SCHOOL OF ELECTRICAL AND COMPUTER ENGINEERING

PERFORMANCE ENHANCEMENT OF AC MACHINES AND PERMANENT MAGNET GENERATORS FOR SUSTAINABLE ENERGY APPLICATIONS

JIANYI CHEN

This thesis is presented as part of the requirements for
the award of the degree of Doctor of Philosophy
of the
Curtin University of Technology

December 1999

SYNOPSIS

Sustainable energy solutions are aimed to reduce the consumption of fossil fuels by using renewable energy sources and energy efficiency techniques. This thesis presents two new sustainable energy applications in the field of electrical machines.

Polyphase induction motors dominate the energy usage spectrum for industrial and commercial applications. The conventional winding structure used in both synchronous and induction machines has a basic unit of the winding with a 60 degree phase belt and a three phase connection either in star or delta. A new winding structure using an innovative Star-Delta Series Connection (SDSC) which has a high winding coefficient and low harmonic content is presented in this thesis. The principle of the SDSC winding is described. The Electro-Magnetic Belt and Electro-Magnetic Space diagram are two important means to be used for optimization of the new winding. Experimental results from two prototypes confirm the theoretical analysis. The efficiency of the new machine at rated load increased by about 3.8% as compared to the standard machine with a conventional winding structure.

Wind energy is one of the most attractive renewable energy options. Wind turbines are designed to couple either synchronous or asynchronous generators with various forms of direct or indirect connection with grid or diesel generators. Permanent magnet (PM) generators using high energy Neodymium- Iron-Boron magnets offer advantages such as direct coupling without gear box, absence of excitation winding and slip rings, light weight and smaller size. This thesis presents the design and development of an outer-rotor PM generator suitable for wind energy conversion. The initial electromagnetic design followed by a Finite Element Analysis is presented in detail. A 20 kW prototype machine was built and extensively tested. It was found that the machine could maintain an efficiency of about 85% for a wide operating range. Equivalent circuit models were developed. The results of the Finite Element analysis matches closely with the experimental and the designed values.

ACKNOWLEDGEMENTS

CONTENTS

LIST OF SYMBOLS

ν	:	Order of harmonic
τ	:	Pole-pitch of the winding
β	:	Blade tip speed ratio
Ω	:	Integral area embraced by the entire integral path
α	:	Position in circular coordinate (radian)
ω	:	Angular velocity
δ	:	Air gap length / load angle
ν	:	Magnetic reluctivity
ψ	:	Flux linkage
α_I	:	Width of a coil-group in radian
ψ_{Iad}	:	Fundamental flux-linkage
Φ_{Iad}	:	Fundamental component of flux in d-axis
Φ_l	:	Leakage flux
Φ_m	:	Magnet flux
β_m	:	Width of magnet
μ_o	:	Parent permeability
μ_o	:	Parent permeability
Φ_r	:	Remanent flux of the permanent magnet
μ_{rec}	:	Recoil permeability
α_Y	:	Periphery angle of a coil pitch
A	:	Magnetic vector potential
A_m	:	Magnet pole area
A_z	:	Magnetic vector potential in Z-axis
B	:	Flux desity
B_{Iad}	:	Fundamental component of flux density in d-axis

B_g	:	Flux density of air gap
B_r	:	Remnant flux-density
C_p	:	Power coefficient
CSG	:	Coil-side group
E.M.F.	:	Electromotive force
EMB	:	Electromagnetic belt
EMS	:	Electro-Magnetic Space
f	:	Frequency / force density
F	:	Electromagnetic force
F_{ad}	:	MMF of armature reaction in d-axis
F_c	:	Coercive MMF of the permanent magnet
f_{lkg}	:	Leakage coefficient
H	:	Magnetic field intensity
H_c	:	Coercive magnetizing force
I_Δ	:	Phase current in delta component winding
i_Δ	:	Current in the delta component winding
$I_{\Delta 1}$	:	Fundamental current in delta component winding
$I_{\Delta 3}$	:	3rd harmonic current in delta component winding
ID	:	Inner diameter
I_d	:	Current in d-axis
I_N	:	Normal current
I_q	:	Current in q-axis----
I_{st}	:	Starting current
I_Y	:	Phase current in star component winding
i_Y	:	Current in the star component winding
J	:	The current density
J_z	:	Applied current density
J_{zpm}	:	Equivalent current density at magnet boundary
K_{dv}	:	Spread factor of vth-harmonic
$K_{dv-\Delta}$	:	Spread factor of vth-harmonic in delta component winding

$K_{dv\text{-}Y}$	:	Spread factor of vth-harmonic in star component winding
$K_{e/m}$	:	Ratio of amplitude of M.M.F. harmonic between new and conventional winding
K_{pv}	:	Chord factor of vth harmonic
K_w	:	Winding coefficient
L_d	:	Direct-axis inductance
L_m	:	Magnet length in the direction of magnetization
L_q	:	Quadrature-axis inductance
L_{stk}	:	Stack length
M.M.F.	:	Magnetomotive force
M_{max}	:	Maximum torque
M_{min}	:	Minimum torque
M_N	:	Normal torque
M_{st}	:	Starting torque
N	:	Number of turns
N_{ph}	:	The total number of turns in series per phase
OD	:	Outer diameter
p	:	Number of poles
P_{Σ}	:	Permeance for the main flux
P_{ex}	:	Total permeance of no-load magnetic circuit
P_l	:	Leakage permeance
P_{mo}	:	Internal permeance of permanent magnet
p_{rl}	:	Per-unit rotor leakage permeance
P_t	:	Power from the wind turbine
P_w	:	Power from the wind
q	:	Electrical degree per slot
q_{Δ}	:	Number of coil-side per group in delta component winding
q_Y	:	Number of coil-side per group in star component winding
R_g	:	Airgap reluctance
SDPC	:	Star-delta in parallel connection
SDSC	:	Star-delta in series connection

S_i	:	Shape function
T	:	Electromagnetic torque
UCSG	:	Unit Coil-Group Side
V_{ph}	:	Phase voltage
W	:	Number of series turns per parallel branch per phase
W_Δ	:	Number of series turns per parallel branch per phase in delta component winding
W^e	:	Weighting function of element
W_Y	:	Number of series turns per parallel branch per phase in star component winding
W_z	:	Number of turns per slot
X_σ	:	Leakage reactance
X_d	:	Direct axis reactance
X_q	:	Quadrature axis reactance
Z	:	Number of slots

CHAPTER ONE

INTRODUCTION

Before the energy crisis was realized, electrical machine technology focus on providing durable products with extended service life as economically as practical. Then, the Arab oil embargo in 1970s and the ensuing awaking to a worldwide energy shortage resulted in a new era for the electrical machinery industry. The impact of these events on electrical machines is considerable. How to conserve the world energy resources through optimum design and renewable energy application of electrical machines is the subject of this thesis.

1.1   Efficiency Improvement in Electric Motors

A recent study [1.1] by US Department of Energy showed that the number of electric motors in the 1 ~ 120-hp range was more than 125 million and 53-58% of the electric energy generated is consumed by electric motor-driven systems. This study presents us a great potential for energy saving by wisely designed energy-efficient electric motors and the devices they drive. An electric motor is a device for converting electrical energy to mechanical energy. The only power consumed by an electric motor is the electrical and mechanical energy losses within the motor, and the balance of the electrical energy is transferred as mechanical energy to driven devices such as machine tools, pumps, fans or conveyors. It is estimated that the motor losses are 5-25% of the input power, depending on the power rating of the motor.

Since energy shortage problem emerged in 1970's and the increasing cost of electric power, motor manufacturers have been facing the challenge to improve electric motor efficiencies to levels that would represent significant savings in energy. Statistics shows that the majority of the motors used in industry around the world are three-phase AC electric motors and most of them are AC polyphase induction motors. Synchronous machines account for less than 1% of the motor-drive energy used in the USA [1.2], and the AC polyphase induction motors dominate the energy usage spectrum insofar as electric motors are concerned. The energy usage of these category ratings of 5 hp and above, is 93% of the total electric motor usage. Induction motor rated and lower, including the fractional horsepower category, account for approximately 5% of the total motor energy utilization. It is seen that even a small percent increase of efficiency, say 1%, from every three-phase electric motor will result in a considerable energy saving in power supply. To achieve the goal of energy efficiency a new dimension has been added to motor technology and design of energy-efficient motor has become a trend in electrical machine industry.

Optimum design of electrical machine took the advantage of the availability of computer-aided design, high-quality materials, and improved manufacturing technology. It can be found that today's motor provides longer service life in much more severe environments than any of its predecessor designs. These actions have been anti-inflationary and have contributed in a major way to world industrialization. The relatively inexpensive energy conversion from electrical to mechanical form provided by electric motors has made possible many of the advances in industrial technology that we enjoy today. For many years, the trend was toward smaller and lighter motors in order to lower cost. Coincident with the trend toward smaller

motors, many users and original equipment manufacturers have been choosing to purchase the low-first-cost motor without considering the power factor and efficiency. Similarly, many books and handbooks on electric motors discuss in great detail the design and performance characteristics of electric motors and the characteristics of various types of motor loads and how to match the motor to the load requirements. However, efficiency, the power factor, energy costs, and life-cycle costing have not been considered as major factors in the design and selection of an electric motor in most applications.

What is the efficiency of an electric motor? Generally speaking, it is the measure of the ability of an electric motor to convert electrical energy to mechanical energy; i.e., kilowatts of electric power are supplied to the motor at its electrical terminals, and the horsepower of mechanical energy is taken out of the motor at the rotating shaft. Therefore, the only power absorbed by the electric motor is the losses incurred in making the conversion from electrical to mechanical energy.

Now, it is quite clear that the task to achieve high efficient-operation of an electric motor is how to reduce the power losses "consumed" by the motor at possible maximum level. The main losses of an induction motor includes five components below:

- Primary I^2r

- Iron

- Secondary I^2r

- Friction and windage

- Stray load

The primary I^2r is the ohmic loss caused by current passing through the stator winding. Most motors use copper conductors, except for some small-horsepower machines with aluminum wire in stator. Where the copper windings are used, there is little more that can be done, from a practical standpoint, to increase the winding conductivity. Obviously, enlarging the cross-sectional area of copper to reduce the primary resistance is an effective means of reducing primary I^2r loss and this method is used in nearly all energy-efficient motor designs. However, increasing copper cross-sectional area results in higher cost of the motor.

Iron loss is caused by the combined effect of hysteresis and eddy current losses and occurs in the stator laminated steel core. These losses are a result of the magnetic field oscillating at fundamental and higher harmonic frequency. Iron losses vary as some power of the magnetic flux density in the iron core. So, reducing flux density can reduce iron losses and this can be achieved by decreasing length of the stator core. Thus, more silicon-steel sheet and copper will be used in such a motor than a standard motor of the same rating. As known, the silicon content and processing of the steel during manufacturing affects the quality of magnetic steel relative to its loss production for a given flux density. Using a better grade of steel for the lamination is also an effective means to reduce iron losses and the thickness of the lamination. Increasing silicon content, up to some practical limit, reduces the watts per kilogram loss, as does annealing the steel. Reducing the thickness of the lamination effects a reduction in the eddy current component of loss.

Similar to the primary I^2r losses, the secondary I^2r losses are the ohmic losses in the rotor conductors. But the same scenario used on the stator does not turn out to be applicable to the rotor, since the secondary I^2r losses are not so easy to be controlled by simply adding more conductor material to the cage structure. The motor starting torque is proportional to its secondary resistance. As the secondary resistance can be varied within a limited range the motor must meet some minimum specified value of starting torque. Additionally, fundamental frequency iron losses are not present in the rotor laminations because the rotor magnetic field oscillates at slip frequency, only a few hertz. Iron losses at low frequency are normally considered to be negligible. But some high-frequency flux pulsations appear in the rotor, particularly near the surface at the air gap. The losses caused by these harmonic fluxes are usually classified as stray load loss.

The friction and windage losses are caused by the friction in the bearings of the motor and the windage loss of the ventilation fan and other rotating elements of the motor. In this thesis, the author is going to discuss the reduction of these mechanical losses.

The difference between total motor losses and the sum of the other four losses is defined as the stray-load loss. They are residual losses in the motor that are difficult to determine by direct measurement and or calculation. These losses are load-related and are generally assumed to vary as the square of the output torque. The nature of this loss is very complex. It is a function of several different factors associated with the design and manufacturing process. The stator winding design has a significant influence to the stray-load loss.

The air-gap flux density is usually considered to be sinusoidal. In fact, it contains other harmonic contents related to saturation effects and slotting of the stator and rotor. These harmonic MMFs result in high-frequency currents in the rotor bar and high-frequency loss in the rotor and stator teeth near the air gap. Although the rotor harmonic current provides a little useful torque, it causes an ohmic loss in the rotor bar. Iron parts such as baffles located close to the magnetic field of coil end turns can be responsible for additional iron losses, which are also classified as stray-load loss. To control the stray-load losses one must take account of both design and careful manufacturing practice.

Owning to the rapidly developed power semiconductor technology, the utilization of power electronic components in variable frequency inverters and soft-starters has provided an economic means for the control of electric motors [1.3-1.5]. However, these external electronic components are bound to increase the first-cost of operation systems and not economic for motors ranging from small to medium sizes. As manufacturers and users still concern about the cost of motors while they are seeking energy-efficient motor, it is quite attractive to increase efficiency by improving motor itself with some novel design.

In chapter two, a novel principle is presented to direct the design of 3-phase winding of AC electrical machine. The winding of an electrical machine designed in accordance with this principle can have higher winding coefficient and lower harmonic content. This principle is applicable to both induction and synchronous machines where the neutral is not necessary. Due to the higher fundamental spread

factor of the new winding motor, the load current can be lower than the conventional winding motor. Correspondingly, the primary I^2r loss, iron loss, the secondary I^2r losses and stray-load loss are reduced.

Mathematical analysis in chapter three verifies that the new winding designed is able to reduce a great amount of the amplitude of harmonic contents in induction motors, especially those troublesome components such as fifth and seventh, etc. The efficiency of the new winding motor is expected to increase by more than 3%. The experimental investigation has been included to confirm the predicted results. Also, the torque of the new winding motor is higher than its conventional counterpart.

1.2 Generators for Wind Turbine Applications

The worldwide energy shortage has prompted the research and development of the renewable energy, including wind energy, wave energy, direct solar radiation, tidal energy and geothermal energy. Many countries have consequently allocated substantial funds to the study of alternative energy resources over the last two decades. Wind energy has emerged as one of the most promising renewable energy technologies since then, although it was not initially regarded as having any particular promise.

Since the power output from wind turbines varies considerably from one day to the next due to changing wind speeds, careful consideration must be given to how it is used. Modern wind turbines have found their major applications producing electricity, and operating either in parallel with conventional power stations, or in

smaller more isolated communities, diesel engines. The coal and oil burnt in the power plants and diesel engines provides continuously reliable power to meet the demand while the wind turbines contribute energy to the system, as the wind blows, so that the overall fuel consumption can be significantly reduced.

A site with average wind speed of 15 MPH is considered an ideal place for setting up wind generator [1.6]. But this does not mean that a site with less than a 15-MPH average is not a potential site. When a designer estimates the potential output from wind energy conversion, even working at average speeds of 9-10 MPH, wind generators can be more cost effective than solar modules over similar production periods, especially since wind generators can produce over a broader range of time – as in the day and night.

1.2.1 Wind Turbine Generators Connected to Grid

Wind turbines may be designed to couple either synchronous or asynchronous generators, and with various forms of direct or indirect grid connection of the generators. Direct grid connection means that the generator is connected directly to the (usually 3-phase) alternating current grid. Indirect grid connection means that the current from the turbine passes through a series of electric devices that adjust the current to match that of the grid. An asynchronous generator can implement it automatically. Wind turbine generator converts mechanical energy to electrical energy. Compared to other generating units ordinarily attached to the electrical grid, wind turbine generators are a bit different. The main reason is that the generator has to work with a power source (wind turbine rotor) that supplies very fluctuating mechanical power (torque). In order to operate at the standard utility frequency (50

or 60 Hz) gearboxes are used between wind turbines and generators to step up the generator shaft speed in most wind conversion systems.

Being coupled to wind turbines, synchronous generators normally use electromagnets in the rotor, which are fed by direct current from the electrical grid. Since the grid supplies alternating current, they have to convert alternating current into direct current before connecting the power to the excitation windings around electromagnets on the rotor. This connection is implemented by using brushes and slip rings on the shaft of the generator.

The synchronous generator has been the primary means getting AC power since the replacement of DC power generation. So, it has the most natural attraction because of its long-term association with the power industry. In an AC system, it is required to provide reactive power to loads and transmission network for voltage support and regulation. A synchronous generator can produce the necessary reactive power for both. Stability is one weakness existing in synchronous operation, particularly under fault conditions. However, wind turbine driven generators raise new stability questions. Rapid variation in mechanical input torque to a synchronous generator causes the electrical output to follow closely causing a potential loss of synchronism with the system. The investigation of these stability questions is the focus of other studies. Some possible special stability may be required in the control system, such as a power stabilizer. The addition of such equipment would increase the cost of synchronous operation.

Most of generators for wind turbine applications are three phase asynchronous generators, or induction generators. This type of generator is not widely used outside the wind turbine industry and in small hydropower units. But three-phase induction machine is the most popular electrical machine, which can be run either as a generator or a motor. Today, one third of the world's electrical energy is consumed by induction motors to drive a variety of machinery in factories, such as pumps, fans, compressors, elevators, machine tools and other applications where electrical energy is needed to be converted to mechanical energy. The advantage of the induction generator is that it is very reliable, and tends to be comparatively inexpensive. It also has some useful mechanical properties for wind turbine applications, like generator slip and certain overload capacity. So, most of the grid connected wind turbine generators (rated typically between 200 – 750 kW) use induction machines.

It should be aware that the induction generator has two disadvantages in operation. First, a reactive source is required for both the generator and the remainder of the system since an induction generator consumes reactive power. Furthermore, voltage stability problems are known to exist for induction generator operation. Both of these problems must be addressed to answer satisfactorily the usefulness of induction generators for wind power generation.

The new AC winding principle proposed by the author can result in performance improvements of induction machines in both motor and generator modes. The proposed method is particularly attractive for induction generators used in wind power applications.

1.2.2 Wind Generators for Stand-Alone Power System

Currently most of the wind turbine generators are connected to large utility grids. It is not cost effective to extend the grid to remote and isolated locations. For example, Australia is a large country with an area of 7.5 million Km^2 and has a small population of about 18 million. State power grid systems supply electricity to approximately 95% of the population living in the state capitals and industrial centres [1.7]. The electric utility companies find it highly uneconomical to extend the grid into sparsely populated regions of the country [1.8]. Thus, many small remote communities have to depend on stand-alone electrical supply systems. These locations represent a significant potential market for stand-alone energy systems usually categorized as Remote Area Power Supplies (RAPS). Traditionally, electricity energy for remote areas has been supplied by diesel driven alternators, characterized by high reliability, high running cost, low efficiency and high maintenance.

It is widely recognized that wind energy is likely to be economically viable in many parts in the world where electricity is generated using diesel fuel. In RAPS systems, the cost of producing electric energy is very high; hence these may be the economic advantages of using renewable energy. In isolated windy location, wind powered generators with battery storage are becoming cost-effective. Nevertheless, for such schemes to be viable and worthwhile, the saved diesel fuel must be significant, and this can be achieved by employing wind turbine generator with rating comparable to or larger than the total demand of the system.

Recent investigations show that there is increasing demand for higher rating wind generators for battery charging in small isolated wind/diesel hybrid power systems. These stand-along systems usually supply power to household appliances, water pumping, water desalination, remote communication equipment, catholic protection for buried pipelines, etc.

The wind turbine generators used in the systems have been small in size, usually less than 5 kW. The three most common electric generators used for isolated wind power generation are DC generators, generators with field wound or permanent magnet and capacitor-excited induction generators. The DC generator and the field wound generator have maintenance problems associated with commutators and brush gear. Permanent magnet generator and induction generator are receiving increasing attention because of the qualities like ruggedness, low cost, manufacturing simplicity and low maintenance requirements.

Stimulated by the increasing availability of high-energy permanent magnet materials, there has recently been much interest and activity in wind-driven generators with permanent magnet excitation [1.9-1.12]. Alternating current generators with permanent-magnet rotors can offer obvious advantages such as the absence of brushes, slip rings, excitation windings, DC supplies, and field circuits losses. This sort of generators are required to be as compact and light as possible so that the machines can be conveniently transported to remote locations and installed at the top of the towers. Permanent magnet generator can work efficiently, and is simple and robust in construction. These obvious merits and the application of new permanent magnetic materials like Nd-Fe-B, have made this type of machines play an important

role in the electrical generation industry, particularly in the areas of wind energy conversion in stand-alone generation.

In chapter four of the thesis, the author presents the design of a permanent magnet generator using Neodymium-Iron-Boron magnets for directly coupled wind turbine applications. To accomplish the goal of small size and lightweight with an extra-low speed for direct coupling, the outer rotor structure is applied to suit the multi-pole construction. Important design principles associated with the outer rotor structure are discussed along with the critical design constraints. A direct-design method is used for the initial electromagnetic design. In the chapter five, finite element method will be applied to analyze the details of the design.

1.3 Finite Element Analysis for Machine Design

During the last two decades numerical techniques particularly the finite element method, have been proven valuable in the design, performance evaluation, and optimization of electrical machinery. In modern power systems, electrical machines such as generators and motors usually operate in parallel, connected to a source with a known voltage. Short-circuits, system transients and other abnormalities on the power system affect the integrity and efficient performance of all the connected devices. An electrical machine is not completely modeled until its interaction with the rest of the power system is taken into account.

Based on the assumption that the sources are unaffected by the finite element solution and external circuitry, the modeling approach has most commonly involved two-dimensional finite element boundary-value problems with specified current

sources for the conductors. Voltages at the terminals of the machine under evaluation are derived a posteriori by calculating flux linkages and their products with angular velocity. Alternatively, the voltage can be obtained by computing electrical field and integrating over a prescribed path. However, electrical machines in practical application are connected to voltage sources instead of ideal current sources. One should be aware that the connection of the windings and the presence of active or passive external circuits might complicate the problem.

Numerical techniques have long been regarded as practical and accurate methods of field computation in the design of electrical machines. Prior to the finite element method, finite differential and integral equation methods were used in electromagnetic calculation. Although all these methods have been used and continue to be used either directly or in combination with others for design, finite elements have emerged as appropriate techniques for low frequency application. Early real finite element solution of the scalar Helmholz equation appeared in late sixties [1.13]. Two-dimensional nonlinear magnetostatic techniques for electrical machines were first put forth in the early seventies [1.14-1.17]. Since then, a variety of other applications of the steady state and transient eddy current methods soon followed [1.18,1.19], which included rotating machinery and power conditioners.

Field models of devices are usually based on some sort of discretized geometry. The device and the space surrounding it are first divided into small, nearly regular pieces, called elements. Then the elements are used to obtain solutions to the field equations in the modeled volume. Chapter five is concerned with the finite element method relying on a discretization of two-dimensional space.

14

Both finite elements and circuit techniques are often used to model devices. A current or current density is usually adopted as the natural excitation for finite element models. If the current is supplied by an external circuit and is unknown, then some means of coupling the circuit to the finite element model must be developed.

The formulation adopted for combined circuit and field analysis should meet two requirements. First, the formulation should be general. It must be represent all classes of field behavior, including electrostatics, eddy currents and wave propagation. If the formulation is general it follows that circuit behavior must be described as a subset of the same formulation. The second requirement is that the separation between circuit behavior and field behavior be relatively straightforward, and involve only a few assumptions. A simple connection without awkward constructs helps to maintain generality, and make the capability easier to implement and use.

The formulation begins with Maxwell's equations in their general form and derives an equivalent variational principle. An equivalent matrix equation is then derived for discrete finite element solution variables. Variables that satisfy the matrix equation, also minimize the energy of the system and, therefore satisfy Maxwell's equations. As both the integral and differential forms of the equations are related to the energy or energy density, they are given the term functional.

In the finite element method, the analytic functional of vector potential $A(r,t)$ and scalar potential $\psi(r,t)$ are expressed as the product of shape functions. The functions vary only with position and discrete values at predetermined grid point locations. The

space integrals are evaluated once, ahead of time, leaving on the time-dependence of the degree-of-freedom to be determined in the actual finite element method calculation. The solution volume is subdivided up into small, semi-regular regions called finite elements. Within each element, the spatial integrals are performed numerically, and assembled together into large matrices representing the entire model. The resulting matrices embody the geometric and material properties of the model, but do not depend on time. Two-dimensional elements are obtained by assuming that all components of the potentials only vary within the plane of the element, and not through its thickness. These elements are useful for modeling thin, conducting sheets and thin air gaps.

In chapter five, the two-dimensional finite element method is used for the analysis, performance evaluation and optimization of electromagnetic calculation of the permanent magnet generator. The variational formulation has its attractiveness that the functional relates to the physical concept energy. However, the weakness of the approach is that for every equation to be solved, a functional needs to be identified at its minimum to satisfy the differential equation being solved. The Galerkin approach can overcome this difficulty of identifying a convenient functional [1.20]. Newton-Raphson method has been adopted to deal with the non-linear problems of electromagnetic field where magnetic permeability is a function of the local magnetic field [1.21]. Although the designed generator has a different construction from normal synchronous machines, it is reasonable to use a standard method of mesh generation to produce triangular elements within the domain. The increments δA_i of vector potential A_i can be obtained by solving the matrix equation. Calculating flux linkages and their products with angular velocity derives the terminal voltages of the

generator to be evaluated at no-load and load conditions. The method is suited for used with two-dimensional magnetic vector potential models for the analysis of magnetic fields under no-load and load conditions of the outer-rotor machine. The Maxwell stress method is one of the most popular methods used to calculate global force and torque in finite element method. The simulation of force and torque shows well-behaved results by employing the Maxwell stress method. The derivation of the Maxwell stress expressions is presented in chapter five. Some of the drawbacks of the B^2 method can be overcome by the Maxwell stress method for computing forces. The simulation of the electromagnetic torque and power capability are given following the computation of the globe forces. The discussion includes some suggested improvements for performance prediction of the outer-rotor permanent magnet generator.

1.4 References

[1.1] U.S. Department of Energy, DOE/EIA-0383, (1991), *Annual Energy Outlook 1990*, Washington, DC.

[1.2] *Classification and Evaluation of Electric Motors and Pumps*, (1980), Washington, DC, U.S. Department of Energy, November 1980.

[1.3] DeBuck, F.G.G., Gistelinck, P. and DeBacker, D., (1984), "A simple but reliable loss model for invert-supplied induction motors", IEEE Transactions on Industry Applications, Vol. IA-20, Jan./Feb., pp. 190-202.

[1.4] Green, R.M. and Boys, J.T., (1982), "Implementation of pulsewidth modulated inverter modulation strategies", IEEE Transactions on Industry Applications, Vol. IA-18, March/April, pp. 138-151.

[1.5] Erickson, C.J., (1987), "Motor design features for adjustable frequency drives", IEEE Transactions on Industry Applications, Vol. 24, March/April.

[1.6] Golding, E.W., (1976), '*The generation of electricity by wind power*', John Wiley & Sons, Inc., New York.

[1.7] Nayar, C.V., Phillips, S.J., James, W.L., Pryor, T.L. and Remmer, D., (1993), "Novel wind /diesel/battery hybrid energy sysytem", Solar Energy, Vol. 51, No. 1, pp. 65-68.

[1.8] Kaneff, S., (1990), "Grid extension to stand-alone systems", The option, Electrical Engineer, April, pp. 66-69.

[1.9] Chalmers, B.J. Wu, W. and Spooner, E., (1998), "An axial-flux permanent-magnet generator for a gearless wind energy system", IEEE Transactions on Energy Conversion, Vol. 14, No. 2, June, pp. 251-257.

[1.10] Chen, Z., Spooner, E. Norris, W.T. and William, A.C., (1998), "Capacitor-assisted excitation of permanent-magnet generator", IEE Proc.-Eletr. Power Appl. Vol. 145, No. 5, Nov., pp. 497-508.

[1.11] Spooner, E., Williamson, A.C. and Catto, G., (1996), "Modular design of permanent-magnet generators for wind turbines", IEE Proc.-Eletr. Power Appl. Vol. 143, No. 5, September, pp. 388-395.

[1.12] Soderlund, L., Eriksson, J-T., Salonen, J., Vihriala, H. and Perala, R., (1996), "A permanent magnet generator for wind power application", IEEE Transactions for Magnetics, 1996, Vol. 32, No.4, pp.2389-2392.

[1.13] Silvester, P., (1969), "Finite element solution of homogeneous wave-guide problems", 1968 URSI Symp. Electromagnetic Waves, Alta Frequenza, Vol. 38, pp.313-317.

[1.14]   Silvester, P. and Chari, M.V.K., (1970), "Finite element solution of turable magnetic field problems", IEEE Transactions, PAS-89, No.7, pp.1642-1651.

[1.15]   Silvester, P., Cabayan, H.S. and Browne, B.T., (1973), "Finite element solution of saturable magnetic field problems", IEEE Transactions, PAS-92, No.4, pp.1642-1651.

[1.16]   Andersen, O.W., (1973), "transformer leakage flux program based on the finite element method", IEEE Transactions, PAS-92, No.2.

[1.17]   Chari, M.V.K. and Silvester, P., (1971), "Analysis of turbo-alternator magnetic field by finite element method", IEEE Transactions, PAS-90, pp.454-464.

[1.18]   Chari, M.V.K., (1973), "Finite element solution of the eddy current problem in magnetic structures", IEEE Transactions, PAS-92, Vol. 1.

[1.19]   Hannalla, A.Y. and Macdonald, D.C, (1976), "Numerical analysis of transient field problems in electrical machines", Proc. IEE, Vol. 123, pp. 893-898.

[1.20]   Hoole, S.R.H., (1989), *Computer-aided analysis and design of electromagnetic devices*', Elsevier.

[1.21]   Silvester, P.R. and Ferrari, R.L., (1990), *Finite element for electrical engineers*', 2nd Ed., Cambridge University Press, Cambridge.

CHAPTER TWO

DESIGN PRINCIPLE OF A NEW THREE-PHASE WINDING

Abstract

It has been established that a greater output can be achieved from a induction machine with a given frame size by increasing the number of phase in the winding and therefore reducing the phase spread as well as increasing the fundamental spread factor. One of the improvements that have been suggested is to employ a star-delta series connection (SDSC) winding.

A new 3-phase winding designing principle is described in this chapter. There are two components, star and delta, in one of three phase windings and the two components of the three-phase winding are connected in series to a 3-phase supply. Theoretically, the new principle is applicable to both induction and synchronous machines where the neutral is not necessary. With this configuration, the circulating currents between two winding components, which are easily to appear in parallel connection, can be completely prevented.

Flexible selection of the Electro-Magnetic Belt (EMB) is another feature of the new winding. Generally, optimization of the EMB leads to a higher fundamental spread factor than for a conventional three-phase winding. The Electro-Magnetic Space (EMS) diagram is a very useful tool in designing a new winding. The arrangement of the 3-phase winding and connection of coils can be directly derived from this diagram.

Being manufactured in single-layer, the chord factor of the new winding is always unity. The technically shorter coil-span results in lower DC resistance of the SDSC winding. The design procedure of this winding is demonstrated with two detailed examples. The winding of an electrical machine designed in accordance with this principle can have higher winding coefficient and lower harmonic content.

2.1   Introduction

The conventional winding structure of 3-phase AC electric machines has been used in industrial manufacture for over half-century. This type of winding structure has following features:

(1) The basic unit of the winding has a coil or coil-group span forming 60° phase-belt, namely 60° electrical angle distribution per pole per phase.

(2) The connection between the individual phase windings in a three-phase winding is in either single-star or single-delta form. This winding structure has dominated the manufacture of electric machines for a long period. It is true that this kind of winding structure has many merits: Since it came out in electrical machine industry a considerable progress has been made on performance improvement of electrical machines.

However, it is the above two features that the conventional 60° phase-belt winding is limited to give better play to the potential capacity. Further improvement of the power output and efficiency is difficult, the M.M.F. harmonic content and electromagnetic noise are still higher than desired and the starting performance is not smooth enough.

It is known, from previous research [2.1][2.2], that a greater output can be achieved from an induction machine with a given frame size by increasing the number of

phases in the winding and therefore reducing the phase spread as well as increasing fundamental spread factor. Much of the effort in past years was in refining designs in response to requirements for particular applications, e.g. pole changing by pole amplitude modulation (PAM) [2.1][2.8][2.9] by using a monotonous delta-star winding configuration. The essence of the delta-star mixture winding lies in the subdivision of a conventional 3-phase 60-spread winding into a delta component and a star component. The two components must occupy 30° electrical angle for each and can then be connected in either parallel or series across the same supply. In those practices, either the delta and star components must contain half of the total number of slots with coils made up of two different numbers of turns, or delta component must occupy as $\sqrt{3}$ times of slots as star component does with identical coils. Nevertheless, due to this design criterion, the delta-star mixture winding is seriously impeded for wider application in industry.

Based on the summary of the previous research works [2.1-2.7], a new principle is presented to direct the design of AC electric machine winding. The new winding designed using this principle is not bound to the basic unit of 60°-phase belt and can have diversified forms. Instead of single-star or single-delta form, the connection of novel 3-phase winding has more flexible and free choice. The distribution of star and delta components of the new winding is not necessary to be restricted by 30 electrical degree for each. In manufacture, the new winding can definitely be arranged in single-layer. Additionally, a shorter coil span than full-pitch may be used in practice to reduce the mean length of the coils. With these features, the new winding can overcome the shortcomings existed in the conventional winding and further improve the whole performances of AC machines. Two detailed design examples following

the principle are given in this chapter. This new 3-phase winding technique can be applied to both three-phase induction machines and synchronous machines that do not need neutral terminal to be brought out. It means that the new type of winding can be used by wind generators for charging battery and synchronous motors. For example, it can be definitely adopted for the armature of a permanent magnet generator for wind energy conversion such as the one to be described in chapter IV.

2.2 Technical Terms [2.5]

There are two technical terms used in the design and analysis of the new winding. Since the terms are seldom used in conventional winding structure, they are defined in this section.

2.2.1 Electro-Magnetic Belt (EMB)

In conventional electrical machines, the winding under each pole is divided into three parts, each part consisting of a coil-group and occupying 60 electrical degrees. This winding width per pole per phase is the basic unit of the winding and is called 'phase belt' for corresponding with one of the three phases of power supply. Because the new winding is made in single-layer, the term of coil-group is not used and is replaced by the Coil-Side-Group (CSG). The basic unit of new winding, as stated previously, is diversified and no longer constrained by the CSG of 60° electrical. Hence, the term of 'phase belt' is not suitable here. As soon as the current fed into the new winding of an electrical machine produces an electromagnetic field and operates via electromagnetic induction, the basic Unit-Coil-Side-Group (UCSG) of the new winding sets up a basic unit of electromagnetic field. Therefore, the

electromagnetic space occupied by an UCSG is defined as an Electro-Magnetic Belt (EMB), expressed in electrical degree, so as to distinguish from the 'phase belt' of the conventional winding.

2.2.2 Electro-Magnetic Space (EMS) Diagram

This term refers to the distribution diagram of coil-sides positioned in electromagnetic space. Consider a stator core with 36 slots which is visualized to be spreaded as a straight belt, as shown in Fig. 2.1. The straight belt is divided into 36 equivalent parts, each containing a slot. The origin is set at the centre of the 36th slot, which occupies the 0° of space position. Then, the 1st slot is at 10°, the 2nd at 20°, and so on. The 36th slot is at 360° and returns to the origin.
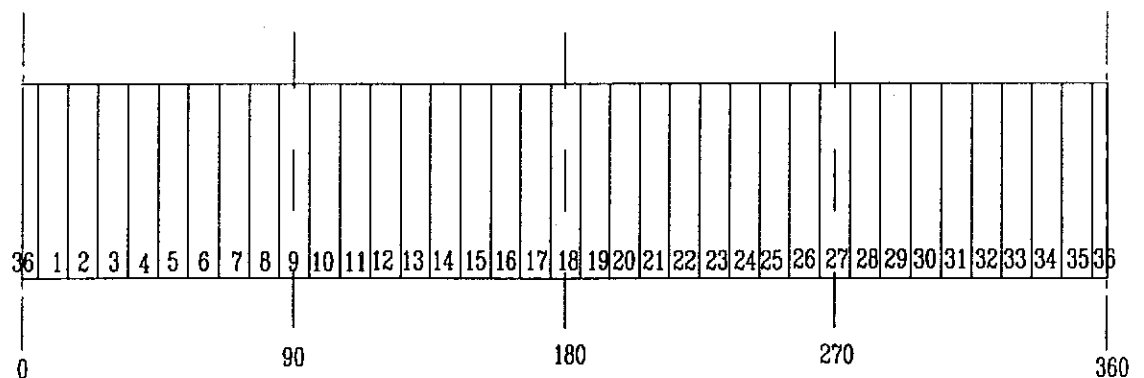
Fig. 2.1 Mechanical space position of spread stator

Once current flows through the machine winding, an electromagnetic field is built up in the space around the electrical machine. The stator and its winding are surrounded by this field. It is obvious that the relation between the slots is no more in mechanical

25

space degrees, but in electrical angle according to the state of the Electro-Magnetic

Space (EMS). Let the number of the poles, p = 4, and the magnetic field distribution

at a given instant is as shown in Fig. 2.2(a) where the origin is at the centre of the

36th slot. But, as the field in Fig. 2.1 changes to that in Fig. 2.2, the 1st slot is at 20°,

the 2nd 40°, and so on. According to the electromagnetic effect, the 1st and the 19th

slot, embracing coil side 1 and 19, are situated at the same EMS position. In view of

the electromagnetic effect, Fig. 2.2(a) can be further developed into Fig. 2.2(b).
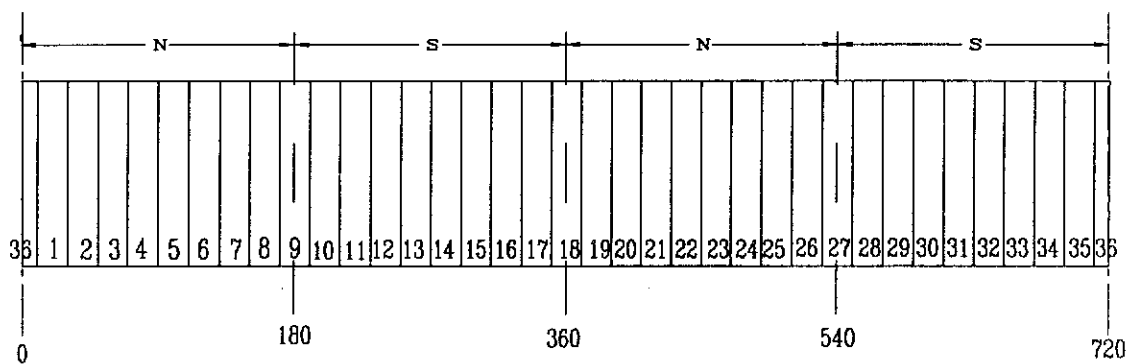
Fig. 2.2 (a)   EMS position of spread stator
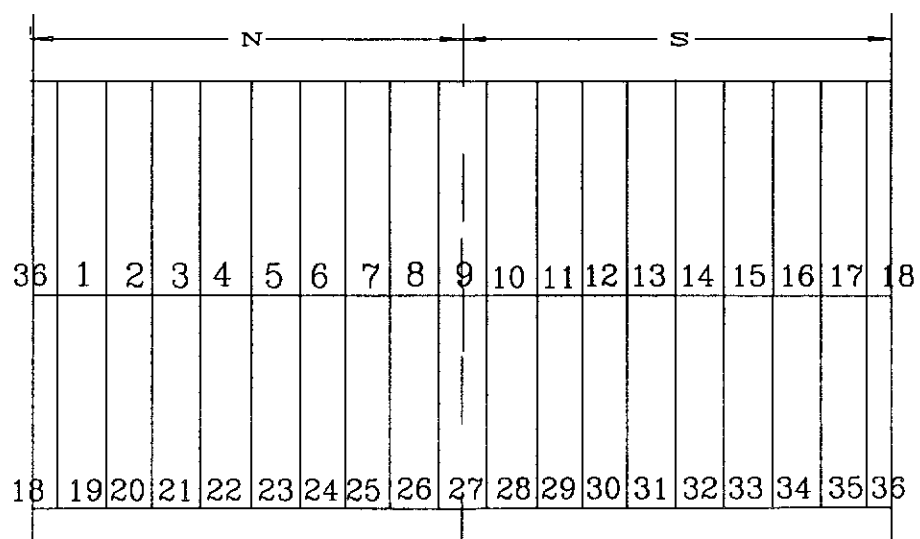
Fig. 2.2(b) Equivalent EMS position of spread stator

Fig. 2.2(a) and (b) show the magnetic position of the stator slots at a given instant. If the spread out stator is restored to its circular shape, an EMS diagram can be obtained as shown in Fig. 2.3. As the space distribution of the rotating magnetic field varies with time, it is not necessary to designate the polarity of 'N' and 'S'. Since the origin can be set at will, it is not necessary to label it in the EMS diagram, nor the corresponding electrical degrees of every coil-side.
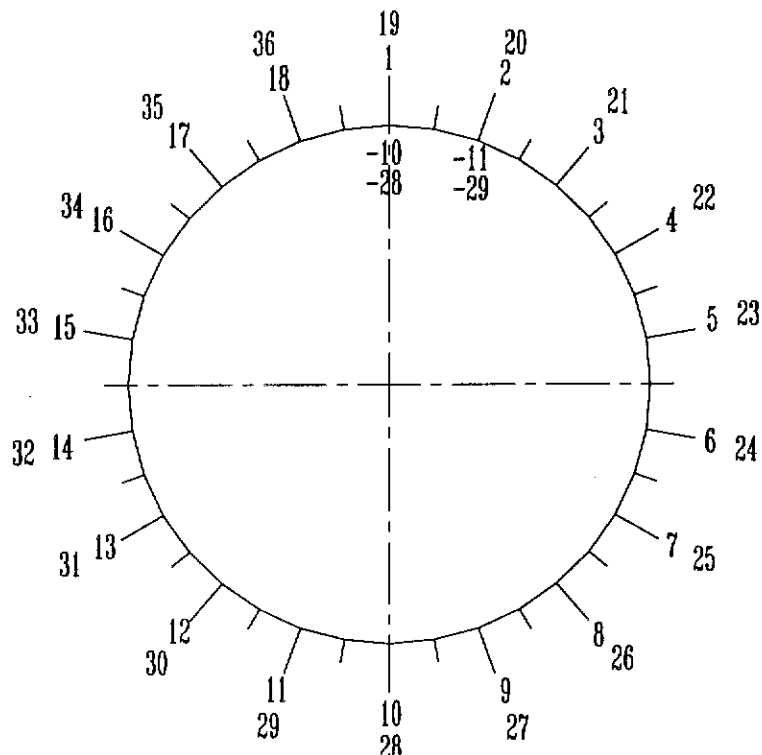
Fig. 2.3 EMS diagram of a winding, with Z=36, p=4

Another characteristic of the EMS diagram is that not only are the corresponding coil-sides of same polarity situated at the same EMS position, but also are the corresponding coil-sides of opposing polarity, when their connections are reversed through 180°. For distinguishing, the reversed coil-sides are denoted by a negative

note "-" sign. For example in Fig. 2.3, the coil-side 10 and 28, after connections have been reversed by 180°, can be shifted to the EMS position of coil-side 1 and 19. This regulation is useful for winding arrangement.

2.3   Principle of the New AC Winding

The new winding breaks through the restrictions of the conventional windings. Its three-phase winding connection is not the single-star or single-delta, and the basic unit of its winding is not bonded by the '60° phase belt' range. In particular, the sum of EMB of star and delta components does not need to equal 60°. This feature is significant to improve the performance of AC electrical machine.

2.3.1 Type of Connections for The New 3-Phase Winding

In stead of the conventional 60°-belt single-star or single-delta winding, a star-delta mixture connection is adopted in the new winding. Two types of winding in mixture connection are proposed:

- • Star-delta in parallel connection (SDPC);
- • Star-delta in series connection (SDSC).

The SDPC configuration shown in Fig. 2.4 is not easy to implement in practice because of the following drawbacks:

i)   The converted effective number of turns in series of the star and delta component windings must be exactly equal.

ii)   The converted cross section of the conductors in the star and delta component

windings should be exactly equal.   29

To ensure that the parameters of the two components, such as resistance and inductance are equal, the space geometry occupied by the two component windings should be strictly equal, including tooth width, slot width, slot depth, slot pitch, slot opening, air gap, etc. This is difficult to achieve with the present design and manufacturing technology. If any of the above requirements are not satisfied some or even seriously unwanted circulating current will occur in the three closed circuits 1, 2 and 3 shown in Fig.2.4. Therefore, this type of connection is seldom used in the new winding.
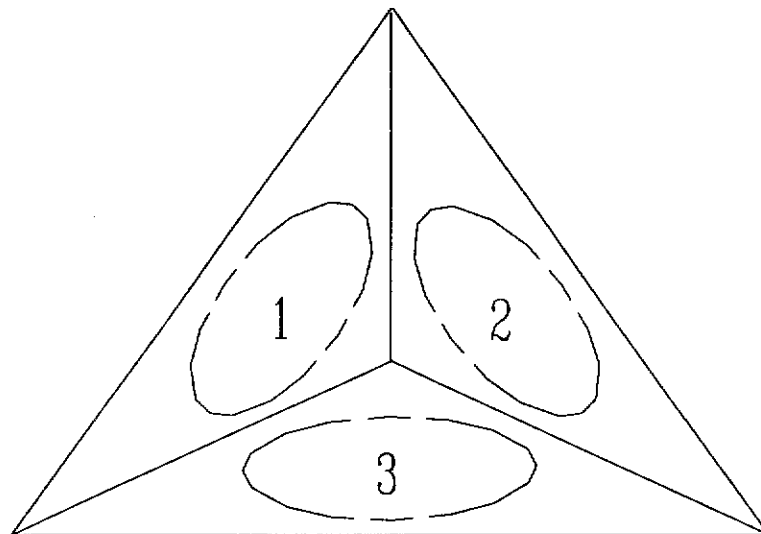
Fig. 2.4   Star-delta mixture connection in parallel

Generally, two types of star-delta mixture series connection are favorable forms: the single-star, single-delta connection shown in Fig. 2.5a and the double-star, single-delta connection shown in Fig. 2.5b. It can be seen that the drawbacks existing in the

SDPC winding disappear in these two configurations. Firstly, there is no circulating current between the two component windings at all. Secondly, it is easier to determine the number of turns in the two components. The ratio of effective number of turns between the star and delta components is not necessary to be equal to $1:\sqrt{3}$. This brings much convenience to the design of winding. An important design rule is that the two component windings must have an EMS displacement of 30° electrical angle with respect to the fundamental. Also, there must be a displacement of 120 electrical degrees between three phase windings for balanced 3-phase operation.

In the connection of Fig. 2.5a, the star and delta component winding should have the cross-section of conductors in the ratio of $\sqrt{3}/1$ and the number of coil turns in the ratio of $1/\sqrt{3}$. With this constitution, the winding consists of the so called 'non-uniform-constitution' due to the different cross section of conductor and different number of turns of coils.

In the connection of Fig. 2.5b, there are two branches in the star component and one in the delta. In this configuration, the coils of the both components can be made up using the same number of turns and the same size of conductor. Thus the term 'uniform-constitution' is used to describe this type of winding configuration.

The new winding has two advantages. Firstly, as every phase winding is subdivided into two components with optimized EMB, a higher spread factor can be obtained. Secondly, as the two component windings have a space displacement of 30° electrical angle, the harmonic content of the magnetic field can be effectively reduced. It is seen that the star-delta mixture connection winding has advantage over

the conventional winding. Also, the star-delta series connection overcomes the shortcomings in star-delta parallel connection. Hence, the star-delta mixture series connection is an important principle of the new winding.
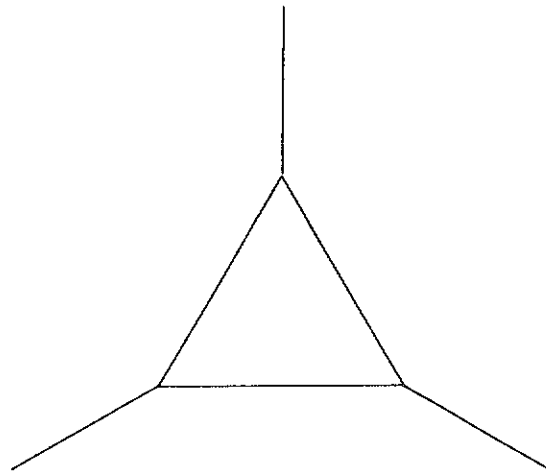
(a)
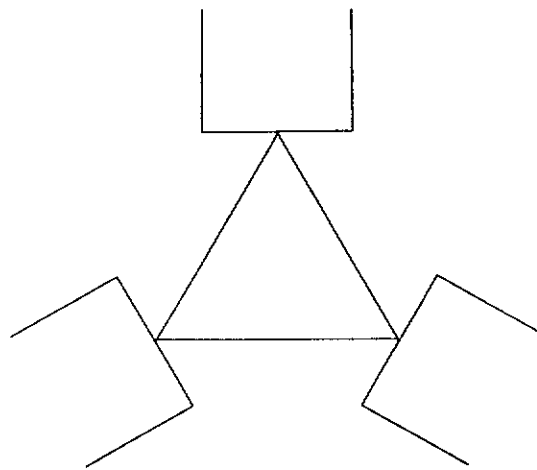
(b)

Fig. 2.5   Star-delta mixture connection in series

2.3.2 Optimization of EMB

Because the winding arrangement is not limited by the 60° phase-belt, the new winding allows a flexible choice of basic unit EMB. Depending upon number of poles and total number of slots, a variety of EMBs can be selected, such as 20°, 24°, 30° and 40° etc. It is the flexible EMB that allows the new winding to have optional combinations of star and delta components, which leads to certain advantages. Hence, the flexible selection of the EMB is another one of the important principles of the new winding.

Three basic rules are presented here to permit the selection of EMB.

(a)   To obtain a high spread factor, narrow EMB is preferred while taking account of a synthetic affection over the whole performance.

(b)   The total peripheral electrical angle must be three times the EMB so that the total number of EMBs can be evenly distributed in between the three phases, namely

$$\frac{p \times 180^{o}}{EMB} = 3k \tag{2.1}$$

Where, k is a positive integer except zero.

(c)   Once all of the EMBs are put together to make up a complete three-phase winding, a displacement of 30° electrical angle must be between the star and delta components per phase.

2.3.3 Coil-Pitch and Winding Type

Usually, double-layer winding is used in the conventional electrical machines. With this arrangement, it is possible to ensure an appropriate short-pitch chord factor to reduce harmonic content of M.M.F.

In the new winding, most of M.M.F. harmonic content can be reduced to a low level, some even get cancelled. Therefore the double-layer winding is no longer necessary, and single-layer winding is used. Theoretically, a full-pitch is employed for the coil-span so as to acquire a higher winding coefficient. If possible, a shorter coil-span can be applied to the new winding to reduce the mean length of the coil, which in theory behaves as full-pitch. Compared with the conventional winding, the new winding has following features;

a)   higher winding coefficient.

b)   lower harmonic content, some are even varnished except the tooth ripple.

c)   single-layer winding can be used.

d)   the new winding may employ shorter coil-span.

Although the uniform-constitution of the new winding consists of two different coils and the end connections are slightly more complex than a conventional winding, it is not expected to cause big increase in labor costs.

2.4 Construction of the New Winding

Two examples are given to illustrate the design procedure:
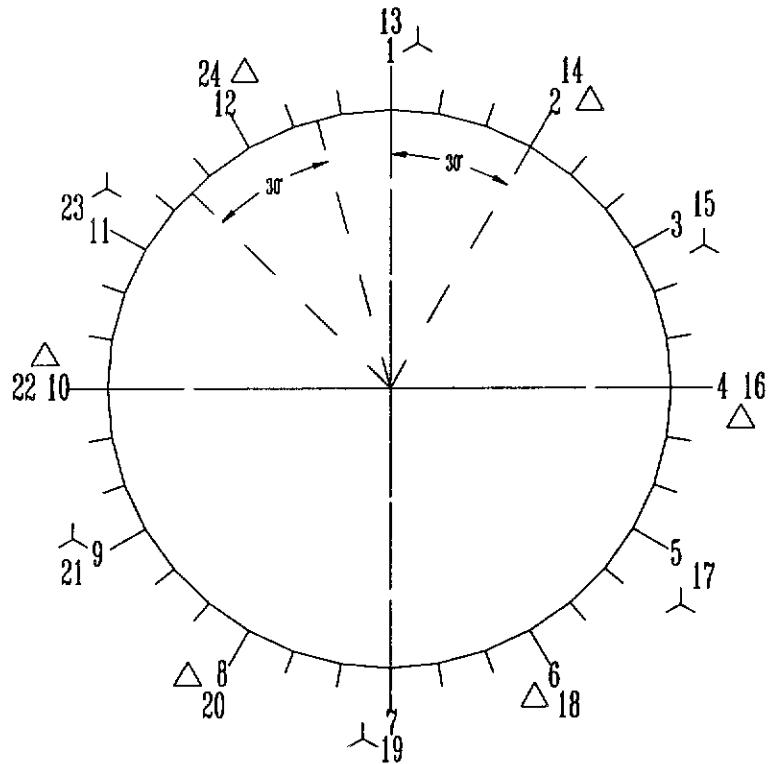
Fig. 2.6   EMS diagram of the winding with p=4 and Z=24

2.4.1 4-Pole Winding in 24 Slots

Example 1: To design a winding with p = 4 and Z = 24;

Step 1: The EMS diagram is shown in Fig. 2.6. As the slot-pitch is 30° electrical angle, the narrowest EMB that may be selected is 30° electrical angle. One coil-side per group is used to form the basic unit of the new winding.

Step 2: Every coil-side is given the attribute of star ($\curlywedge$) or delta ($\triangle$), as shown in Fig. 2.6. The UCSG-$\curlywedge$ (1,13) belongs to the star group, and the UCSG-$\triangle$ (2,14) to the delta group. There is a displacement of 30° between the two UCSG. Similarly, other UCSG belong to star or delta alternately.
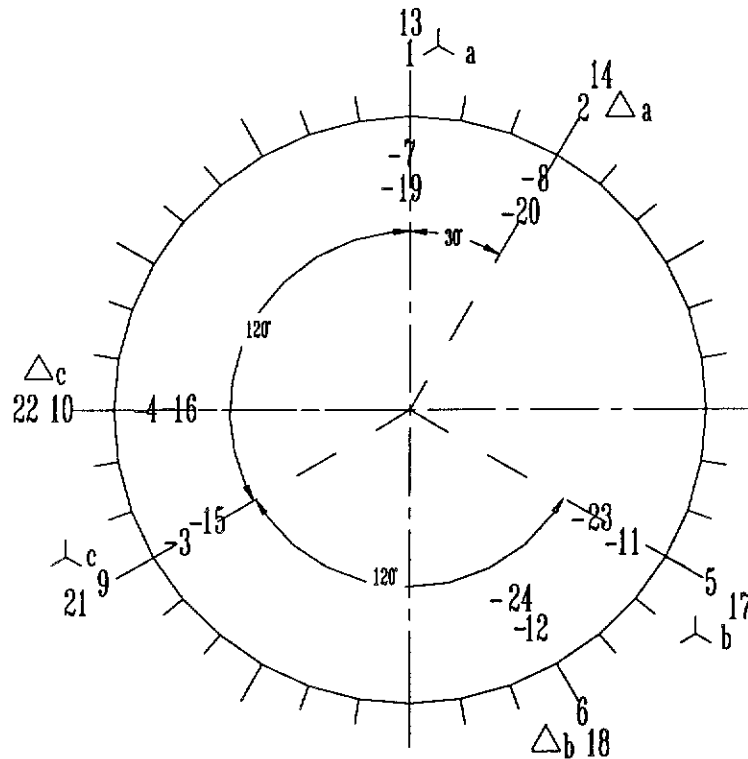
Fig. 2.7   Star-delta component diagram with E.M.B.=30°, p=4 and Z=24

Step 3: All coil-sides belonging to star or delta component winding in the same phase are connected together. Note that all reverse-connected coil-sides are now located at the opposite position, i.e. 180° displacement from their original. For example, coil-sides 7 and 19, after reverse-connection, have the same space position as 1 and 13, expressed as -7 and -19. It is seen, in Fig. 2.7, that there is an exact displacement of 30° between the star and delta components of the same phase and

35

three star or three delta component windings have a displacement of 120° between each other. Thus, a completely symmetrical three-phase winding has been formed.
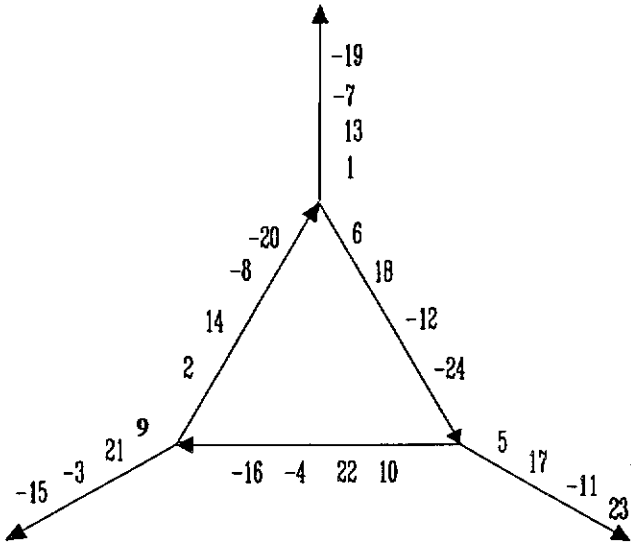
(a)
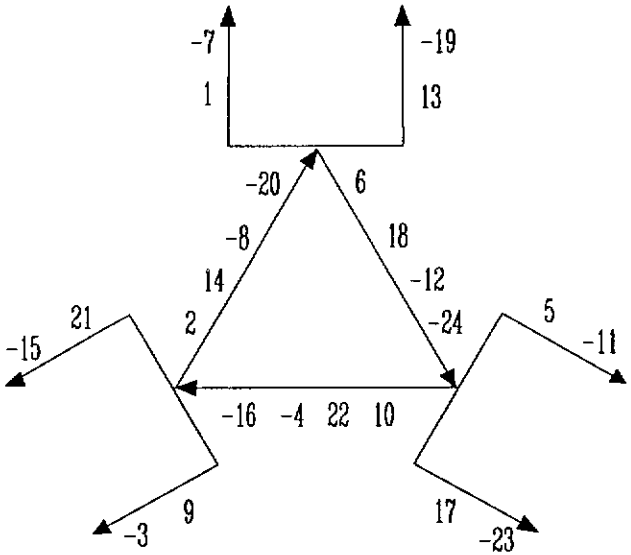
(b)

Fig. 2.8 Star-delta mixture series connection of a 3-phase winding

EMB=30°, p=4 and Z=24

Based on the above, two types of star-delta mixture connection winding can be formed, as shown in Fig. 2.8. Fig. 8(a) shows non-uniform-constitution and Fig. 2.8(b) shows uniform-constitution. Now, the slot distribution can be directly found from Fig. 2.8. The pole pitch is $\tau = \dfrac{24}{4} = 6$. Since it is full-pitch winding the coil span has the same slot distance 6. It is seen that star and delta components under one pole have the equivalent winding width of 30 electrical degree respectively, or 1 coil side. So, CSG of each component under two pair-poles contains two coils. Keeping a phase sequence ABC, the slots allotted to the three phases are listed in Table 2.1.

Table 2.1   Slot distribution for 4-pole, 24-slot

	Star	Delta
Phase A	1-7, 13-19	2-8, 14-20
Phase B	5-11, 17-23	6-12, 18-24
Phase C	9-3, 21-15	10-4, 22-16

Starting phase-A star-component in slot 1, coil side 1 is connected to coil side (1+6)=7 to form the 1st coil and the 2nd coil consists of coil side 13 and 19. Then phase-A delta-component has the 1st coil consisting of coil side 2 and 8 and the 2nd coil owning coil side 14 and 20. So, phase A winding can be obtained by connecting the 4 coils in order. Similarly, coil sides 6-12, 18-24, 5-11 and 17-23 are connected to form phase B winding, and coil sides 10-4, 22-16, 9-3 and 21-15 are connected to form phase C winding. It should be noticed that the difference between the connection of star component for Fig. 2.8(a) and Fig. 2.8(b).

2.4.2 4-Pole Winding in 36 Slots

Example 2: To design a winding with p = 4 and Z = 36.

Following the procedure of the previous example, the EMS diagram to give every coil-side the attribute of star ($\curlywedge$) or delta ($\triangle$) is drawn as shown in Fig. 2.9.
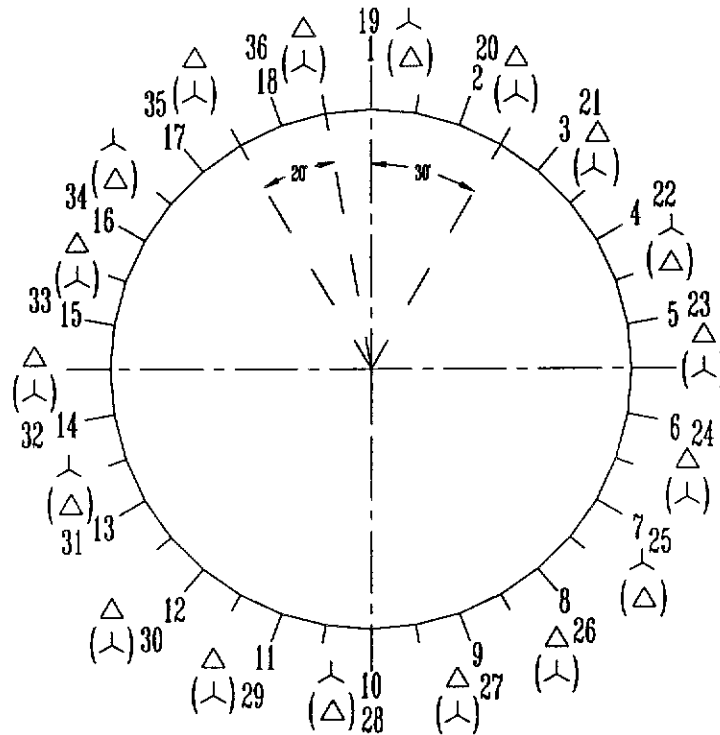
Fig. 2.9   EMS diagram of a winding with p=4 and Z=36

As the slot-pitch is 20° electrical angle, the possible narrowest EMB is 20° electrical angle. Thus, one UCSG consists of a coil-side. To satisfy the condition of displacement of 30° electrical angle between star and delta components, the attribute is arranged as $\curlywedge$-$\triangle$-$\triangle$ or $\triangle$-$\curlywedge$-$\curlywedge$ shown in brackets. Further modification of the EMS diagram, the Fig. 2.9 can be transferred to a final Star-delta component diagram

as shown in Fig. 2.10. Fig. 2.10 is useful to deduce the connection configuration of the new winding. By checking the arrangement of Fig. 2.10 in accordance with the rule mentioned in 2.3.1, it is seen that an exact displacement of 30° between the star and delta component of the same phase and a displacement of 120° exists between the three star and delta component windings respectively. Thus, a completely symmetrical 3-phase winding has been formed for this design.
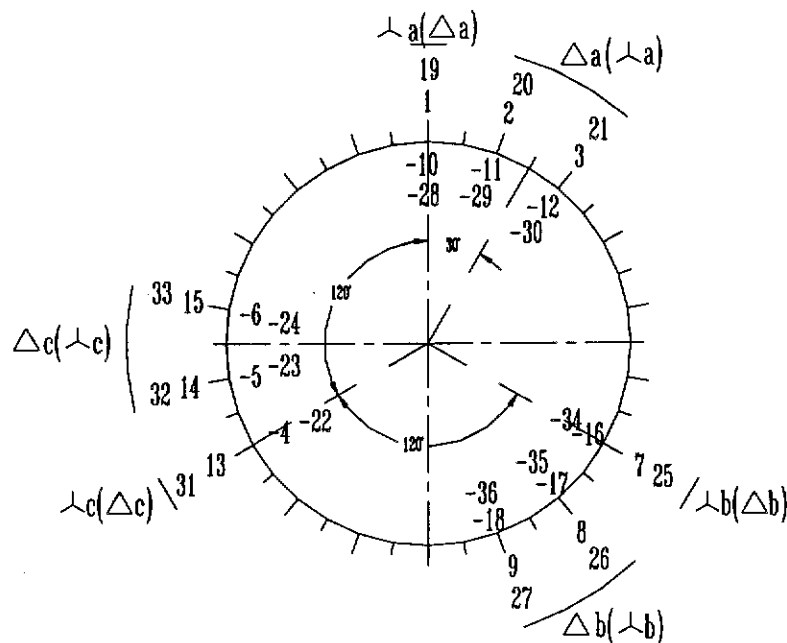
Fig. 2.10   Star-delta component diagram with EMB=20°, p=4 and Z=36

Using a derivation similar to that in the former example, four types of SDSC winding can be formed as shown in Fig. 2.11 and Fig. 2.12. Out of that, the Fig. 2.11(a) and Fig. 2.12(a) are called the non-uniform-constitution and the Fig. 2.10(b) and Fig. 2.11 (b) are the uniform-constitution.
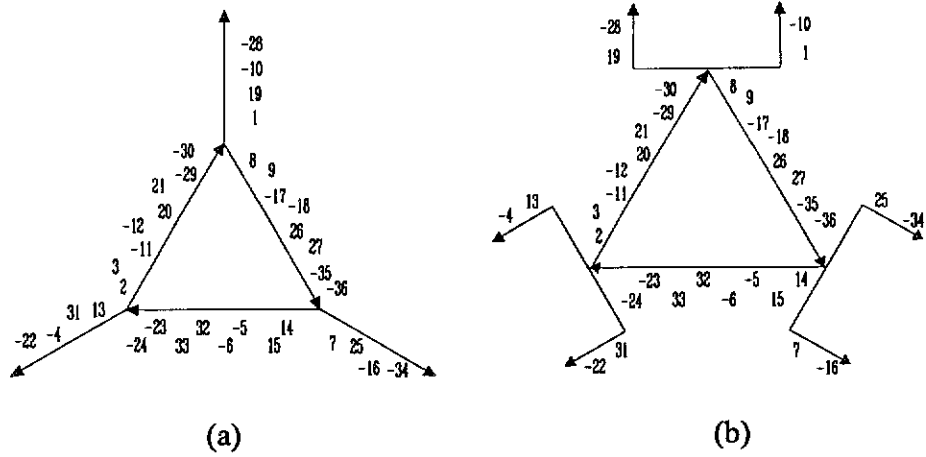
Fig. 2.11   Star-delta mixture series connection of a 3-phase winding
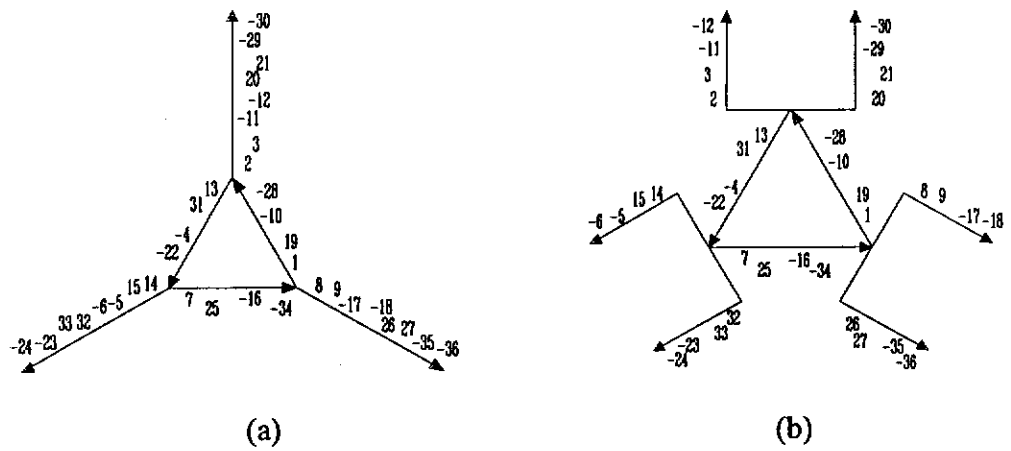
EMB=20°, p=4 and Z=36

Fig. 2.12   Star-delta mixture series connection of a 3-phase winding

EMB=20°, p=4 and Z=36

In this case of Fig. 2.11, the delta component windings contain twice the number of coils as the star component windings. But in the case of Fig. 2.12, the arrangement is reversed.

Take the Fig. 2.11(a) and (b) as the examples to deduce the slot distribution. Since

the full-pitch is the pole pitch: $\tau = \dfrac{36}{4} = 9$. The coil span has the slot distance 6. In

this case the star and delta components have the different winding width. Under one

pole, the star occupies 20 electrical degree or 1 coil side, and the delta 40 electrical

degree or 2 coil sides. So, the CSG of star component in one phase has two coils

cross two pair-poles, and the CSG of delta component in one phase four coils cross

two pair-poles. Three phases are symmetrical. Keeping a phase sequence ABC, the

slots allotted to the three phases are listed in Table 2.2.

Table 2.2   Slot distribution for 4-pole, 36-slot

	Star component	Delta component
Phase A	1-10, 19-28	2-11, 3-12, 20-29, 21-30
Phase B	7-16, 25-34	8-17, 9-18, 26-35, 27-36
Phase C	13-4, 31-22	14-5, 15-6, 32-23, 33-24

Starting phase-A star-component in slot 1, coil side 1 is connected to coil side

(1+9)=10 to form the 1st coil, and the 2nd coil consists of coil side 19 and 28. Then

phase-A delta-component has the 1st coil consisting of coil side 2 and 11, the 2nd

coil consisting of coil side 3 and 12, the 3rd coil consisting of coil side 20 and 29,

and the 4th coil consisting of coil side 21 and 30. So, phase A winding can be

obtained by connecting the 6 coils in order. Similarly, phase B and phase C windings

can be obtained. One should pay attention to that the two coils of star component are

connected in series in Fig. 2.11(a), and in parallel in Fig. 2.11(b).

2.5 Conclusion

As it interpreted in this chapter, a conventional 3-phase winding has, in effect, a 6-phase distribution. Every one sixth of the total electrical spacing is occupied by each phase, i.e. 60 electrical degrees. By means of Star-Delta mixture in series connection, a standard, 60°-spread winding can be converted to a quasi-12-phase winding operating from a normal three-phase supply. It will be shown in chapter three that a higher spread factor and lower M.M.F. harmonic can be achieved through the increase of the effective number of phases.

The new winding has two advantages. Firstly, as every phase winding is subdivided into two components with optimized EMB, a higher spread factor can be obtained. Secondly, as the two component windings have a space displacement of 30° electrical angle, the harmonic content of the magnetic field can be effectively reduced. It is seen that the star-delta mixture connection winding has advantage over the conventional winding. Also, the star-delta series connection overcomes the shortcomings in star-delta parallel connection. Hence, the star-delta mixture series connection is an important principle of the new winding.

The new winding principle and the design procedures have been illustrated by two examples. Flexible selection of EMB and appropriate arrangement of EMS diagram are two important means to realize the optimization of the new winding. Usually a narrow EMB is preferred. Although it is required that the delta component should contain $\sqrt{3}$ times as many effective turns per phase as star component, a slight difference is allowed in practice because of discretization of wire sizes. This does not

cause any significant problem in the new machines due to the advantage of star-delta series connection. The new winding can be manufactured as a single layer, and it is easy to determine slot combination. Employing this full-pitch coil can increase the utilization coefficient of slot area. The shorter coil-span may reduce the DC resistance of the winding.

The new winding has two different types; one is non uniform-constitution and the other uniform-constitution. Both these methods are suited for the mass production. So far as the winding connections are concerned, the new winding is quite straightforward. Although the uniform-constitution consists of two different coils and the end connections are slightly more complex than conventional one, it is expected to cause increase in labor costs.

2.6 References

[2.1] Broadway, A.R.W. and Rodriguez, J.L., (1981), "Delta-star PAM", IEE Proc.-B, **128**, (5), pp. 255-259.

[2.2] Hughes, A., (1970), "New 3-phase winding of low M.M.F.-harmonic content", Proc. IEE, **117**, (8), pp. 1657-1666.

[2.3] Rawcliffe, G.H., Burbridge, R.E. and Fong, W., (1958), "Induction motor speed-changing by pole-amplitude modulation", Proc. IEE, **2597L**, (8), 105A, pp. 411-419.

[2.4] Chen, J.Y. and Chen, C.Z., (1998), "Investigation of a new AC electrical machine winding", IEE Proc.-B, Electr. Power Appl., **145**, (2), pp. 125-132.

[2.5] Chen, J.Y. and Chen, C.Z., (1988), "Magnetic-space 3-phase AC electrical machines and its starting circuit", China Patent, No.88218352.4.

[2.6] Chen, C.Z. and Chen, J.Y., (1981), 'The winding of AC electric machine in Electromagnetic Space' (I) (in Chinese), China Electrical Equipment, (3/4), pp.52-63.

[2.7] Chen, J.Y. and Chen, C.Z., (1982), 'The winding of AC electric machine in Electromagnetic Space' (II)(in Chinese), China Electrical Equipment, (2), pp.1-21.

[2.8] Chidambaram, P., Achutha Kamath, A., Subbiah, M. and Krishnamurthy, M.R., (1983), "A new pole-changing winding using star/star-delta switching", IEE Proc., Vol. 130, Pt. B, No. 2, (3), pp. 130-136.

[2.9] Rajaraman, K.C., and Betigeri, K.G., (1982), "Optimum design of 2:1 pole-changing motor", IEE Proc., Vol. 130, Pt. B, No. 2, (3), pp. 130-136.

Appendix II-1

An Example of a Conventional Winding Configuration with 4 Poles and 36 Slots

In this Appendix, a conventional three-phase AC winding with 4 poles and 36 slots is presented. It is assured that winding is laid out in single layer, wave winding with full-pitch coils.
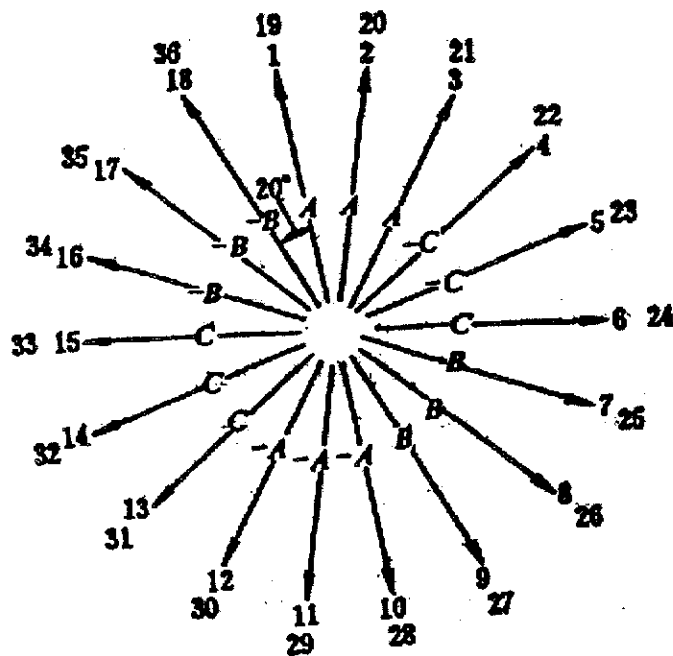
Fig. A2.1.1   Slot EMF star for pole=4 and slot =36

The slot EMF star diagram is shown in Fig. A2.1.1. Every number from 1 to 36 represents an EMF of one coil side in one slot. The phase displacement of the slots can be noted in Fig. A2.1.1. With the help of this diagram, all of the coil sides are

assigned to the three phases A, B, and C. The resultant EMFs of the 3-phase winding must be symmetrical and the phase shift between the three phase windings must be 120°.

The pole pitch is $\tau = \dfrac{36}{4} = 9$. Since it is a full-pitch winding, the coil span has the same slot distance 9. The number of slots per pole per phase is $q = \dfrac{36}{3 \times 4} = 3$. So, a coil-group under one pair-pole contains three coils. Keeping a phase spread = 60° and a phase sequence ABC, the slots allotted to the three phases are listed in Table A2.1.1.

Table A2.1.1 Slots distribution

Phase A	1,2,3	-10,-11,-12	19,20,21	-28,-29,-30
Phase B	7,8,9,	-16,-17,-18	25,26,27	-34,-35,-36
Phase C	-4,-5,-6	13,14,15	-22,-23,-24	31,32,33

Starting phase A in slot 1, coil side 1 is connected to coil side (1+9)=10 to form the 1st coil. Then the 2nd coil consists of coil side 2 and 11, and the 3rd coil side 3 and 12. So, one coil-group under one pair-pole in phase A can be obtained by connecting the three coils in order. Similarly, coil sides 19, 20, 21, 28, 29 and 30 are connected to form another coil-group of phase A. Thus, the phase A winding can be completed by connecting the two coil-groups to obtain the maximum EMF, with two terminals *A* and *X* as shown in Fig. A2.1.2.

Following the similar procedure phase B and C windings can be completed with our

terminal *B-Y* and *C-Z*. Fig. A2.1.2 shows the whole three-phase winding diagram.

Angle between slot $\alpha = \dfrac{4 \times 180}{36} = 20°$. Thus the start of phase B lies 120/20=6 slots

away from that of phase A i.e., in slot 7 and that of phase C lies in slot 13.
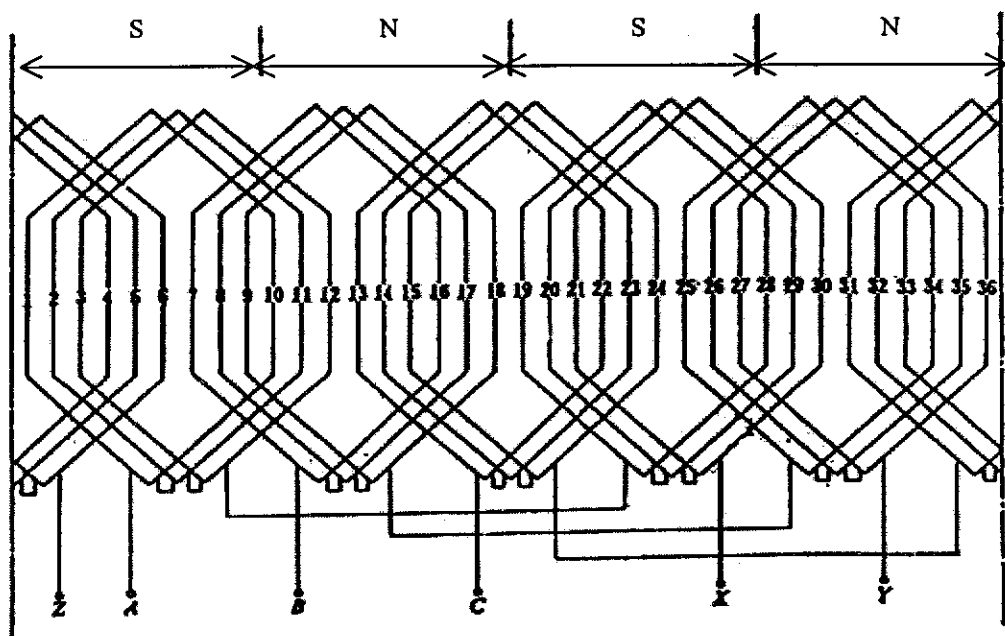
Fig. A2.2   Three-phase winding diagram for P=4 and slot=36

An example of a Conventional Winding Configuration with 4 Poles and 24 Slots

The design of the counterpart of conventional winding is given here.

Slots per pole per phase $q = \dfrac{24}{3 \times 4} = 2$. The slot EMF star diagram is shown in Fig.A2.2.1.
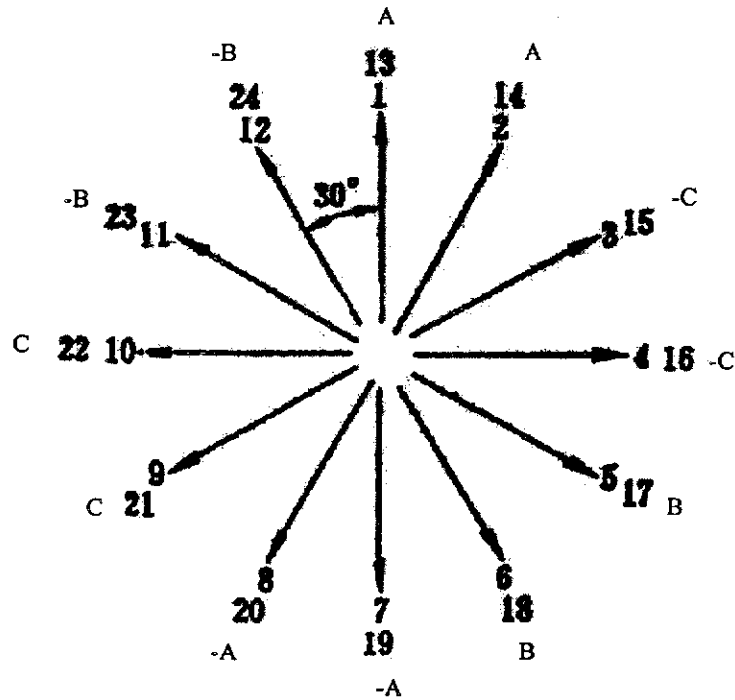
Fig. A2.2.1   Slot EMF star for pole=4 and slot =24

Pole pitch $\tau = \dfrac{24}{4} = 6$. As a full-pitch winding the coil span take the same number of

slot. This is an even number and hence winding is not possible with a coil span of 6

slots. A coil span of 5 slots is an alternative.

The slots allotted to three phases are list in Table A 2.2.1.

Table A2.2.1 Slots distribution

Phase A	1,2	-7,-8	13,14	-19,-20
Phase B	5,6	-11,-12	17,18	-23,-24
Phase C	-3,-4	9,10	-15,-16	21,22

The whole winding is connected in mush armature. Fig. A2.2.2 shows the winding

diagram for phase A only. The winding for other two phases may be similarly

completed.
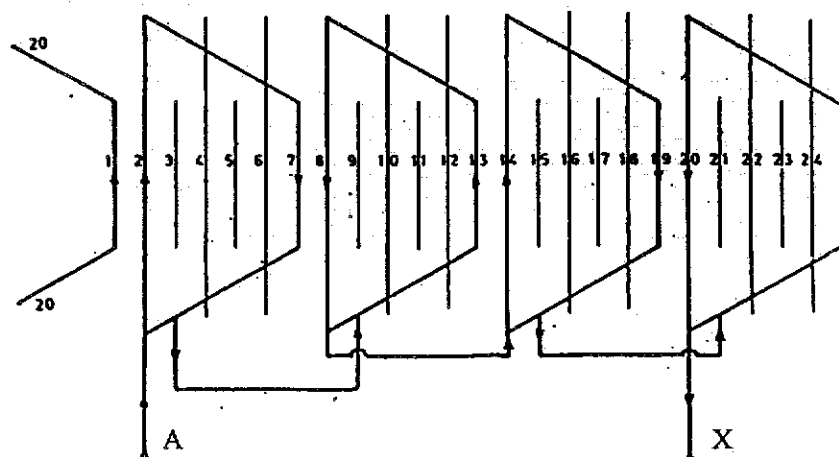
Fig. A2.2.2 Three-phase winding diagram for P=4 and slot=24

MATHEMATICAL ANALYSIS AND EXPERIMENTAL INVESTIGATION OF THE NEW WINDING MACHINES

Abstract

This chapter presents a mathematical analysis to verify that the new star-delta in series connection (SDSC) winding designed in accordance with the EMS principle is able to reduce considerably MMF harmonic contents in three-phase induction motors, especially those troublesome ones such as fifth and seventh and so on. Two prototype electric motors were constructed borne on the winding presented in the last chapter. Theoretical analysis shows that the new SDSC winding has a higher fundamental spread factor than a similar conventional winding. Experimental investigation conducted on the prototype induction motor with 36 slots and 4 poles proved that it has higher efficiency and torque compared to a standard motor. The second prototype machine with 24 slots and 4 poles results in an almost the same level of performance of its conventional counterpart, but, with a rotor 15% shorter in size. The two prototype machines aim at achieving different benefits. No-load and load tests were carried out to investigate the effect of the circulating current in the delta component winding of the new winding, mainly caused by third harmonic current. The test results show that the new SDSC winding machine does not cause overheating problem at normal operating condition although the circulating current is inversely proportional to number of turns in the delta winding, which is only a

fraction of the whole winding. However, caution should be paid to no-load operation at excessive voltage.

3.1 Introduction

There is a trend towards increasing flux density in the designing modern induction machines. As the permissible temperature of insulating materials used for both the windings and laminations go up, the operating flux and current density of contemporary induction machines also become progressively higher. A variety of methods [3.1-3.4] have been used for analyzing magnetic field of induction machines. The most noticeable harmonic contents in the magnetic field are the third, fifth and seventh harmonics that usually cause troublesome to electrical machines operation. These harmonics degrade starting torque and output power of machines, and result in higher iron loss and stray loss. The shapes of flux distributions in various sections of an induction machine are interrelated. The most saturated section normally has a flattened shape of flux density distribution. Saturation in an induction machine has two main impacts: a) the proportion of the total available M.M.F. consumed in the iron of the rotor, stator cores and teeth is increased. It results in decreasing the effective fundamental magnetizing reactance. b) when saturation occurs in the teeth but not the core, the previous sinusoidal air-gap flux presents a flattening tendency. As a consequence, an additional flux harmonic appears in the air gap. A similar situation arises when the iron of the stator core, but not the teeth, is saturated, the air gap flux assumes a peak shape.

By reducing the harmonic contents in AC machines, it is possible to increase their efficiency and output. The new SDSC winding configuration is aimed at to achieve lower harmonic content in three-phase AC electrical machines.

As it interpreted in the last chapter, a conventional 3-phase winding has, in effect, a 6-phase distribution. Every one sixth of the total electrical spacing is occupied by each phase, i.e. 60 electrical degrees. The new SDSC 3-phase winding enable to obtain almost twice the spread, each component occupying much smaller part of the total electrical degrees. The new winding is considerable superior to the conventional 120° spread winding both in terms of its 'effectiveness' as measured by the distribution factor and in terms of its harmonic content. The star-delta arrangement is a good improvement on the 60° spread winding. It is, in effect, a 12-phase winding. In the theoretical analysis [3.5], the comparison of M.M.F. harmonic produced by the new winding and conventional winding shows that the star-delta winding has a substantially lower harmonic content. The experimental results [3.5][3.6] of the prototype also prove that.

There are several factors can influence the magnetic field distribution in the air gap of an electric machine. In order to facilitate a survey of the relations that follow, and to avoid unnecessary mathematical complexity, certain simplifying assumptions have been made. The assumption of infinite relative permeability of iron ($\mu_r = \infty$) is the main simplifying condition throughout the entire work. However, the relative permeability of iron is considered to be finite if the effect of iron saturation is dealt with for accurate analysis. All harmonics are referred to the entire bore of the machine, i.e. the fundamental harmonic of the order $v = 1$ forms one pair-pole corresponding to the periphery angle 2π. If the machine has p par-poles the harmonic producing a magnetic field with p pair-poles is called the working harmonic. This

harmonic is always of the order $v = p$. An arbitrary harmonic of the vth order forms v pair-poles. To one pair-pole of this harmonic corresponds the periphery angle $2\pi/v$.

In this chapter all magnetic field calculation performance as for two-dimensional field without considering boundary and end effects.

3.2   Analysis of Harmonic Content of M.M.F.

A general expression for the magnetic field produced by a three-phase SDSC winding is derived in this section and followed by comparison of amplitudes of MMF harmonics between the SDSC and standard windings.

3.2.1 Harmonic Content of The New Winding

The amplitude of the vth harmonic M.M.F. produced by a symmetrical 3-phase winding is given by [3.8]:

$$F_v = \frac{6\sqrt{2}}{\pi} \frac{W K_{dv} K_{pv} I}{vp} \quad \text{A/pole} \tag{3.1}$$

where,

v = harmonic order

p = number of poles

K_{dv} = spread factor of vth harmonic

K_{pv} = chord factor of vth harmonic

W = number of turns in series per parallel branch per phase

I = phase current

54

Equation (3.1) can be modified for the new SDSC winding. The parameters or variables of SDSC winding should be considered for the star and delta two different components. So, the subscripts Y and Δ stand for the star and delta components respectively. The item W becomes W_Y and W_Δ in the modified equations, referred to the number of turns in series in each parallel branch per phase for star and delta components respectively. I is changed into I_Y and I_Δ for the phase current in the two components. $K_{dv\text{-}Y}$ and $K_{dv\text{-}\Delta}$ express the vth-harmonic spread factor of the two components. As the new winding can be laid out as a single-layer winding, its chord factor is always equal to 1. Thus, K_{pv} can be omitted from the equations.

From the equation (3.1), the amplitude of the vth harmonic M.M.F. produced by the delta component of mixed winding is given by

$$F_{v\Delta} = \frac{6\sqrt{2}}{\pi} \frac{W_\Delta K_{dv\text{-}\Delta}}{vp} I_\Delta$$

$$= \frac{CI_\Delta}{v} W_\Delta K_{dv\text{-}\Delta} \qquad \text{A/pole} \qquad (3.2)$$

where,

$$C = \frac{6\sqrt{2}}{\pi p}$$

The amplitude of vth harmonic M.M.F. produced by star component of the winding is given by

$$F_{\nu Y} = \frac{CI_Y}{\nu} W_Y K_{d\nu-Y} \qquad \text{A/pole} \qquad\qquad (3.3)$$

When current flows through the SDSC winding, both delta and star winding components produce a series of νth harmonic M.M.F. Where, $\nu = 6k\pm1$ and k is a positive integer such as 1, 2, 3, ... But 3rd-harmonic M.M.F. does not appear in these harmonic series.

Let the current in the two winding components be expressed as

$$i_\Delta = \sqrt{2} I \sin\omega t \qquad\qquad (3.4a)$$

and

$$i_Y = \sqrt{2}\sqrt{3} \sin(\omega t - \pi/6) \qquad\qquad (3.4b)$$

According to equation (3.2) and (3.4a), the equation for the $\nu(=6k\pm1)$th harmonic MMF produced by the delta-connected winding is:

$$F_{(6k\pm1)\Delta} = \frac{CI}{6k\pm1} W_\Delta K_{d\nu-\Delta} \sin[(6k\pm1)\frac{x}{\tau}\pi \mp \omega t] \qquad\qquad (3.5)$$

where,

τ = pole-pitch of the winding

x = position in space

To obtain the (6k±1)th harmonic M.M.F. produced by the star-connected winding, it must take account of the displacement between the two winding components, and the time-phase shift of current. Thus, the equation is given by

$$F_{(6k\pm1)Y} = \frac{CI}{6k\pm1}\sqrt{3}W_Y K_{dv-Y} \sin[(6k\pm1)(\frac{x}{\tau}\pi - \frac{\pi}{6}) \mp (\omega t - \frac{\pi}{6})]$$

$$= \frac{CI}{6k\pm1}\sqrt{3}W_Y K_{dv-Y} \sin[(6k\pm1)\frac{x}{\tau}\pi \mp \omega t - k\pi] \qquad (3.6)$$

Optimization of E.M.B. and arrangement of coil-sides in star-delta series connection are important means to reduce harmonic content. Four factors, from equation (3.5) and (3.6), can be considered:

(a)   The item '-kπ' in the right side of equation (3.6) is just a phase displacement of kπ between the (6k±1)th harmonic M.M.F.s produced by the star and delta component winding. When k is odd, the two harmonic components of M.M.F. weaken each other. When k is even, they enhance each other. So, half of the (6k±1)th harmonic M.M.F.s can be reduced considerably.

(b)   The spread factor K_{dv} is used to reduce the other half of (6k±1)th harmonic M.M.F.. By optimizing E.M.B. and its distribution in space, when k is even, a special spread factor is obtained so that the other half of (6k±1)th harmonic M.M.F.s produced by the two components winding is reduced instead of enhancing each other.

(c)   Being in cooperation with the factor (a) and (b), optimization of the number of turns in series per phase of the two components of the winding, W_Δ and W_Y, reduces the (6k±1)th harmonic M.M.F.

(d)   By use of different values of phase current I_Δ and I_Y, a reasonable arrangement for all coil-sides and their combinations can also effectively weaken all orders of harmonics, irrespective of whether it is non-uniform-constitution or uniform-constitution.

3.2.2 Harmonics Calculation and Comparison

To analyze harmonic content of the new winding, the two detailed examples previously described in last chapter are employed.

3.2.2.1   30°-E.M.B. winding

In the example 1 of *2.4.1*, slot-pitch is $\alpha = 30$ electrical degrees and the number of coil-side per group is $q_\Delta = q_Y = 1$. Thus, the spread factors of vth harmonic of the delta and star components winding are

$$k_{dv-\Delta} = \frac{\sin v q_\Delta \frac{\alpha}{2}}{q_\Delta \sin v \frac{\alpha}{2}} = \frac{\sin v 15^\circ}{\sin v 15^\circ} = 1 \qquad (3.7a)$$

and

$$k_{dv-Y} = k_{dv-\Delta} = 1 \qquad (3.7b)$$

As it is single-layer winding, the total number of coil-side per phase is 8. The number of coil-side of each component is thus 4, so that both have 2 coils per phase. This is single-$\curlywedge$ and single-$\triangle$ non-uniform-constitution, which corresponds to the one shown in Fig. 2.8a. Let the number of turns for each coil in delta component winding be $W_{z\Delta} = W_z$ and in star component $W_{zY} = W_{z\Delta}/\sqrt{3} = W_z/\sqrt{3}$. Thus, $W_\Delta = 2\,W_z$ and $W_Y = 2\,W_z/\sqrt{3}$. Also, suppose that the current $I_\Delta = I$.

Substituting the above values into equation (3.5) and (3.6), the amplitude of vth harmonic M.M.F. produced by the whole winding is obtained as

$$F_{(6k\pm1)\Delta+Y} = \frac{CI}{6k\pm1}(W_\Delta k_{dv-\Delta} + \sqrt{3}W_Y k_{dv-Y})$$

$$= \frac{CI}{6k\pm1}\left(2W_z + 2\frac{W_z}{\sqrt{3}}\sqrt{3}\right)\times 1$$

$$= \frac{4CIW_z}{6k\pm1} \qquad \text{A/pole} \qquad (k = \text{even}) \qquad (3.8)$$

and

$$F_{(6k\pm1)\Delta+Y} = \frac{CI}{6k\pm1}\left(2W_z - 2\frac{W_z}{\sqrt{3}}\sqrt{3}\right)\times 1$$

$$= 0 \qquad \text{A/pole} \qquad (k = \text{odd}) \qquad (3.9)$$

If this winding is delta connected in a conventional 60° phase belt (also single-layer) its spread factor of vth harmonic M.M.F. is given by

$$K_{dv(60°)} = \frac{\sin vq\dfrac{\alpha}{2}}{q\sin v\dfrac{\alpha}{2}} = \frac{\sin v 30°}{2\sin v 15°}$$

As the total coils of this winding is 12, the number of coils per phase is 4. Let the number of turns for each coil be W_z. Thus, the total number of turns in series per phase is $4W_z$. Also, it is supposed that the phase current of 60°-phase belt winding is equal to the phase current of the delta component of the new winding. Thus, the amplitude of (6k±1)th harmonic M.M.F. of this winding is:

$$F_{(6k\pm1)60°} = \frac{CI}{6k\pm1} \times \frac{\sin(6k\pm1)30°}{2\sin(6k\pm1)15°} \times 4W_z \qquad \text{A/pole} \qquad (3.10)$$

From equation (3.8), (3.9) and (3.10), the ratio of amplitudes of (6k±1)th harmonic M.M.F. produced by the new and conventional windings, expressed in '$K_{e/m}$', can be obtained as

$$K_{e/m(6k\pm1)} = \frac{2\sin(6k\pm1)15°}{\sin(6k\pm1)30°} \qquad (k = \text{even}) \qquad (3.11a)$$

and

$$K_{e/m(6k\pm1)} = 0 \qquad (k = \text{odd}) \qquad (3.12a)$$

Because $|\sin(6k\pm1)30°| = 0.5$ and $|2\sin(6k\pm1)15°| = 0.51764$, the equation (3.11a) and (3.12a) are identical to the equations below,

$$K_{e/m(6k\pm1)} = 1.0353 \qquad (k = \text{even}) \qquad (3.11b)$$

and

60

$$K_{e/m(6k\pm1)} = 0 \qquad\qquad (k = odd) \qquad\qquad (3.12b)$$

The above is the form of 30° E.M.B. winding, namely the delta and star components occupy half of the original 60° phase belt. The equation (3.11b) and (3.12b) show the ratio of the amplitude of (6k±1)th harmonic M.M.F. between this type of winding and 60° phase belt winding. It is seen, from the $K_{e/m}$, that when k is odd the (6k±1)th harmonics are vanished and when k is even the (6k±1)th harmonics M.M.F.s produced by the new winding are 3.53% larger than by 60° phase belt winding. This is the feature of 30° E.M.B. winding.

3.2.2.2   20° -E.M.B. winding

In the example 2, p = 4, Z = 36 and E.M.B. = 20°. It is supposed that the winding be connected in series of single-$\curlywedge$ and single-$\triangle$, as shown in Fig. 2.11a. It is non-uniform-constitution and single-layer winding. So, $\alpha = 20°$, $q_\Delta = 2$, $q_Y = 1$. Let $W_\Delta = 4W_z$, $W_Y = 2W_z/\sqrt{3}$ and $I_\Delta = I$. The spread factor can be obtained

$$K_{dv\text{-}\Delta} = cos\nu 10°$$

$$K_{dv\text{-}Y} = 1 \qquad\qquad (3.13)$$

and the resultant amplitude of (6k±1)th harmonic is

$$F_{(6k\pm1)\Delta+Y} = \frac{CI}{6k\pm1}\left(4W_z \cos\nu 10° \pm \frac{2W_z}{\sqrt{3}} \times \sqrt{3} \times 1\right)$$

$$= \frac{2CIW_z}{6k \pm 1}[2\cos(6k \pm 1)10° \pm 1] \qquad \text{A/pole} \qquad (3.14)$$

If the above winding is designed in 60° phase belt and connected in delta, its spread factor of (6k±1)th harmonic is given by

$$K_{dv} = \frac{\sin v q \dfrac{\alpha}{2}}{q \sin v \dfrac{\alpha}{2}} = \frac{\sin v 30°}{3 \sin v 10°}$$

It is provided that this conventional winding is in single layer and its phase current is equal to the current of the delta component of new winding. Thus, the amplitude of harmonic M.M.F. of it is given by

$$F_{(6k \pm 1)60°} = \frac{6CIW_z}{6k \pm 1} \frac{\sin(6k \pm 1)30°}{3 \sin(6k \pm 1)10°}$$

$$= \frac{2CIW_z}{6k \pm 1} \frac{\sin(6k \pm 1)30°}{\sin(6k \pm 1)10°} \qquad \text{A/pole} \qquad (3.15)$$

From the equation (3.14) and (3.15), the ratio of the amplitude of harmonic M.M.F. produced by new and conventional winding is obtained

$$K_{e/m(6k \pm 1)} = \frac{[2\cos(6k \pm 1)10° \pm 1]\sin(6k \pm 1)10°}{\sin(6k \pm 1)30°}$$

as $|\sin(6k \pm 1)30°| = 0.5$

$$K_{e/m(6k\pm1)} = 2[\sin(6k \pm 1)20^\circ \pm \sin(6k \pm 1)10^\circ] \tag{3.16}$$

So far as the note of "±" before the '1' in the right hand of the equation (3.16); "+" is used when k is even, and "-" is used when k is odd. This is another ratio form of harmonic M.M.F. between the two windings.

Table 3.1   Comparison of harmonic M.M.F.s for motors; p=4, slot=36.

Harmonic order	New star-delta winding	Conventional winding	Ratio $K_{e/m}$
1	2.9696155	2.8793852	1.031337
5	0.0571150	0.1305407	0.437527
7	-0.0451371	-0.0760127	0.593810
11	0.0287236	-0.0483717	-0.593810
13	-0.0219673	0.0502080	-0.437527
17	-0.1746833	0.1693756	-1.031337
19	-0.1562956	0.1515466	-1.031337
23	-0.0124163	0.0283784	-0.437527
25	0.0126384	-0.0212836	-0.593810
29	-0.0108952	-0.0183479	0.593810
31	0.0092121	0.0210550	0.437527
35	0.0848462	0.0822681	1.031337
37	0.0802599	0.0778212	1.031337
41	0.0069652	0.0159196	0.437527
43	-0.0073479	-0.0123742	0.593810
47	0.0067225	-0.0113210	-0.593810
49	-0.0058281	0.0133205	-0.437527

Let the constant $2CIW_z$ in equation (3.14) and (3.15) be a unity. The computed amplitude of harmonic M.M.F.s up to 49th produced by the new and conventional

windings and the ratio of the amplitude of the two windings are listed in Table 3.1. As the amplitude of those higher-order harmonic M.M.F. are quite lower compared with the fundamental M.M.F., they could be neglected in the magnetic-field analysis of the machines without any significant impact.

Take the most serious harmonic contents for a survey,

When k = 0,

$$K_{e/m(fundamental)} = 1.0313$$

When k = 1,

$$K_{e/m(5th)} = 0.4375$$

$$K_{e/m(7th)} = 0.5938$$

When k = 2,

$$K_{e/m(11th)} = 0.5938$$

$$K_{e/m(13th)} = 0.4375$$

When k = 3,

$$K_{e/m(17th)} = 1.0313$$

$$K_{e/m(19th)} = 1.0313 \qquad \text{(tooth-ripple)}$$

It is noticeable, from this case of 20°-E.M.B. winding, that the main harmonic contents such as fifth, seventh, eleventh and thirteenth harmonics, which normally cause disadvantages in electrical machines, have been reduced a great of deal by the new winding. These harmonic-M.M.F.s are respectively reduced to 43.75% and 59.38% of the corresponding M.M.F.s of the conventional 60°-phase belt winding. Instead of being weakened, the seventeenth and nineteenth harmonic M.M.F.s are

increased by the same percentages as the fundamental. These tooth ripples can be reduced by using the usual strategy of skew.

3.2.3 Spread Factor of Fundamental M.M.F.

In the above two cases, the spread factors or winding factors of fundamental M.M.F. have been greatly increased.

In the example 1,

for the new winding; $K_{d-\Delta} = K_{d-Y} = 1$

for the conventional winding; $K_{d-60^\circ} = 0.9659$

The spread factor has been increased by 3.53%.

In the example 2,

for the new winding; $K_{d-\Delta} = 0.9848 \text{ and } K_{d-Y} = 1$

resultant $K_{d-(\Delta+Y)} = \dfrac{W_\Delta \times K_{d-\Delta} + W_Y \times K_{d-Y}}{W_\Delta + W_Y} = 0.98987$

for the conventional winding $K_{d-60^\circ} = 0.9598$

The spread factor has been increased by 3.13%. Experimental results will show that the higher spread factor dedicates to the higher efficiency and torque of the SDSC winding machines.

3.3 Experimental Investigation

Prototype AC induction machines with the new winding were built to test their performance. These prototype machines include non-uniform-constitution of single-star single-delta series connection and uniform-constitution of double-star single-delta series connection, as well as the winding types of single-layer full-pitch, double-layer full-pitch and double-layer short-pitch. Fig. 3.1 and 3.2 show the photographs of a 3 kW prototype and its counterpart.

3.3.1 3 KW Induction Motor With 4-Pole and 36 Slots

The main purpose of making this type of motor is to show that motors with the new windings have potential to increase efficiency without reducing the power factor. The prototype machine, based on the original 4AP100L-4 induction motor (product of a local factory in Western Australia), retained all the original geometrical shapes and sizes (including the plinth, shell, core, rotor and slot, etc) except that the stator winding was re-designed. The new motor is designated as $4AP_{ems}100L-4$.

The main dimensions and performance specifications for the two motors are listed in the Table 3.2. It is seen that the new motor has better performances than original one. In particular the efficiency at rated load of 3 kW was increased by 3.76%, from 82.65 % to 85.76%. It is a considerable improvement for saving power energy.

All the test data were acquired from direct-measurement tests on the same dynamometer. Enough points of sample were collected through each test of no-load, full-load and locked-rotor tests. Temperature rise was determined only after the tested machine operated at rated output power for at least 1 hour.
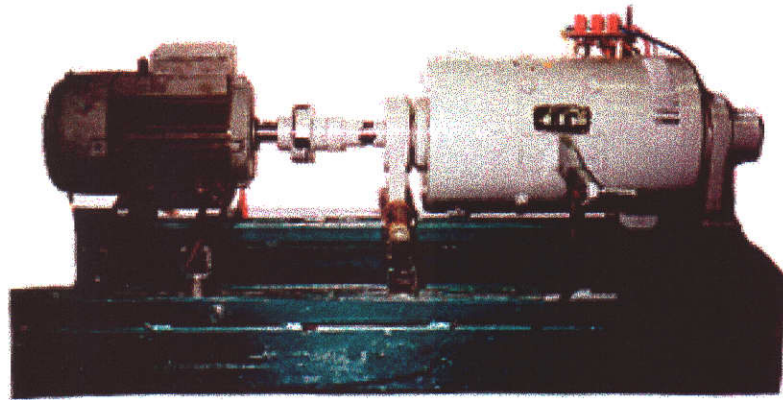
Fig. 3.1   3 kW prototype of 4AP$_{ems}$ on the test bench
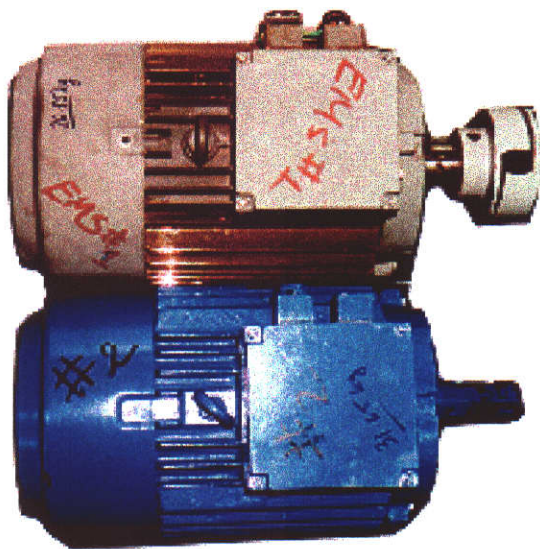
Fig. 3.2   New winding motor and its conventional counterpart

Table 3.2 : Dimensions and performance

Machine	4AP100L-4	4AP$_{ems}$100L-4
Stator core OD	149 mm	149 mm
Stator core ID	97 mm	97 mm
Core axial thickness	135 mm	135 mm
Poles	4	4
Number of slots	36	36
Air gap length	0.25 mm	0.25 mm
3-phase winding connection type	△	⅄
Phase belt / E.M.B.	60° phase belt	20° E.M.B.
Winding layers	1	1
Winding layout	Full-pitch, concentric	Full-pitch, rhombus
Phases	3	3
Frequency	50 Hz	50 Hz
Power output	3 kW	3 kW
Voltage line-line	420 v	420 v
No-load current	3.77 A	3.64 A
Rated current	6.21 A	6.06 A
Winding DC resistance*	6.08 Ω (at 75°C)	5.02 Ω (at 75°C)
Efficiency	82.65%	85.76%
Power factor	80.87%	80.88%
Starting current	42.02 A	43.95 A
Starting torque	49.6 N-m	62.13 N-m
Maximum torque	72.064 N-m	73.03 N-m
Temperature rise	60.87 C°	55.53 C°

*   DC resistance was measured across 2 of 3 output terminals by average of 3

measured data.

Fig. 3.12 shows a comparison of characteristics (efficiency, power factor) versus output power for the new and conventional machines. It is seen that the motor with the new SDSC winding has a higher efficiency than the conventional motor through the output power, while the two power factor curves do not show any significant difference. These results are identical with the theoretical design data.
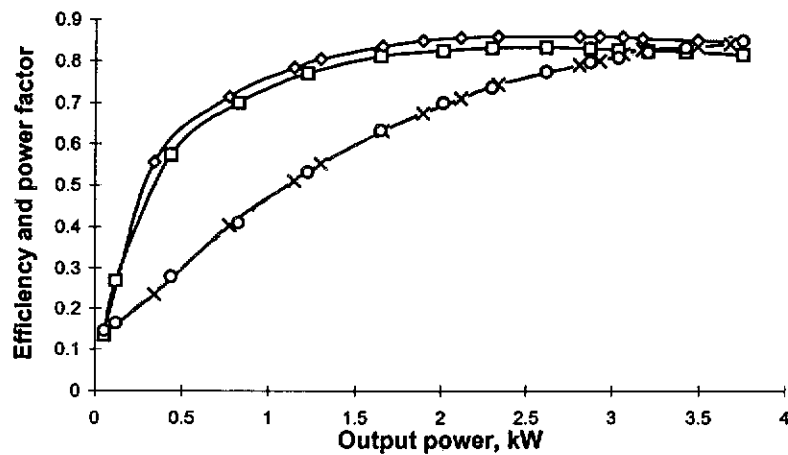
—◇— Efficiency of the new winding motor
—✕— Power factor of the new winding motor
—□— Efficiency of the conventional motor
—○— Power factor of the conventional motor

Fig. 3.12   Output characteristics

Also, the load current drawn by the SDSC winding motor is lower than the conventional motor throughout the variation of the shaft-load, as shown in Fig. 3.13. It shows that the new winding motor requires lower input power while working at the same load condition. The saved power comes from those lower dissipated losses that include iron loss, copper loss and stray loss. The reduced harmonic contents contribute to this result.
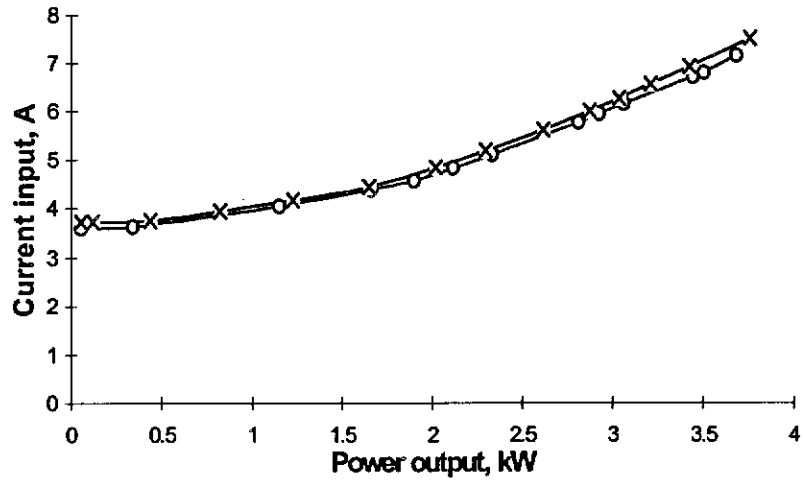
—X— Conventional motor

—O— New winding motor

Fig. 3.13   Input characteristic
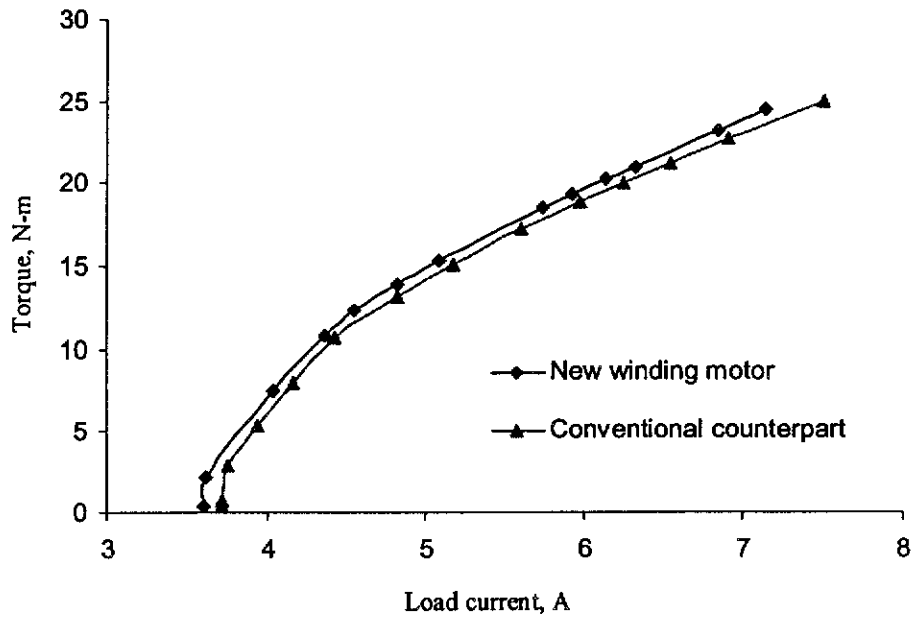
Fig. 3.14   Torque characteristic

To explore the variation of magnetic field with the output load, a full-pitch single coil is separately inserted in the stator core of the new winding motor and the conventional motor. The varied terminal voltages of the coil were recorded throughout the load tests. To make a comparison between them, the two curves are drawn in the same figure as shown in Fig. 3.14b. It is found that the voltage induced in the single coil of the conventional motor dropped down faster along with the load increasing than the new winding motor. When shaft load increased from 50 W to 3.6 kW, single coil voltage of the conventional motor reduced by 129 mV and new winding motor by 112 mV, the ratio of the two being 1.15. As the induced voltage is proportional to the M.M.F. strength, the results display that new winding can produce stronger M.M.F. at the same load.

—◇— New winding motor
—△— Conventional motor
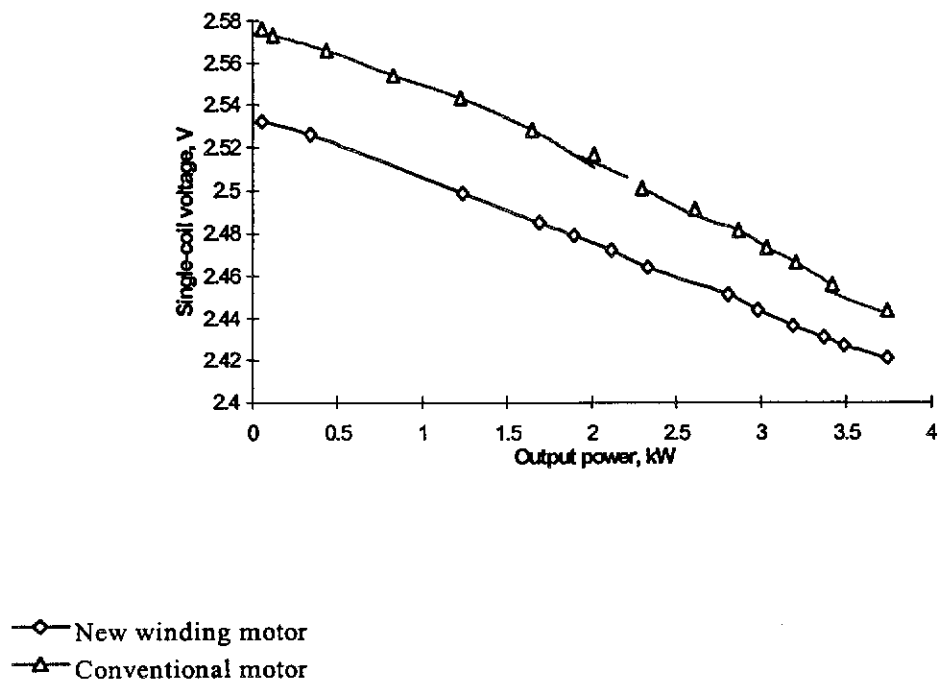
Fig. 3.14b   Single coil characteristic

3.3.2 1.5 KW Induction Motor With 4-Pole and 24 Slots

When this prototype machine was designed, the project aimed at that the new winding motor could save appropriate raw materials while maintaining the motor performance as the same level as the conventional motor. This was requested by the manufacturer to reduce the production cost.

Based on the original Y90L-4 induction motor (Y-series product of a local factory in Shanghai, China), the prototype machine was designed with the original thickness of the core cut down by 15%, while the other original geometrical shape and sizes were keep the same. The stator winding was redesigned and manufactured in accordance with the new winding principle. The new motor was given the new nameplate as $Y_{ems}90L$-4. All the test data were acquired from direct-measurement tests made by an authorized examination institute.

A comparison of the main dimensions and performance between the two motors is detailed in Table 3.3. It is shown that the improved motor maintains an output performance at the same level as the original, although its stator and rotor core are 15% shorter than the original. With the 85% length of original iron core, it is estimated that a variety of effective raw materials were saved as following; 15% of silicon steel; 7~10% of copper; 10% aluminum and 10~13% of insulation material.

Table 3.3 : Comparison of dimensions and performance

Machine	Y90L-4	$Y_{ems}90L$-4
Stator core OD	130 mm	130 mm
Stator core ID	80 mm	80 mm
Core axial thickness	120 mm	120×0.85=103 mm
Poles	4	4
Number of slots	24	24
Air gap length	0.25 mm	0.25 mm
3-phase winding	(Y)	(Δ)
Phase belt / E.M.B.	60° phase belt	30° E.M.B.
Winding layers	1	1
Winding layout	Full-pitch,	Full-pitch,
Phases	3	3
Frequency	50 Hz	50 Hz
Power output	1.5 kW	1.5 kW
Voltage line-line	380 V	380 V
Stray loss	32 W	14 W
No-load current	2.04 A	2.308 A
Rated current	3.65 A	3.69 A
Efficiency	78.74%	79.82%
Power factor	0.793	0.791
I_{st} / I_N	5.34	5.57
M_{st} / M_N	2.87	2.97
M_{max} / M_N	3.27	3.19
M_{min} / M_N	1.7	2.31
Temperature rise	57.9 C°	61.5 C°

The test data show that all of the output performance of the new winding motor has reached the expected results. It is interesting to notice that the new motor had only 14 W of stray loss, whereas the original one had 32 W. The ratio of the two is 43.75%. The reduction in the machine loss is due to lower harmonic content as expected from the theoretical analysis.

3.4   3rd-Harmonic Circulating Current

Like a normal 3-phase winding, the SDSC winding does not produce third harmonic M.M.F. in the air gap in the linear operating region. But, modern induction motors are designed to operate close to the saturation region. Recent years, there is a trend towards increasing the flux density. As the permissible temperatures of insulating materials used for both the windings and laminations go up, the operating flux and current density of contemporary induction motors also become progressively higher. The higher flux densities cause magnetic saturation that produces third-harmonic flux in the magnetic field. This 3rd-harmonic component exists in the air gap flux and causes the flux density waveform to flatten in the top. This results in 3rd-harmonic E.M.F. being induced in each phase winding. These E.M.F.s are co-phase in 3-phase winding and may interact each other to form a threefold 3rd-harmonic E.M.F. in the delta-connected winding component. So that a 3rd-harmonic circulating current is produced to balance out the original 3rd-harmonic M.M.F. Hence, 3rd-harmonic current can always exist in the delta-connected winding. The possible trouble is that the delta-connected winding component is only a fraction of the new winding, while it must induce currents larger enough to substantially wipe out the 3rd-harmonic flux in air gap. This 3rd-harmonic current in delta winding

component may lead to winding temperature rise beyond the normal range. This problem was discussed by the previous research [3.5].

3.4.1 3rd-Harmonic Current at No-Load Condition

The theoretical analysis and experimental results have shown that 3rd-harmonic circulating current in the SDSC winding does not significantly affect the machine performance when the machine operates at normal voltage.

No-load tests were made for the induction motors $4AP_{ems}100L-4$ and $4AP100L-4$. The no-load test data showed that the phase current I_Δ in delta part winding of both motors contained a strong 3rd-harmonic current. The waveforms of the two currents in delta component windings are shown in Fig. 3.15 and the corresponding data is summarized in Table 3.4. It is seen that both currents have a shape of flat top which means motors are operated at saturation condition. Also, it is evident that the new winding can yield a little bit higher 3rd-harmonic current in delta winding component than the conventional one when the motors operate at normal voltage and no-load condition, since there is a hollow at the top of the wave in Fig. 3.15(a). In spite of having a nearly 3% lower input current, the motor $4AP_{ems}100L-4$ had its I_Δ 0.91% higher than the original motor $4AP100L-4$. However, this minor difference does not lead to significant deterioration to the machine performance. The 3-phase windings of the conventional machines are usually connected in single-delta for those induction motors with rated output power above 3 kW. It is seldom to find any noticeable problem due to the high temperature rise since this winding connection was applied in industrial product.
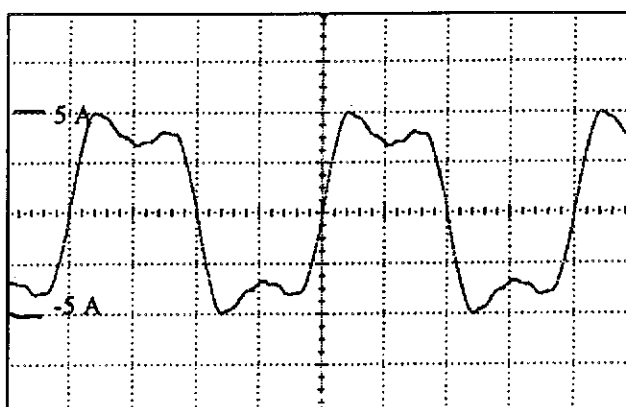
(a)   Motor 4AP_{ems}100L-4
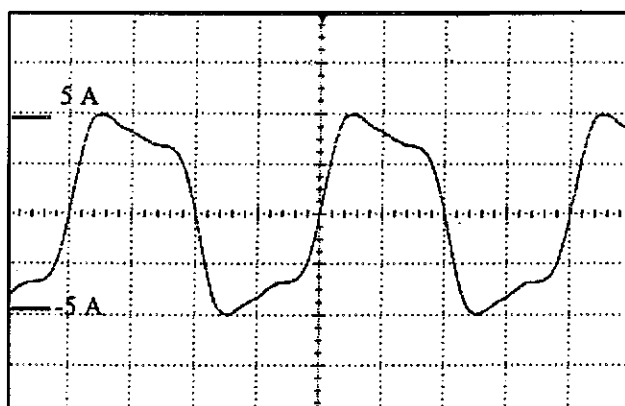
(b)   Motor 4AP100L-4

Fig. 3.15   Current waveform in delta part winding at no-load

Table 3.4:   No-load test data at rated voltage

Motor tested	Voltage input	Current input	Current in delta part
4AP$_{ems}$100L-4	420 V	3.663 A	2.22 A
4AP100L-4	420 V	3.776 A	2.20 A

77

When the motor operates at no-load condition, the input current contains mainly the magnetizing component. The active component is a quite small part of the input VA to meet friction, windage and iron losses. At the moment, the air gap flux is high, the core is deeply saturated and the 3rd-harmonic current in the delta part winding increases in a large amount. Table 3.5 shows those concerned currents data at different voltages in no-load test for motor 4AP$_{ems}$100L-4. Where, I$_{\Delta3}$ is calculated by RMS method. It is supposed that input line current I$_{in}$ is sinusoidal. Thus, there are only fundamental and 3rd-harmonic components presented in I$_{\Delta}$,

$$I_\Delta = \sqrt{I_{\Delta1}{}^2 + I_{\Delta3}{}^2}$$ (3.17)

because of I$_{\Delta1}$ = I$_{in}$ / $\sqrt{3}$, I$_{\Delta3}$ is given by

$$I_{\Delta3} = \sqrt{I_\Delta{}^2 - (I_{in} / \sqrt{3})^2}$$ (3.18)

So, I$_{\Delta3}$ can be calculated by the equation (3.17) and (3.18).

To find out how the I$_{\Delta3}$ possibly cause high temperature rise in the new winding, three indices are employed here; γ_1 = I$_{\Delta3}$ / I$_{\Delta1}$ %, γ_2 = (I$_\Delta$ - I$_{\Delta1}$) / I$_{\Delta1}$ % and the (1 + γ_2)^2 means the heat loss rate.

Table 3.5: No-load currents for motor 4AP$_{ems}$100L-4

Item	Test and calculated data				
V$_{in}$ --- input voltage, V	300	350	400	420	460
I$_{in}$ --- input current, A	1.966	2.464	3.205	3.663	4.879
I$_\Delta$, A	1.147	1.451	1.919	2.221	3.251
I$_{\Delta1}$, A	1.135	1.423	1.85	2.115	2.817
I$_{\Delta3}$, A	0. 166	0.284	0.507	0.678	1.623
$\gamma_1 = I_{\Delta3} / I_{\Delta1}$ %	14.65	19.99	27.38	32.05	57.616
$\gamma_2 = (I_\Delta - I_{\Delta1}) / I_{\Delta1}$ %	1.067	1.978	3.68	5.01	15.41
$(1 + \gamma_2)^2$	1.021	1.04	1.075	1.103	1.332

It is found that when the motor 4AP$_{ems}$100L-4 is operated at rated voltage 420 V, the value of 3rd-harmonic current I$_{\Delta3}$ is 32.06% of the fundamental. The waveform of I$_\Delta$ presents a saturated shape, somewhat similar to a trapezium as shown in Fig. 3.15 (a), with an obvious hollow part at the top of the current waveform. This is caused by a serious 3rd-harmonic current I$_{\Delta3}$. Due to the I$_{\Delta3}$, the heat loss of the delta part windings increased by 15.2%, a not negligible increment. Fortunately, the no-load current I$_{in}$ and delta component winding current I$_\Delta$ are not so high to result in excessive temperature rise, in spite of a large I$_{\Delta3}$.

From Table 3.5, it is seen that when the supply line voltage was increased by 9.52% from 420 V to 460 V, the input current I$_{in}$ increased by 34.4% from 3.63 A to 4.879 A, I$_\Delta$ by 45.6%, and I$_{\Delta3}$ by 104.5%. Due to the enlarged I$_{\Delta3}$, the heat loss of the delta part winding jumped to 1.353 while the temperature rise produced by the delta part winding was a considerable value.
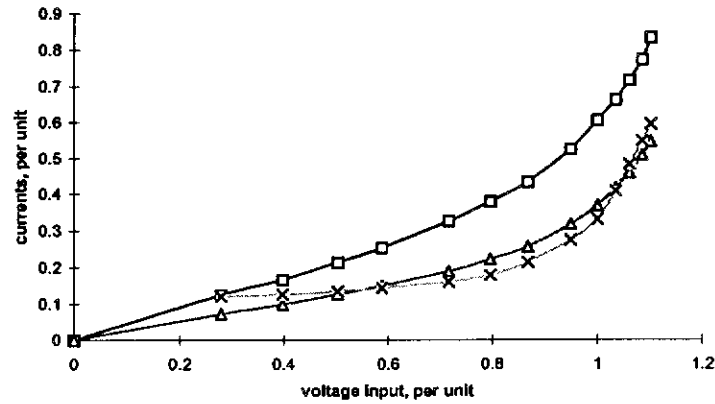
—□— I_{in} input line current

—△— I_Δ phase current in delta part winding

—✕— $I_{\Delta 3}/I_{\Delta 1}$ ratio of 3rd-harmonic current to fundamental

Fig. 3.16   No-load test performance for 4AP$_{ems}$100L-4

Fig. 3.16 shows the curves of no-load currents varying with input voltage in per unit. It is displayed that the curve of $I_{\Delta 3}/$ $I_{\Delta 1}$=f(V_{in}) grows more rapidly and I_Δ increased faster than I_{in} when supply voltage was over the rated value (420 V). Therefore, the winding insulation has a high probability to be damaged while the motor is operating at over voltage range at no-load operation condition. With the same reason, this situation should be taken care of for the conventional 60°-phase belt winding in delta connection. Generally speaking, a proper attention should be paid to the situation when machines are operating at no-load and excessive-voltage conditions.

3.4.2 3rd-Harmonic Current at Load Condition

When the machines are working at load condition, the saturation in the core is distinctly reduced due to the reaction of active load through air gap flux. To investigate this changing tendency load tests were made for the induction motors 4AP$_{ems}$100L-4 and 4AP100L-4. Fig. 3.17 shows the waveform of phase current I_Δ in

delta part winding of the two motors. It is found that the waveform of I_Δ was no more a flat top but changed to a nearly-triangle shape, indicating a greatly reduced fraction of 3rd-harmonic circulating current in delta component winding current I_Δ. It is shown that the new star-delta series connection winding is impossible to be overheat due to the existence of the 3rd-harmonic current in the delta component winding when the machine operates at load, especially at full-load condition.
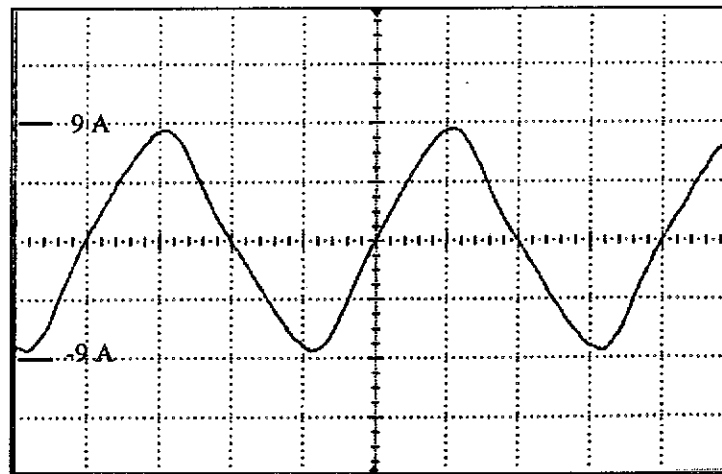
(a) Motor 4AP$_{ems}$100L-4
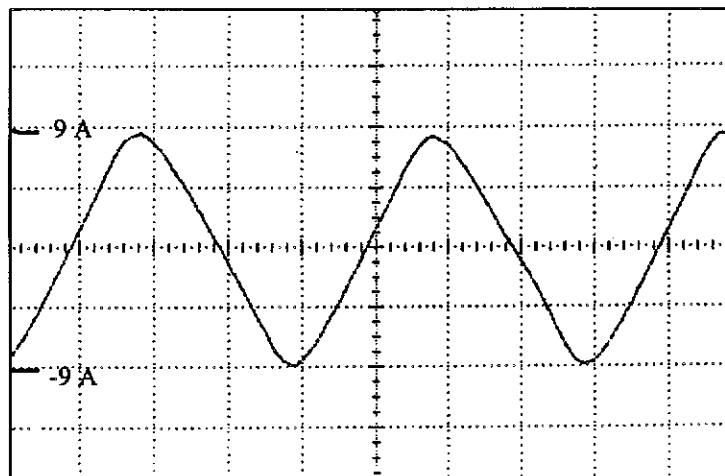
(b) Motor 4AP100L-4

Fig. 3.17 3rd-harmonic current at full-load test

Further quantitative analysis proves the same results. Load tests were carried out for the two induction motors 4AP100L-4 and 4AP$_{ems}$100L-4 to operate at the point very closed to the rated output power of 3 kW. The tested and calculated data related to the currents are listed in Table 3.6. It is seen that the coefficients of γ_1 and γ_2 are 8.66% and 0.3749% for the conventional winding motor, and 12.99% and 0.84% for the new winding motor. As the 3-phase winding connection is changed from single-delta ($\triangle$) to star-delta series connection ($\curlywedge$), the reduction of the number of series turns in the delta component winding results in a larger 3rd-harmonic current $I_{\Delta 3}$ in the new winding so that the phase current I_Δ in delta part of the new winding increased more rapidly due to $I_{\Delta 3}$. The conventional winding had increment of heat loss of 0.75%, and the new winding 1.69%. This is because that the delta component winding of the conventional winding contains the whole coils. But the delta component winding of the new winding only occupies a fraction of 2/3 of the whole coils. In view of the entire winding, the increment of heat loss was 0.75%×1 = 0.75% for the conventional winding, and 1.69% ×2/3 = 1.127% for the new winding. The two values can be regarded as the same level. Naturally, the temperature rise in the new winding is not well distributed. The delta component has a higher temperature rise than the star component. However, the two components winding are packed together by varnished insulation and the thermal conduction is good. Thus, the difference of temperature between the two parts of winding is not significant.

Table 3.6: Comparison of load currents between 4AP100L-4 and 4AP$_{ems}$100L-4

Machines	4AP100L-4	4AP$_{ems}$100L-4
3-phase winding connection type	△	(star-delta symbol)
V_{in} --- input voltage, V	419.6663	418.6667
I_{in} --- input current, A	3.070541	3.093573
I_{Δ}, A	6.33	6.183333
$I_{\Delta 1}$, A	3.6684	3.6
$I_{\Delta 3}$, A	0.3165	0.4638
$\gamma_1 = I_{\Delta 3} / I_{\Delta 1}$ %	8.66	12.99
$\gamma_2 = (I_{\Delta} - I_{\Delta 1}) / I_{\Delta 1}$ %	0.3749	0.84
$(1 + \gamma_2)^2$	1.0075	1.0169

3.5 Conclusions

The essential principles concerning the design of a new three-phase winding have been described with detailed examples. The new star-delta series connection winding has been shown to have obvious advantages comparing with the normal 60° phase-belt winding. With its narrow E.M.B., full-pitch coil and flexible arrangement of coil-side-group for phase winding, the new winding has a higher winding factor and it is possible to reduce harmonic content to a quite low level. Although the ratio of turns between star and delta components should be in $1 : \sqrt{3}$, it is allowed to be adjustable somewhat to suit the discrete sizes of conductors in commercial products without significant impact to the machine performance. Nevertheless, it is very restricted in the delta-star parallel connection winding.

As it interpreted in the last chapter, a conventional 3-phase winding has, in effect, a 6-phase distribution. Every one sixth of the total electrical spacing is occupied by each phase, i.e. 60 electrical degrees. The new SDSC 3-phase winding enable to obtain almost twice the spread, each component occupying much smaller part of the total electrical degrees. The new winding is considerable superior to the conventional 120° spread winding both in terms of its 'effectiveness' as measured by the distribution factor and in terms of its harmonic content. The star-delta arrangement is a good improvement on the 60° spread winding. It is, in effect, a 12-phase winding. In the theoretical analysis [3.5], the comparison of M.M.F. harmonic produced by the new winding and conventional winding shows that the star-delta winding has a substantially lower harmonic content. The theoretical analysis shows that most salient harmonic contents can be reduced to quite low values. In the case with p = 4 and slot = 24, when k = odd the $(6k \pm 1)$ th harmonic is eliminated. The experimental results [3.5][3.6] of the prototype also prove that.

The circulating current yielded in the delta-connected winding was considerably concerned by the previous research [3.7]. Saturation harmonics rotate in the air gap at the synchronous speed with respect to the fundamental flux waveform. Voltages are induced in the stator and rotor windings with frequencies at values of multiples of the stator supply and rotor-slip frequency respectively. These push harmonic current into the supply and can give rise to circulating current in the delta-connected windings, which may occasionally be sufficient to damage the windings. They are responsible for additional noise and core losses that assume greater importance in large machines because of power involved. It has been found in a series of tests that the 3rd harmonic current in the delta component winding could reach a level about

27 percent of the fundamental one at no-load operation. Even though, there was no overheat happened in the test. This was due to the lower no-load current of the new winding motor. When the new motor operated at full-load or higher load condition the 3rd harmonic circulating current dropped down to about 10 percent of the fundamental current. The test results show that the new winding motors do not have high temperature rise caused by 3rd harmonic current when working at normal load range. An attention should be paid to operation at excessive-high voltage condition.

The experimental results of the two different prototype machines demonstrate the new winding merits; either the new winding machine can increase efficiency by more than 3% with respect to the conventional machine, or can save considerable raw materials such as silicon steel sheet by about 15% without worsening performance of the conventional one. The result of lower stray loss displays the lower harmonic contents of new winding contains. The experimental results show that there was no overheat problem caused by the 3rd-harmonic circulating current at normal operation.

The non-uniform-constitution and uniform-constitution of the new winding are not complicated in technology. Especially, the uniform-constitution has almost the same technical procedure in manufacture as the conventional winding.

The design principle and procedure are described through two detailed cases. The new winding can employ either non uniform-constitution or uniform-constitution, but non uniform-constitution should take account of the ratio of cross-section of coil

between star and delta components and uniform-constitution should not. The utilization coefficient of slot area is increased by definitely using single-layer, and the technical short-pitch has mean length of coil shorter than usual one. Although this new winding has been applied mainly to induction motors, it can also be applied to other three-phase AC machines such as synchronous machines.

3.6   References

[3.1] Williamson, S., and Laithwaite, E. R., (1985), "Generalized harmonic analysis for the steady-state performance of sinusoidally-excited cage induction motors", IEE Proc.-B, **132**, (3), pp. 157-163.

[3.2] Hsu (Htsui), J. S., Liou, S. P. Lin, B. T. and Weldon, W. F., (1989), "Losses influenced by third-harmonic flux in induction motors", IEEE Transactions on Energy Conversion, Vol. 6, (3), Sept. pp. 461-468.

[3.3] Chalmers, B. J. and Chandra, K. N., (1970), "High-frequency no-load losses of cage induction motors", IEEE Transactions on Power and Apparatus and System, Vol. PAS-89, No. 6, July/August, pp. 1043-1049

[3.4] Jha, C.S. and Sreenivasa, S., (1973), "Generalised rotating-field theory of wound-rotor induction machines having asymmetry in stator and/or rotor windings", Proc. IEE, **120**, (8), pp. 867-873.

[3.5] Chen, J.Y. and Chen, C.Z., (1998), "Investigation of a new AC electrical machine winding", IEE Proc. B, Electr. Power Appl., 145, (2), pp. 125-132.

[3.6] Chen, J.Y. and Chen, C.Z., (1998), "A Low Harmonic, High Spread Factor Induction Motor", IEEE International Conference on Power Electronics Drives and Energy Systems for Industrial Growth, Perth, Australia, December, pp129-134.

[3.7] Alger, P. L. and Hughes, A., (1971), "Correspondence: New 3-phase winding of low M.M.F.-harmonic content", Proc. IEE, 118, (3/4), pp. 607-608.

[3.8] Heller, B. and Hamata, V., (1977), "Harmonic effect in induction motors", (Elsevier Scientific Publishing Company, 1st edn.).

Appendix III-1

The Magnetic Field of a group of turns

The resultant magnetic field intensity of a coil with one turn referred to the circular

coordinate at the axis of the coil is a periodic function and can be expressed as [3.8]:

$$H_r(\alpha) = \frac{2i}{\pi\delta} \sum_{v=1}^{v=\infty} \frac{1}{v} \sin v \, \frac{\alpha_y}{2} \cos v\alpha \qquad (A3.1.1)$$

where H_r is the magnetic field intensity of a coil, δ the air gap, α the position of the

winding expressed in radian, v the order number of the harmonics and α_y the

periphery angle of the coil pitch in radian.

The resultant magnetic field of a group of turns consisting of N turns with equal

current i mutually displaced by a constant angle α_l is determined most conveniently

by superposition as the sum of the fields of the individual turns. According to

equation (A3.1.1), the field intensity of the individual turns is obtained:

$$H_1(\alpha) = \frac{2i}{\pi\delta} \sum_v \frac{1}{v} \sin v \, \frac{\alpha_y}{2} \cos v\alpha$$

$$H_2(\alpha) = \frac{2i}{\pi\delta} \sum_v \frac{1}{v} \sin v \, \frac{\alpha_y}{2} \cos v(\alpha - \alpha_1)$$

$$H_3(\alpha) = \frac{2i}{\pi\delta} \sum_v \frac{1}{v} \sin v \, \frac{\alpha_y}{2} \cos v(\alpha - 2\alpha_1) \qquad (A3.1.2)$$

$$\vdots$$

$$H_N(\alpha) = \frac{2i}{\pi\delta} \sum_v \frac{1}{v} \sin v \, \frac{\alpha_y}{2} \cos v[\alpha - (N-1)\alpha_1]$$

The resultant field given by the sum of the above components is:

$$H(\alpha) = \frac{2i}{\pi\delta} \sum_{v=1}^{v=\infty} \frac{1}{v} \text{sinv} \frac{\alpha_y}{2} \{\cos v\alpha [1 + \cos v\alpha_1 + ... + \cos v(N-1)\alpha_1]$$
$$+ \sin v\alpha [\sin v\alpha_1 + \sin v\alpha_2 + ... + \sin v(N-1)\alpha_1]\}$$

$$(A3.1.3)$$

Adding the series in square brackets and rewriting equation (A3.1.3), obtain

$$H(\alpha) = \frac{2Ni}{\pi\delta} \sum_{v=1}^{v=\infty} \frac{1}{v} \text{sinv} \frac{\alpha_y}{2} \frac{\text{sinv}N\frac{1}{2}\alpha_1}{N\sin v\frac{1}{2}\alpha_1} \cos v[\alpha - (N-1)\frac{1}{2}\alpha_1] \qquad (A3.1.4)$$

Moving the origin of the coordinates by the angle $(N-1)\frac{1}{2}\alpha_1$ toward the centre of the group of turns, a new coordinate system is obtained with the transformation equation:

$$\alpha' = \alpha - (N-1)\frac{1}{2}\alpha_1 \qquad (A3.1.5)$$

In the new coordinate system the magnetic field intensity of the group of turns is converted to the form:

$$H(\alpha) = N \sum_{\nu=1}^{\nu=\infty} \frac{\sin \nu N \frac{1}{2}\alpha_1}{N \sin \nu \frac{1}{2}\alpha_1} H_\nu^{'}(\alpha) \qquad\qquad (A3.1.6)$$

where

$$H_\nu^{'}(\alpha) = \frac{2I}{\pi\delta}\frac{1}{\nu}\sin\nu\frac{\alpha_Y}{2}\cos\nu\alpha^{'} \qquad\qquad (A3.1.7)$$

is the magnetic field intensity of the turns, symmetrical with respect to the axis of the group.

Appendix III-2

The Magnetic Field of a Conventional M-Phase Winding

Considering m groups of N turns each, their axes are mutually displaced along the circumference by the angle $(2/m)\pi$. In each group of N turns flows the current of one phase of a symmetric m-phase system, i.e. the currents in the individual groups of phase amplitude $I/\sqrt{2}$ and angular velocity ω are shifted in time by the same angle $(2/m)\pi$. According to equation (A3.1.6 - 7), the equation of the magnetic field intensity can be written as:

$$H_m(\alpha) = \frac{2\sqrt{2}NI}{\pi\delta}[\sin\omega t \sum_{v=1}^{v=\infty}\frac{1}{v}\sin v\frac{\alpha_y}{2}\frac{\sin Nv\frac{1}{2}\alpha_1}{N\sin v\frac{1}{2}\alpha_1}\cos v\alpha$$

$$+\sin(\omega t - \frac{1}{m}2\pi)\sum_{v=1}^{v=\infty}\frac{1}{v}\sin v\frac{\alpha_y}{2}\frac{\sin Nv\frac{1}{2}\alpha_1}{N\sin v\frac{1}{2}\alpha_1}\cos v \times (\alpha - \frac{1}{m}2\pi)$$

$$+\cdots+\sin(\omega t - \frac{m-1}{m}2\pi)\sum_{v=1}^{v=\infty}\frac{1}{v}\sin v\frac{\alpha_y}{2}\frac{\sin Nv\frac{1}{2}\alpha_1}{N\sin v\frac{1}{2}\alpha_1}\cos v(\alpha - \frac{1}{m}2\pi)]$$

(A3.2.1)

Using the product formula

$$\sin\alpha\cos\beta = \frac{1}{2}[\sin(\alpha+\beta)+\sin(\alpha-\beta)$$ (A3.2.2)

Equation (A.3.2.1) can be further developed and transformed to the form below,

$$H_m(\alpha) = \frac{\sqrt{2}NI}{\pi\delta}\sum_{v=1}^{v=\infty}\frac{1}{v}\sin v\frac{\alpha_y}{2}\frac{\sin Nv\frac{1}{2}\alpha_1}{N\sin v\frac{1}{2}\alpha_1}\{\sin[(\omega t + v\alpha) - (v+1)\frac{0}{m}2\pi]$$

$$+\sin[(\omega t - v\alpha) + (v-1)\frac{0}{m}2\pi]+\sin[(\omega t + v\alpha) - (v+1)\frac{1}{m}2\pi]$$

$$+\sin[(\omega t - v\alpha) - (v-1)\frac{1}{m}2\pi]+\cdots+$$

$$\sin[(\omega t + v\alpha) - (v+1)\frac{m-1}{m}2\pi]+\sin[(\omega t - v\alpha) - (v-1)\frac{m-1}{m}2\pi]\}$$

(A3.2.3)

The expression in braces is similar to the sum of equation (A3.1.2) for $\alpha = \omega t \pm \nu\alpha, \alpha_1 = \pm[(\nu \pm 1)2/m]\pi$ and $N = m$, so that the field intensity of the m-phase winding can be written, according to equns. (A3.1.3) and (3.2.2), as follows:

$$H_m(\alpha) = \frac{\sqrt{2}NI}{\pi\delta} \sum_{\nu=1}^{\nu=\infty} \frac{1}{\nu} \sin\nu \frac{\alpha_y}{2} \frac{\sin N\nu\frac{1}{2}\alpha_1}{N\sin\nu\frac{1}{2}\alpha_1} \{ \frac{\sin(\nu+1)\pi}{\sin[(\nu+1)/m]\pi}$$

$$\times \sin[(\omega t + \nu\alpha) - (\nu+1)\frac{2\pi}{m}] + \frac{\sin(\nu-1)\pi}{\sin[(\nu-1)/m]\pi} \times \sin[(\omega t - \nu\alpha) + (\nu-1)\frac{2\pi}{m}] \}$$

$$(A3.2.4)$$

Appendix III-3

The Magnetomotive Force of a M-Phase Winding

The distribution curve of magnetomotive force $F(\alpha)$ is defined by the relation

$$F(\alpha) = \delta H_\alpha \qquad (A3.3.1)$$

With constant air gap δ and $\mu = \infty$,

$$F(\alpha) = \delta H + \int_0^{\alpha} A(\alpha)d\alpha \qquad\qquad (A3.3.2)$$

The distribution of the magnetomotive force $F(\alpha)$ cab, therefore, be derived from the distribution of magnetic field intensity by multiplying it by the air gap length δ. According to equns. (A3.2.4) and (A3.3.1), the magnetomotive force distribution of an m-phase winding for instance is given by:

$$F_m(\alpha) = \frac{\sqrt{2}NI}{\pi} \sum_{v=1}^{v=\infty} \frac{1}{v} \sin v \frac{\alpha_y}{2} \frac{\sin Nv\frac{1}{2}\alpha_1}{N \sin v\frac{1}{2}\alpha_1} \{ \frac{\sin(v \pm 1)\pi}{\sin[(v \pm 1)/m]\pi}$$

$$\times \sin[(\omega t \pm v\alpha) \mp (v \pm 1)\frac{2\pi}{m}]\} \qquad (A3.3.3)$$

CHAPTER FOUR

PERMANENT MAGNET WIND GENERATOR DESIGN

Abstract

This chapter presents the design of a permanent magnet generator using Neodymium-Iron-Boron magnets suitable to directly coupled wind turbine applications. To accomplish the goal of small size and lightweight with an extra-low speed for direct coupling, an outer rotor structure with multiple poles is employed. Important design principles associated with the outer rotor structure are discussed along with the critical design constraints. The direct-design method is used for initial electromagnetic design. In the chapter V, the finite element method will be applied to analyze the details of the design.

In this chapter, a simple magnetic equivalent circuit approach is used for a quick and iterative design and optimization, the lumped parameters of the generator are calculated, and mathematical equations and phasor diagram are developed. Comprehensive experimental tests were conducted to verify the characteristics of the prototype generator and investigate the main machine parameters. A comparison between the theoretical values and experimental results is presented to demonstrate the effectiveness of design principles and methodologies. A good agreement has been obtained between the theoretically computed values and experimental results.

4.1 Introduction

Due to the increasing availability of high-energy permanent-magnet materials, there has been much interest and studies in wind generators with permanent-magnet excitation [4.1~4.4]. AC generators with permanent magnet rotors can offer potentiality of a high efficiency in operation and a simple and robust structure in construction because of the absence of DC field current and excitation winding. Using the recently developed high-energy permanent-magnet material, Neodymium-Iron-Boron, further enhances the reliability and effectiveness of the wind generators.

A recent study shows a great demand for small to medium rating wind generators used in stand-alone generation-battery systems in remote area [4.15]. This type of generator incorporates usually either diesel generation or solar-diesel generation to supply an isolated community. The type of generator for this application is required to be compact and light so that the generators can be conveniently installed at the top of the towers and directly coupled to the wind turbines. Compared to a conventional, gearbox coupled wind turbine generator, directly coupled generators has a series of advantages, such as a much reduced size of the overall system, a rather low installation and maintenance cost, flexible control method, quick response to the wind fluctuation and load variations, etc. However, a directly coupled generator needs to have a very low-speed operation to match the wind turbine speed and, at the same time to produces electricity in normal frequencies range (30-80 Hz). According to the electric machine design principles, this implies a very bulky generator with a very big pole number.

In research, we present a novel PM generator design to fully explore the potentials of high-energy PM machines in directly coupled wind energy applications. In particular, an innovative outer-rotor structure is adopted to cope with various difficulties in designing a directly coupled wind turbine generator. In a normally designed inner rotor PM generator for gearbox coupled applications, the number of poles is low and the magnets can be arranged on the rotor. In order to produce normal frequencies at very low speeds for direct coupling to the wind turbine, the PM generator needs a very large number of poles, resulting in a design of substantially enlarged diameter and high cost. To be economically competitive, the design of low-speed, large-diameter generators has to be optimized in terms of cost, power density, and efficiency. As will be discussed behind, the structure of outer-rotor displays uniqueness to meet such requirements.

Important design principles associated with the outer rotor structure are discussed along with the critical design constraints. The simple magnetic equivalent circuit approach is used for a quick and iterative design and optimization. the details of the design will be analyzed by finite element method in the chapter V. The targets for the generator are based on the attempting for low cost and high efficiency. Comprehensive experimental tests were conducted to verify the characteristics of the prototype generator. A comparison between the theoretical work and testing results is presented to demonstrate the effectiveness of design principles and methodologies.

4.2 Features of the Outer-Rotor Structure

The most salient feature of the newly designed PM wind generator is the outer-rotor structure as shown in Fig. 4.1.
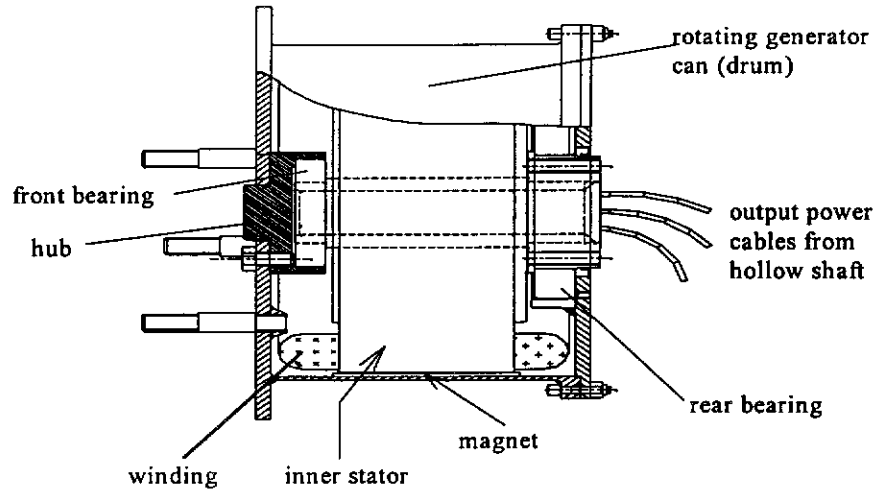
Fig. 4.1   Axial cutaway view of the generator

In this machine, the wound stator is stationary, located in the center of the machine while the magnets are mounted evenly along the inner circumference of the rotating drum supported by the front and rear bearings. In fact, this rotating steel rotor drum plays significant multi-functions such as:

i)   supporting magnetic poles;

ii)   forming part of magnetic path for the main flux;

iii)   providing a direct joint between wind turbine and the generator;

iv)   forming a protective cover to prevent the generator from environmental hazards.

Several advantages can be identified easily from the illustrated outer-rotor structure:

a) The blades of the wind turbine can be conveniently bolted to the front face of the drum to realize the direct coupling between the wind turbine and the PM generator;

b) Because of the enlarged periphery of the out-rotor drum, the multi-pole structure can be easily accommodated;

c) Due to the multi-pole structure, the total length of the magnetic path is reduced. This makes not only an effective utilization of the permanent magnets but also a noticeable height reduction of the rotor yoke, resulting in a significantly reduced total volume and weight. The coil pitch equals to the slot pitch so that the end winding is shorter and correspondingly, copper loss is lower than those in a long pole pitch machine.

Furthermore, with the ratio of the rotor diameter to the magnet width large enough, a minor air gap between the inner arc of the drum and the flat magnet surface will not be significant, resulting in a much simplified process of machining and mounting of the permanent magnets. Therefore, a small pole pitch and larger pole number are favorably accommodated by the outer-rotor structure and a cost-effective, directly coupled PM generator can be made. In the actual design, all of the radially magnetized magnets are squarely shaped and evenly placed to the inner periphery of the rotor drum. While the generator is running, the centrifugal force of the magnets applies a pressure to the bonding media. Thus, the reliability of the glued joints becomes higher. As exposed to the natural wind flow, the outer-rotor has a much-

reduced temperature rise than the stator. Additionally, the simple outer-rotor structure makes the PM generator compact, light and rugged, and easy to be installed at the top of a high tower.

4.3 Wind Energy Assessment

The power P_w available from the wind with a density ρ through a cross-area A varies with the cube of the wind speed v:

$$P_w = \frac{1}{2}\rho A v^3 \tag{4.1}$$

A wind turbine, with this swept area in the air stream, will develop a power P_t. P_t/P_w is the conversion efficiency and called the power coefficient C_p, i.e.

$$C_p = P_t/P_w = P_t/(\frac{1}{2}\rho A v^3) \tag{4.2}$$

Assuming a circular cross sectional area with a radius R, equation (4.2) becomes

$$P_t = \frac{1}{2}C_p\rho\pi R^2 v^3 \tag{4.3}$$

More detailed analysis of wind turbine performance [4.5] indicated that maximum power from the wind is obtained when the final down wind velocity is one third of the up wind velocity. The value of power coefficient is then 16/27 or 0.593.

Generally, practical wind turbines for wind generation have C_p value no more than 0.45. The power coefficient C_p is a function of blade tip speed ratio β and approximates to a parabola where C_p reaches a maximum $C_{p\text{-}max}$ at $\beta = \beta_{opt}$, and is zero at $\beta = 0$ and $2\beta_{opt}$. Fig. 4.2 shows a C_p-β curve of a typical fixed-pitch, horizontal axis wind turbine.
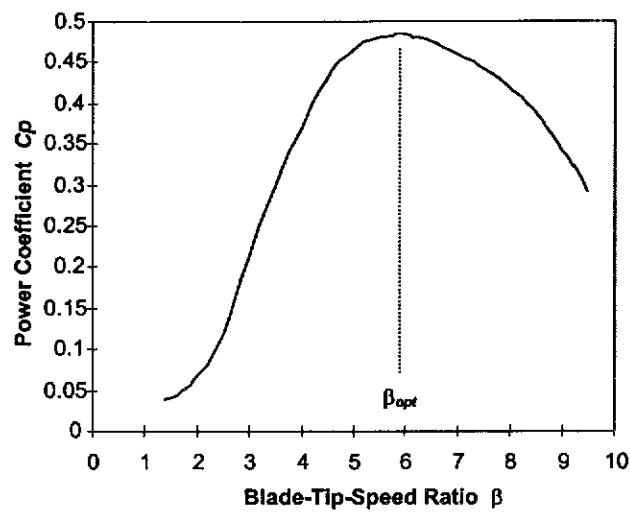
Fig. 4.2 C_p-β curve for a horizontal axis wind turbine

It can be seen that a single maximum $C_{p\text{-}max}$ occurs when the tip-speed ratio takes a particular value β_{opt}. Obviously, if the turbine is to extract maximum power from the wind, the shaft speed will vary as,

$$\omega = \beta_{opt}\, v/R \qquad\qquad (4.4)$$

When the turbine is running and keeping the tip speed ratio at β_{opt}, the output power from the turbine is,

$$P_t = (\frac{1}{2} \rho\pi \ C_{p\text{-}max} \ R^2) \ v^3 \qquad (4.5)$$

The expression in the bracket is constant, and hence the output power varies as the cube of the wind speed. Substituting equation (4.4) for v in equation (4.5), P_t can be alternatively expressed in terms of ω as,

$$P_t = (\frac{1}{2} \rho\pi \ C_{p\text{-}max} \ R^5/\beta_{opt}^3) \ \omega^3 \qquad (4.6)$$

Fig. 4.3 shows an estimated annual energy output versus mean wind speed for a horizontal axis wind turbine. It is assumed that wind speed follows a Weibull distribution [4.6].
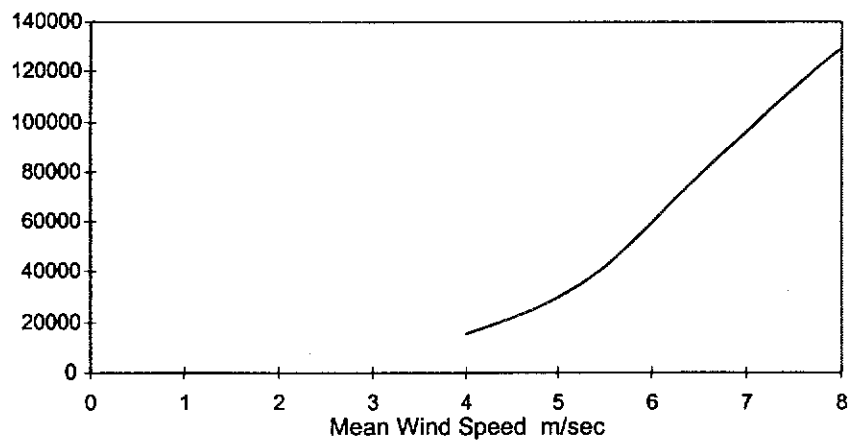
Fig. 4.3   Predicted annual energy output versus mean wind speed

The annual energy output is obtained from the Wind Energy Conversion output power curve and wind speed distribution for the site. A Weibull distribution of wind speed is often assumed for the assessment of energy output where detailed site measurements over a long period are not available. Fig. 4.4 shows a Weibull distribution with mean annual wind speed of 7.1m/s that is typical for a good site in Western Australia. Mean annual wind speed less than 4.2m/s in a site is considered uneconomic to set up a wind generator and greater than 9m/s is rarely available.
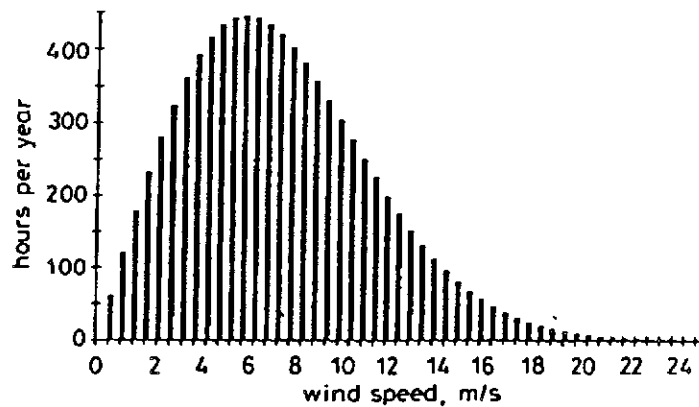
Fig. 4.4   Weibull distribution of wind speed

The nominal speed of the PM generator, which largely determines the overall size of the generator, can be determined from the wind energy assessment equation. A mean annual wind speed of 7.1 m/s is used for the design of the generator, a rotating speed of 170 rpm can be derived as the nominal speed for the wind turbine as well as the outer-rotor PM generator.   For the nominal frequency of 68 Hz, the permanent magnet has to have 48 poles.

4.4 Design Constraints

The critical factors affecting the main dimensions of the PM generator and the special design constraints due to the outer rotor structure are discussed in this section.

4.4.1 Temperature Rise

Since it is exposed to open-air conditions in remote locations, the generator is required to be completely enclosed for protection against possible damages caused by storm, sun radiation, dust, insects, chemical pollution, etc.. Therefore, there is almost no direct ventilation between inside and outside of the rotor drum and the only heat dissipation is through the outer surface of drum. Due to the multi-pole structure, the iron loss is larger than a normally designed electric machine. So, the heat generated by armature and other losses may cause a noticeable temperature rise. A maximum ambient temperature of 50°C is assumed and the glue material binding the magnets is able to withstand 120°C. Thus, a constraint of maximum temperature rise of 70°C is imposed for the full load condition. All of the thermal sources must be catered for the assumed condition.

4.4.2 Demagnetization

The magnets can be partially demagnetized by over current and/or excessive temperatures. The PM generator has to be specified to suffer no more than a tolerable demagnetization even at a possible maximum current and temperature. In addition, the magnetic design should ensure that the magnets are safe with demagnetization currents applied at all possible orientations.

4.5   Electromagnetic Design

An iterative magnetic circuit method is employed to search for a proper operating point of the magnet in no- and full- load conditions. The method involves discretization of the magnetic flux loop path that is shown by the cross-section of the generator in Fig. 4.8. The objective of the iteration is to produce an optimized magnetic structure with a low cost. The calculation is based on a smooth, non-slotted outer stator surface since the slot effect is taken accounted of by the traditional Carter coefficient approach.

The permanent magnets establish the flux in the outer-rotor machine and the flux is intended to link the coils of the phase windings on the inner-stator. All of the coils are located as close as possible to the magnets to minimize the amount of magnet flux that leaks poles of opposite polarity without linking any turns of the windings. A flux guide is formed by the laminated steel core of the stator due to its high permeability. The flux is drawn through the steel teeth radially across the narrow airgap and the yoke.

Obviously, there is a concentration of flux in the teeth. The flux crossing the air gap funnels into the teeth, which occupy approximately half of the periphery. This means that the air gap flux density will be of the order of one-half the maximum flux density in the teeth, i.e., at most, 0.8 T if it is kept below 1.6 T in the steel. The flux density in the magnets in such a machine with surface-mounted magnet will be comparable to the air gap flux density, or slightly higher. For this outer-rotor

generator, only the high-energy magnets, e.g., Cobalt-Samarium and Neodymium-Iron-Boron, are capable of operating at this high level of flux density. Machines with ferrite magnets operate with lower flux density, but at less cost.

4.5.1 Nd-Fe-B Permanent Magnet

Much of the recent progress made in the development of permanent magnet machines can be attributed to remarkable improvement of the properties of magnet materials. Following the successful development of $SmCo_5$ and then Sm_2Co_{17} in 70s, there was some concern that the cost and availability of the principal constituents might limit the commercial success of these magnets. Attention was drawn to find new magnetic materials with properties superior to existed ferrite and alnico types. Earlier investigations involved using iron in place of cobalt with a variety of rare earth elements, but all the R_2Fe_{17} compounds have very low operating temperature [4.16]. A technical term, 'Curie temperature' (T_c), is introduced here to describe fundamental characteristic of magnetic materials. The term T_c expresses the temperature above which spontaneous magnetization will not exist. The practical operating temperature for a magnet is well below T_c, and yet T_c itself is only around 125°C for Sm_2Fe_{17} and around 60°C for $Nd_2 Fe_{17}$.

An important progress was made in early 1980s. R_2Fe_{17} was modified to the ternary compound $R_2Fe_{17}B$, which has tetragonal crystal symmetry and a strong uniaxial magnetocrystalline anisotropy. The Curie temperatures for $R_2Fe_{17}B$ are some 200-300°C higher than those of the corresponding R_2Fe_{17} compounds. Then, Development quickly focussed on $Nd_2Fe_{17}B$. This new alloy is enable to offer the highest saturation magnetization, and its T_c is slightly over 300°C [4.7]. The most

compelling attribute of this compound, however, is that neodymium is considerably more abundant in the nature than samarium. It promises a significant saving in raw materials cost by coupling neodymium with the use of iron as the transition metal. $Nd_2Fe_{17}B$ is the basic compound for the modern family of permanent magnets known as neodymium-iron-boron, but various partial substitutions and modifications are commonly made to adjust the magnetic properties to suit practical applications. Nowadays, considerable research worldwide is devoted to advancing the technical capabilities and application of Nd-Fe-B.

It is known that the required magnet volume is inversely proportional to the energy product, i.e. $B_M H_M$, for a given air gap volume being magnetized to a certain flux density. Contours of constant energy product are rectangular hyperbolas, usually drawn from property data sheet provided by magnet suppliers. The maximum energy product or $(BH)_{max}$ of a given magnet occurs where the demagnetization characteristic is tangent to the BH hyperbola. If the recoil permeability is unity, this occurs for a permeance coefficient of unity, provided that there is no externally applied field from windings or other magnets. As Nd-Fe-B has a larger energy-density than most of permanent materials, it has been widely used in various types of electric machines. Fig. 4.5 shows the demagnetizing characteristic of Nd-Fe-B used in this design. It is seen that Nd-Fe-B has comparatively higher remanence B_r, coercive force H_c and maximum energy product $(BH)_{max}$. According to supplier's data, the Curie temperature is 310°C, and working temperature can be up to 120°C. All of these information are useful for detailed machine design.
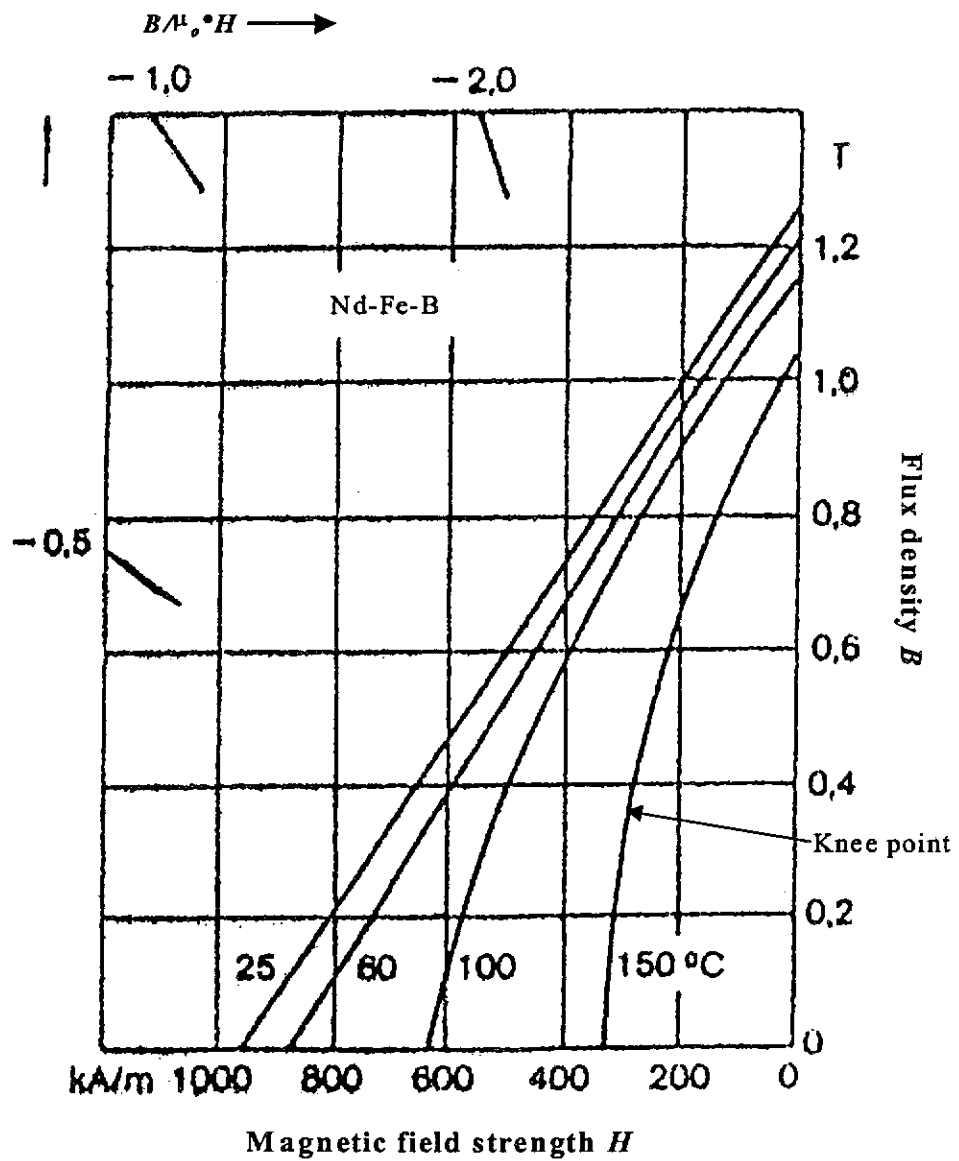
Fig. 4.5   Demagnetizing characteristic of Nd-Fe-B

4.5.2 Magnetic Circuits

In magnetic circuits, a permanent magnet can be represented either by a Thevenin equivalent circuit comprising an M.M.F. source in series with an internal reluctance or by a Norton equivalent circuit comprising a flux source in parallel with an internal permeance, as shown in Fig. 4.6 (a) and (b). Since they both represent the same

thing, equivalent circuits are exactly equivalent and can not be distinguished from each other by measurements at the terminals. Which one to use is a matter of convenience.
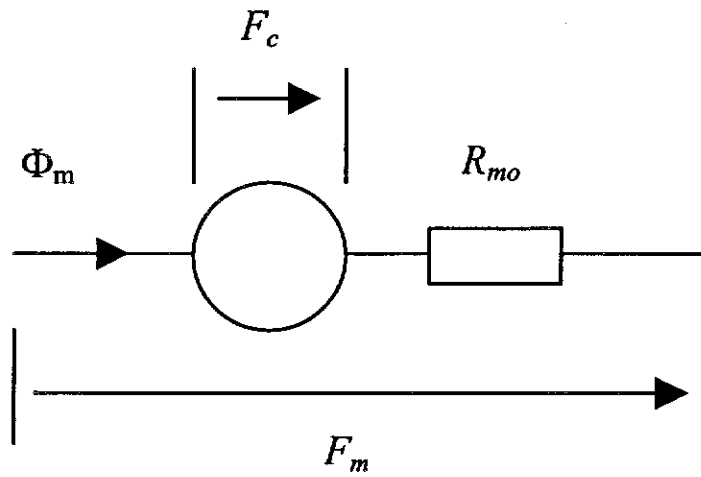
(a) Thevenin
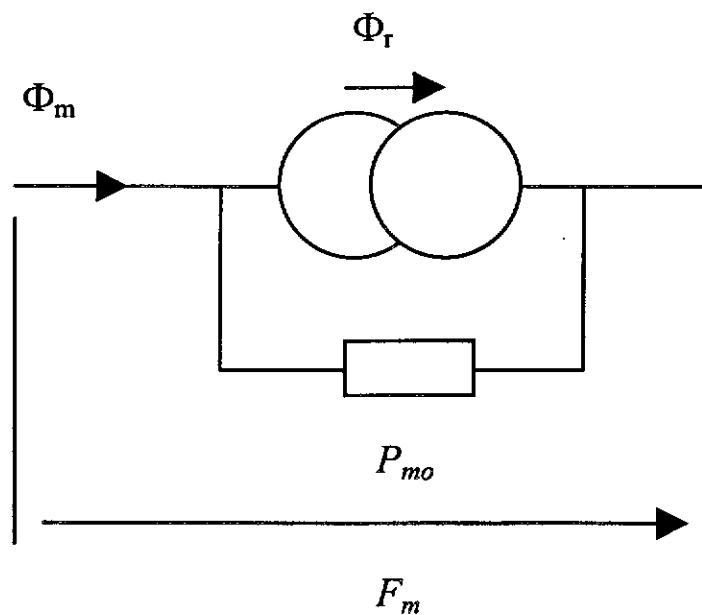
(b)   Norton

Fig. 4.6   Equivalent magnetic circuits

Analogous to the voltage/current of relationship of an electrical source at its terminals, the characteristics of a permanent magnet can be expressed graphically in terms of the flux/M.M.F. (Φ/F) relationship at the terminals or pole-faces as shown in Fig. 4.7 [4.17]. The magnet can be "short-circuited" by connecting a soft iron "keeper" across its poles. This ensures that the M.M.F. across the terminals is zero, and the magnet is operating at the Short-Circuit point in Fig. 4.7.
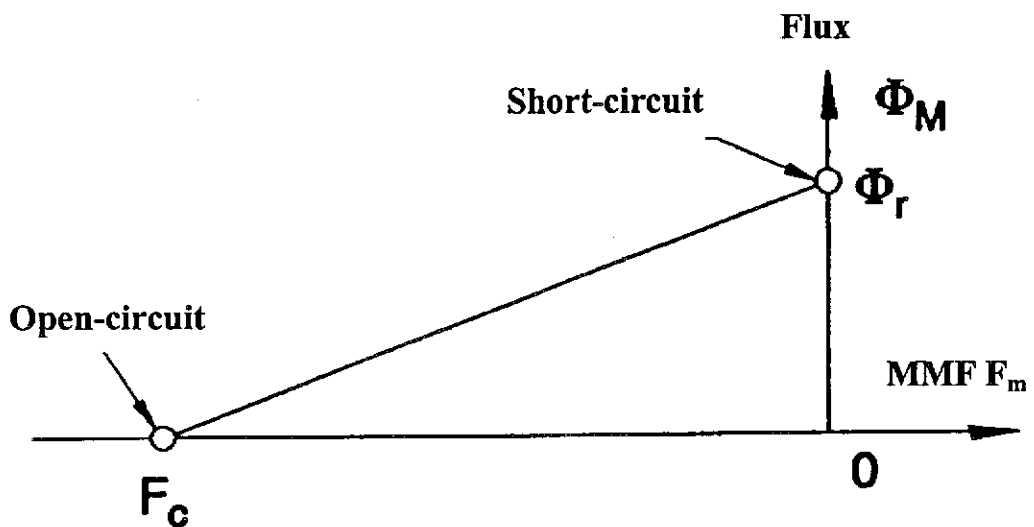
Fig. 4.7 Φ/F characteristic of a permanent magnet at given dimension

On the other hand, the "open-circuit" condition requires that the flux leaving the magnet pole is zero. In order to achieve this, an external demagnetizing MMF must be applied to suppress the flux. The internal MMF of the magnet must be exactly balanced out by the applied external MMF when the flux emerging from the pole is zero. It is only possible to do this in a magnetizing fixture with a separate DC excited coil to provide the external MMF. The terminal MMF is negative so that it can oppose the internal MMF of the magnet, F_c, and is exactly equal to it. F_c is called the

coercive MMF since it is the MMF required to coerce the magnet to produce zero flux. It directly expresses the resistance of the magnet to demagnetization.

Φ_r is called the remanent flux. This term is used to describe how much flux remains in the magnet after it has been magnetized. The amount of flux Φ_r that can be produced into an infinitely permeable keeper expresses the maximum available flux from the magnet. However, it should be careful to interpret the term because the ability of a magnet to retain flux in a magnetic circuit depends on both F_c and Φ_r at the same level. It is better to regard Φ_r as the flux retained by a keeper in the magnetic short-circuit condition. However, there is no keeper in normal operation, and the magnet operates at a flux below Φ_r. This is because the MMF drop across the air gap appears as a negative, demagnetizing MMF as seen from the magnet terminals. Besides, the phase currents produce an additional demagnetizing MMF to drive the operating point still further down the characteristic.

To describe properly the characteristics of magnets, the two parameters F_c and Φ_r are necessarily used. Also, the slope of the magnet characteristic relates F_c and Φ_r. For a given remanent flux Φ_r, it is desirable to have the flattest possible slope since this is associated with a high value of F_c and a high resistance to demagnetization. Neodymium-Iron-Boron has an Φ/F characteristic whose slope is close to the theoretical maximum and is classified as hard magnets due to its high resistance to demagnetization.

4.5.3 Open Circuit Operation

There are many important aspects of design to consider and it is not easy to define or derive an optimum design in some simple closed forms. But, it is possible to make an optimum choice of machine construction, keeping in mind the requirement to achieve sufficient output power from given dimensions, and to be able to predict performance at variable load. Because of the non-linearity, an iterative method is used for determining the operating point of the magnets. The steps involve discretization of magnetic circuit and integration of loop flux path. Repeated calculation and optimized device aim at to obtain possible large output, good performances and low cost of product.

To determine the dynamic operation point of the magnet, it is necessary to find the resultant magnetic potential differences in the discrete sections along the flux path. The leakage flux resulting from the polarization of the magnets affects the density in critical parts of the magnetic circuit and main flux. It is necessary to set up a simultaneous equation related with the balance between the MMF and the reluctance drop throughout the entire path. Applying Maxwell's integral equation in the machine construction, an equation for electromagnet calculation can be obtained,

$$\int_m Hdl - \int_s Hdl - \int_r Hdl - \int_g Hdl = \int_\Omega Jd\Omega \qquad (4.7)$$

Where, subscript m, s, r, and g express the integral paths across magnet, stator, rotor, and air gap respectively as shown in Fig. 4.8. Ω is the integral area embraced by the entire integral path and J is the current density. The first and last integrals in the equation (4.7) are referred to MMF of magnet and armature reaction. The integral

path is also shown in Fig. 4.8. In the subsequent calculation and analysis, it is assumed that put forth that a smooth stator replaces the slotted stator. Carter's coefficient is then used to modify the air gap and a larger air gap length than actual one is applied to the case.
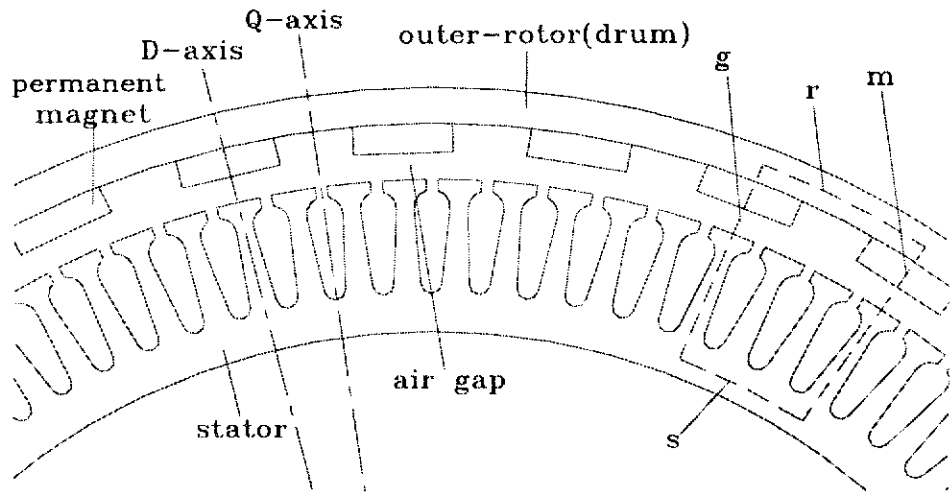
Fig. 4.8   Cross section of the PM generator

One of the important tasks is to determine the main flux paths and assign reluctances and permeances to the various branches of magnetic circuits. In Fig. 4.8, the main flux i.e. air gap flux Φ_g cross the air gap and links the coils of the stator winding. Φ_m is the magnet flux actually produced from the magnet. The leakage flux Φ_l expresses the part of the magnet flux that fails to link the stator windings. These fluxes are all defined on a per-pole basis and their units are Wb. For a calculation of lumped parameters, the ratio of air gap flux to magnet flux is defined as leakage coefficient

$$f_{lkg} = \frac{\Phi_g}{\Phi_m} = \frac{\Phi_g}{\Phi_g + \Phi_l} \tag{4.8}$$

The leakage coefficient is always less than 1, and its value depends on the configuration of the generator. The Norton magnetic equivalent circuit is shown in
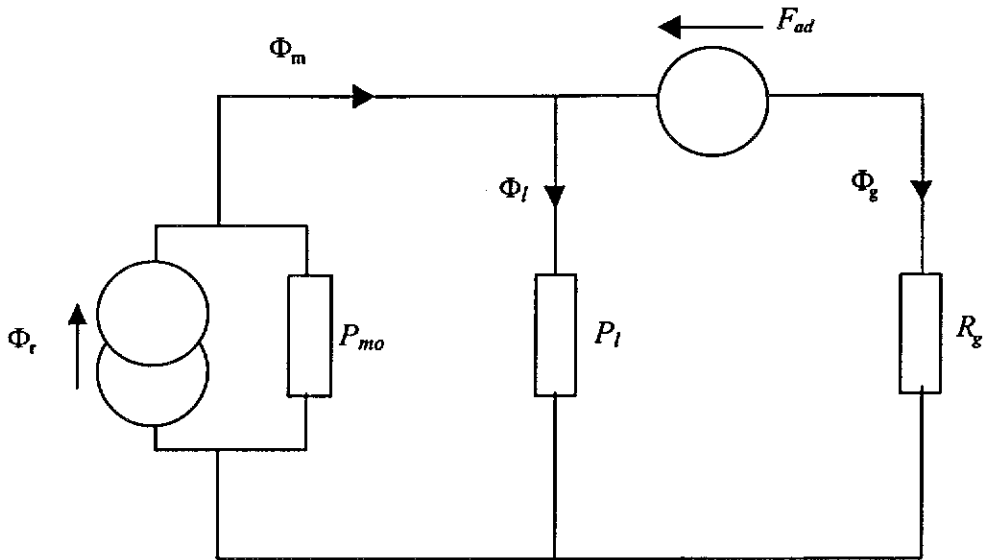
Fig. 4.9   Magnetic equivalent circuit of one pole

Fig. 4.9. where the magnet is represented by a flux source Φ_r and an internal permeance P_{mo}. The leakage permeance P_l is in parallel with the P_{mo}. The armature reaction F_{ad} is shown as an MMF in series with the air gap reluctance R_g, but F_{ad} is initially assumed to be zero at open-circuit condition. Permeances P and reluctances R are mixed freely in Fig. 4.9. This reflects that a leakage permeance diverts magnet flux away from the windings while a reluctance, mainly air gap, presents a magnet "resistance" to the flux. Provided that the steel has an infinite permeability compared with air gap, the reluctance of the steel stator and rotor may be omitted for simplicity. The magnet permeance is given by

$$P_{mo} = \mu_{rec}\,\mu_o\,A_m/L_m \qquad\qquad \text{Wb/At} \qquad\qquad (4.9)$$

113

Where A_m is the magnet pole area and L_m is the magnet length in the direction of magnetization. The magnet permeance P_{mo} is a highly idealized concept. It is derived from the radio Φ_r/F_c and thus assumes a straight demagnetization characteristic as well as uniform properties and magnetization throughout the magnet.

The air gap reluctance R_g is given by

$$R_g = \frac{g'}{\mu_o A_m} = \frac{g'}{\mu_o L_{stk} \beta_m} \qquad (4.10)$$

Where A_g is the pole area of the air gap, L_{stk} the stack length and β_m the width of magnet. The air gap g' used here is not the necessarily the physical air gap length g, but an effective value modified by the Carter's coefficient to allow for slotting. However, for the machines with surface-mounted magnets the air gap modification for slotting is mall because the magnet effectively acts as a large additional air gap, and therefore it is acceptable to use g'=g for approximate calculation [4.18].

When the PM generator is working in no-load condition, the air gap flux is solely contributed by the magnets. It is assumed that the demagnetization curve of the permanent magnets is stable with a single valued relationship between B and H. Although the Nd-Fe-B permanent magnet has its demagnetization curve in the second quadrant in B/H plane, H is treated as a positive value for convenience of calculation. For a magnet with given geometry, it is more convenient to use Φ/F curve which can be directly derived from its B/H curve shown in Fig. 4.5 by using

$$\Phi = BA_m \text{ and } F = HL_m \qquad (4.11)$$

The obtained Φ/F characteristic is shown in Fig. 4.10. The remanent flux Φ_r and the coercive MMF F_c depend not only on the material properties but also on the dimension of the magnet, and this makes matters a little more complicated than the simple magnetic equivalent circuit. The material property associated with Φ_r is the remanent flux-density B_r, and the material property associated with F_c is the coercive magnetizing force H_c. Their relationship are respectively related to

$$\Phi_r = B_r A_m \text{ and } F_c = H_c L_m \qquad (4.12)$$

The magnet's operating point generally moves reversibly up and down the straight part of the characteristic in Fig. 4.10. The slope is the recoil permeance. Note that the Φ/F demagnetizing curve is linear with intercepts. Hence,

$$\Phi = -(\Phi_r/ F_c)F + \Phi_r \qquad (4.13)$$

The ratio, Φ_r/F_c, can be interpreted as the permeance of the magnet. If paths are considered for both the main and leakage flux, a balance between the reluctance drops and the magnet MMFs guarantees that

$$\Phi_m = \Phi_\Sigma + \Phi_l$$

$$= F_m/(R_g + R_s + R_r) + F_m P_l$$

$$= F_m(P_\Sigma + P_l) \qquad (4.14)$$
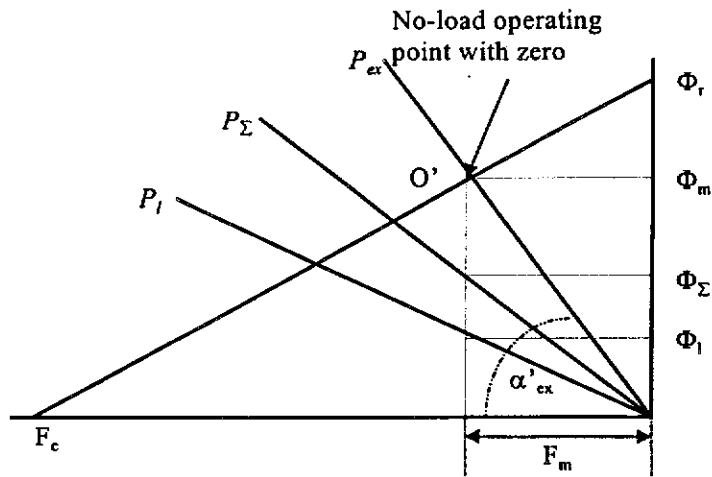
Fig. 4.10   No-load operating point of magnet

where $R_g + R_s + R_r$ is the total reluctance due to the gap, stator core and rotor yoke, and P_Σ and P_l are the permeances for the main flux and leakage flux respectively. The main flux path within a pair of poles consists of rotor yoke, two magnets, two sections of air gap, stator teeth and yoke. The total permeance P_{ex} of the entire magnetic circuit can be expressed as

$$P_{ex} = \Phi/F_m = P_\Sigma + P_l \qquad (4.15)$$

P_{ex}, the total permeance of no-load magnetic circuit, represents the external effect to the magnet. The operating point corresponding to the no-load condition is plotted as the intersection O' of the no-load line with the demagnetizing curve shown in Fig. 4.10. The coordinate Φ_m on Φ-axis represents the total flux coming out from a magnet face. The angle of the no-load line is

$$\alpha'_{ex} = \arctan P_{ex} \qquad (4.16)$$

The two lines with the slopes of main permeance P_{Σ} and leakage permeance P_l are also shown in the figure. The proper operating point can be adjusted by applying the iterative method to change the dimensions of the permanent magnets, which essentially changes the position of the PM demagnetization curve, and the geometry of the stator and rotor lamination, which essentially determines the slope of no-load line P_{ex}.

Out of the total remanent flux shown in Fig. 9, only the fraction $P_g/(P_{mo}+P_l+P_g)$ cross the air gap and link the phase winding. Thus, with $P_g=1/R_g$, air gap flux is

$$\Phi_g = \frac{f_{lkg}}{1+f_{lkg}P_{mo}R_g}\Phi_r \qquad (4.17)$$

Considering $\Phi_r=B_rA_m$ and $\Phi_g=B_gA_g$, and making use of equations (4.10-4.12), the expression in respective flux density for open-circuit can be derived. The air gap flux-density is

$$B_g = \frac{f_{lkg}\dfrac{A_m}{A_g}}{1+\mu_{rec}f_{lkg}\dfrac{A_m g'}{A_g L_m}}B_r \qquad (4.18)$$

The corresponding flux-density B_m in the magnet is given by

$$B_m = B_g \frac{A_g}{f_{lkg} A_m}$$ (4.19)

Due to f_{lkg} is less than 1, the magnet flux and flux-density are greater than they would be if there were no flux leakage at a given air gap flux.

If the vertical axis of Fig. 4.10 is scaled by $1/A_m$ and the horizontal axis by $1/L_m$, there results a relationship between the flux density B_m and magnetic field strength H_m. The practical B/H characteristic of the commercial Nd-Fe-B product is shown in Fig. 4.5 and a theoretical demagnetization characteristic is shown in Fig. 4.12 for design illustration. The slopes in the figures are called recoil permeability μ_{rec}. Although it is convenient to determine the no-load (open-circuit) operating point by using magnetic Φ/F characteristic and permeance lines, it is very direct to use the B/H curve to compute the magnetic structure without considering the effect of different geometry of magnets. The operating point of the magnet can be determined either graphically from Fig. 4.5; or by calculating H_m from the equation that describes the demagnetization characteristic:

$$B_m = \mu_{rec}\mu_o H_m + B_r \qquad B_m > B_k$$ (4.20)

The inequality $B_m > B_k$ means the need to check that the operating point is must be above the knee point. In the B/H domain, a relative parameter μ_{ex} can be defined to replace P_{ex},

$$\mu_{ex} = P_{ex} \ (L_m/A_m)$$ (4.21)

118

which is called the normalized permeability line in no-load operation. The concept of normalized permeability will be used later to compute the operation point in full load conditions.

Although Neodymium-Iron-Boron magnet has a straight demagnetization characteristic at room temperature, it may develop a knee in the second quadrant at higher temperatures. Generally, the remanent flux-density B_r decreases with temperature [4.17]. This effect is usually specified in terms of the reversible temperature coefficient of B_r, quoted in % per degree C. Let the symbol α_{Br} express the coefficient and the remanent flux-density at temperature is given by

$$B_{r(T)} = B_{r(20)}[1+\alpha_{Br}(T-20)/100] \qquad (4.22)$$

Where $B_{r(20)}$ is the value of B_r at 20°C.

The variation of coercivity with temperature is not so important as the variation of the knee point. Unfortunately, the necessary information about the knee-point values H_k and B_k as well as their variation with temperature have not been found in the given material data of the commercial product. A straight demagnetization characteristic is assumed at the beginning of the electromagnetic design, but after magnetic calculation it should be checked if the magnet flux-density B_m is greater than B_k by referring to the actual magnetization curve (Fig. 4.5) at the appropriate temperature. This procedure is safe and simple. The temperature coefficient of H_c is not used, since it does not provide the necessary information about the all-important

knee point. The performance of the generator could be degraded by the effect of elevated temperature on the demagnetization characteristic. The high temperature leads to decreasing magnet flux and therefore the torque per ampere. Also, it requires the operating current to be limited because of the upward migration of the knee-point into the second quadrant. In the design the range of variation in the torque constant which can be tolerated is quite small, of the order of a few percent. Limits are therefore set on the machine temperature and on the phase currents to keep the operation within the safe range. To achieve low cost of the generator it is not necessary to seek very high temperature properties of magnets.

4.5.4   Rotor Leakage Permeance

Two main effects are caused by rotor leakage flux. First, the magnet flux is wasted through the leakage path. In open-circuit condition the air gap flux is less than magnet flux. Accordingly, the leakage coefficient f_{lkg} is defined in equation (4.9) as the ratio Φ_g/Φ_m in order to characterize the effectiveness of the magnetic circuit in using the available magnet flux. From the magnetic circuit in Fig. 4.9, the leakage coefficient f_{lkg} is

$$f_{lkg} = \frac{1/R_g}{P_l + 1/R_g} = \frac{1}{1 + P_l R_g} \tag{4.23}$$

Another effect of rotor leakage is to provide a bypass path and divert d-axis armature-reaction flux around the magnet. The per-unit rotor leakage permeance p_{rl} can be defined as

$$P_{rl} = P_l / P_{mo} \qquad (4.24)$$

where P_l is the rotor leakage permeance per pole and P_{mo} the magnet permeance per pole. It characterizes the effectiveness of this bypass path. The relationship between leakage coefficient and per-unit rotor leakage permeance can be expressed as

$$p_{rl} = (\frac{1}{f_{lkg}} - 1)\frac{1}{P_{mo}R_g} \qquad (4.25)$$

Leakage flux in the magnetic circuit is caused by the combined MMFs of the magnets and the stator armature current. It is apparent that the calculation of no-load operating point involves the detailed calculation of the leakage permeance in different integral sections. However, a feature of leakage magnetic flux is that the leakage flux lines usually have a relatively long path in air, a linear magnetic media that gives a lot of convenience to find analytic expressions for leakage flux permeance. The leakage permeance related to those sections with various shapes and dimensions, including the paths between stator teeth, rotor poles, and between steel core and magnet, has to be considered. Since the inner-stator has a structure similar to that of a rotor in a normal machine design, stator-slot leakage permeance and others alike are skipped in the calculation.

The rotor leakage permeance P_l is calculated by simplified methods of flux-path analysis. There are three main fringing paths related to rotor as shown in Fig 4.11. For the leakage flux permeance e-f-g-h between the adjacent poles of the outer-rotor, the important dimensions are shown in Fig. 4.11(a).
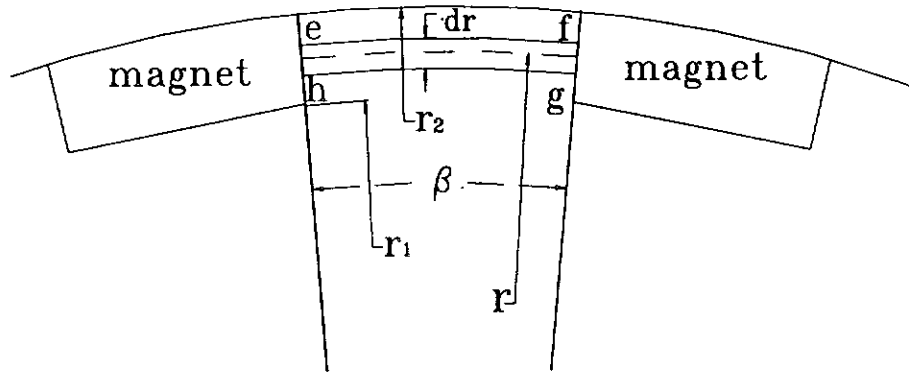
(a) Leakage flux path between two magnets through inside
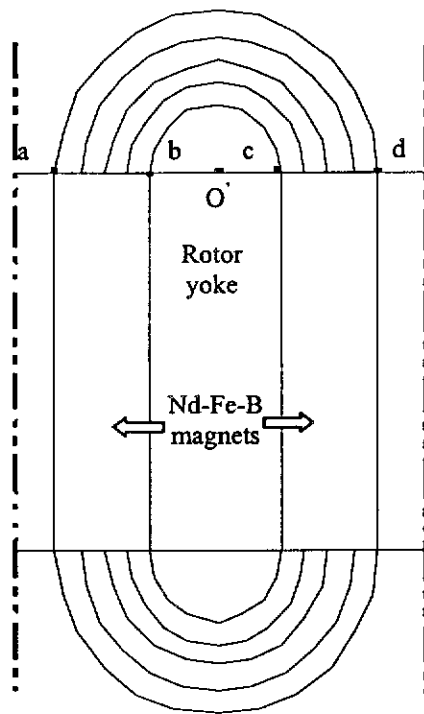
(b) Leakage flux path between two magnets through outside
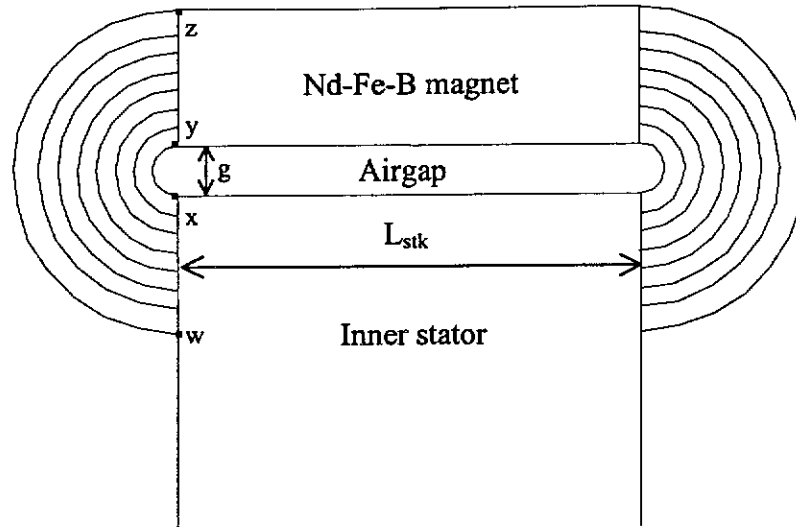
(c) Fringing flux path between magnet and stator

Fig. 4.11   Rotor Leakage flux path

Because the rotor radius is far greater than the magnet thickness, the two adjacent sides of the two opposite magnets can be approximately regarded as parts of two extended planes intersecting at the shaft center, with the angle β between them. These two equipotential surfaces e-h and f-g have the position radii r_1 and r_2, and axial length L_{stk} (into the paper). Assuming the center of the shaft is O that does not appear in the Fig.4.11 (a), the r_1 is O-h or O-g, and the r_2 is O-e or O-f. Consider the elemental strip bounded by two arcs with radii r and r+dr, between the equipotential surfaces e-h and f-g. The flux through this strip is

$$d\phi = \mu_o F L_{stk} \frac{dr}{r\beta} \tag{4.26}$$

where F is the MMF or magnetic potential drop between faces e-h and f-g. Integrating the equation (4.26) from r_1 to r_2, the total flux between the two magnets can be obtained

$$\phi = \frac{\mu_o F L_{stk}}{\beta} \int_{r_1}^{r_2} \frac{dr}{r} = \frac{\mu_o F L_{stk}}{\beta} \ln \frac{r_2}{r_1} \qquad (4.27)$$

As the permeance is defined by ϕ/F, this leakage permeance can be obtained

$$P_{m1} = \frac{\phi}{F} = \frac{\mu_o L_{stk}}{\beta} \ln \frac{r_2}{r_1} \qquad (4.28)$$

Leakage flux also occurs between magnets via space outside the active length. This leakage permeance due to end-flux between pole-pieces may be calculated by using an approximate method. It is assumed that the flux flows in semi-circular arcs across the outside air space between magnets from surface a-b to c-d, as shown in Fig. 4.11 (b). The equation (4.26) is used again with $\beta = \pi$, $r_1 = O'\text{-b}$ or $O'\text{-c}$ and $r_2 = r_1 + w_m$. Here, $O'\text{-b}$ is half of the interval between two magnets and w_m the width of the magnet. So, P_{ends} is contributed by

$$P_{ends} = \frac{2\mu_o h_m}{\pi} \ln \frac{r_2}{r_1} \qquad (4.29)$$

where h_m is the thickness of the magnet. This formula includes both ends of the magnets.

Fringing of main flux links the stator and rotor and goes through the path beyond the actual air gap area. It is assumed that the path of fringing flux forms semi-circular arcs through air space out of active length. Taking account of four sides, this corresponding permeance can be approximately calculated by the equation below

$$P_{Rf} = \mu_o \frac{(L_{stk} + k_f \frac{g}{\pi})(w_m + k_f \frac{g}{\pi})}{g} \tag{4.30}$$

where the coefficient k_f is depended on the ratio of L_{stk} or w_m to segment x-w or y-z. When the ratio is greater than 1 $k_f = 1$. Other wise $k_f = 0.307$. In this case k_f is assigned 0.307. This resulting permeance can then be added to the permeance for the section of the air gap. It is seen, from Fig. 4.11 (c), that the fringing flux in fact augments the axial length of the air gap section.

Lumped permeance calculations is usually used in initial design and occasionally refined into complex nonlinear magnetic equivalent-circuit calculation. Although the method is less accurate and less reliable than the modern finite element method, its main virtues are simplicity and easy to be programmed. Its use can be justified only where extreme speed of calculation is required and accuracy is of secondary importance, particularly for preliminary sizing calculations.

4.5.5 Full-Load Operating Point

With the full load current flowing through the armature winding, the magnetic flux of the generator is significantly altered and the operating point varies. This additional field may drive the operating point further down the demagnetization characteristic,

and depress the air gap-flux-density as well as the magnet flux-density below the open-circuit or no-load value. Once the phase current is removed, the operating point should be able to recover to the open-circuit point, and the recovery should be complete and reversible provide that the excursion of the operating point has not left the straight part of the demagnetization characteristic.

The full load magnet operating point has be to positioned in such a way that the magnetic field by the magnets is still adequate and can be completely recoverable for the worst load conditions. The corresponding position of operating point depends on both the direction and amplitude of the armature MMF. The air gap field, set up by the stator armature MMF, possesses direct-axis and quadrature-axis components, which bears a close relationship to the direct- and quadrate-axes inductance, L_d and L_q.

In the case of the PM generator, attention is paid to the demagnetizing component, the negative I_{ds}. It is known that the amplitude of MMF produced by a three-phase d-axis current under one pole is:

$$F_{ad} = \frac{3}{\pi} \frac{2\sqrt{2} W_p k_w}{p} I \qquad (4.31)$$

where W_p is the number of turns in series per phase, k_w the winding factor and p the number of poles. Thus, the field strength due to the armature MMF is:

$$H_{ad} = F_{ad} / h_m = 2.7 \frac{W_p k_w}{p h_m} I \qquad (4.32)$$

H_{ad} caused by armature reaction can be directly added to the no-load characteristic. Hence, the no-load line is shifted along the H-axis for a value of H_{ad} and intersects with the magnet demagnetizing curve at point L shown in Fig. 4.12. Note that under the full load, L is the operating point of the magnet. The corresponding coordinate B_{ad} on the B-axis is the flux density.
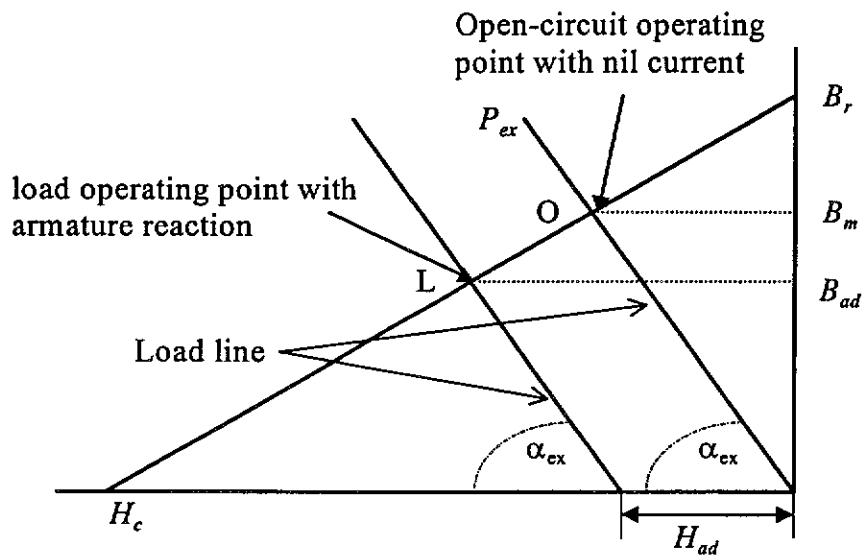
Fig. 4.12   Load operating point of magnet

To calculate the induced voltage in the load conditions, the radial flux density of the air gap can be decomposed into:

$$B_r(\ell) = \sum_{n=-\infty}^{+\infty} (a_n \cos \frac{n\pi\ell}{\tau} + b_n \sin \frac{n\pi\ell}{\tau}) \qquad (4.33)$$

where a_n, & b_n are coefficients, ℓ the average length of the arc of air gap and τ the pole pitch.

From equation (4.33), the fundamental and other harmonic flux per phase are obtained. So The fundamental and other harmonic EMFs can be found by

$$E_n = 4.44 f W_p K_{dpn} \Phi_{pn} \tag{4.34}$$

where

    f - frequency of the power source.

    W_p - number of turns in series per phase.

    K_{dpn} - fundamental or harmonic winding factor.

All the design principles and major equations discussed above are summarized and coded into a computer program to design a prototype outer-rotor PM generator and important design results are listed in Table 4.1.

Table 4.1   Principal Design Details

Outer diameter of the rotor	550 mm	Winding layers	1 Layer
Inner diameter of the rotor	537.5 mm	Magnet thickness	3.5 mm
Length of stator core	75 mm	Magnet cross section of one pair-pole	1875 mm^2
Number of poles	48	Number of phase	3
Number of slots	144	Parallel branches	1
Turns / phase	288		

4.6 Determination of X_d and X_q

A PM generator suffers from the disadvantage that because of the absence of field windings, excitation control can not be achieved. To analyze steady-state performance of PM generators, it requires knowing their main parameters. Direct-axis inductance L_d and quadrature axis inductance L_q are two of the important parameters. The positions of the direct(D) axis and quadrature(Q) axis are illustrated in Fig. 4.8. The present section aims at investigating these two parameters and predicting performance of the generator by employing a properly modified two-axis diagram as well as some basic tests. The object is, with a simple method, to achieve satisfactory accuracy by incorporating all major effects while maintaining a relative efficient calculation procedure.

4.6.1 D-Axis Reactance X_d

To calculate synchronous reactance the fundamental component of the resultant armature-reaction flux is necessarily used. This fundamental component can be derived from the actual flux by Fourier analysis, no matter what waveform of the original flux is. The actual or total fluxes in the d-axis and q-axis are also important from the designer's point view.

As $X_d \neq X_q$, permanent magnet generator with saliency has two axes of symmetry. They are pole-center axis or d-axis and interpolar axis or q-axis, which are observed from the point of view on the rotor. The effect of the armature ampere-conductor distribution and MMF in setting armature-reaction flux can be analyzed by considering the MMF to be resolved into a d-axis component $F_{1ad}\cos p\theta$ and a q-axis

component $F_{Iaq} \sin p\theta$ [4.13]. The d-axis and q-axis fluxes that they set up are not sine-distributed because the air gap permeance is not uniform. Additionally, it makes the magnetic circuit somewhat complicated that the air gap permeance in the d-axis is in series with the magnet permeance.

For the calculation of X_d, the geometry derived from the outer-rotor PM generator is shown in Fig. 4.13. Taking account of the minor air gap between magnet and rotor drum, the main air gap can be regarded as uniform.
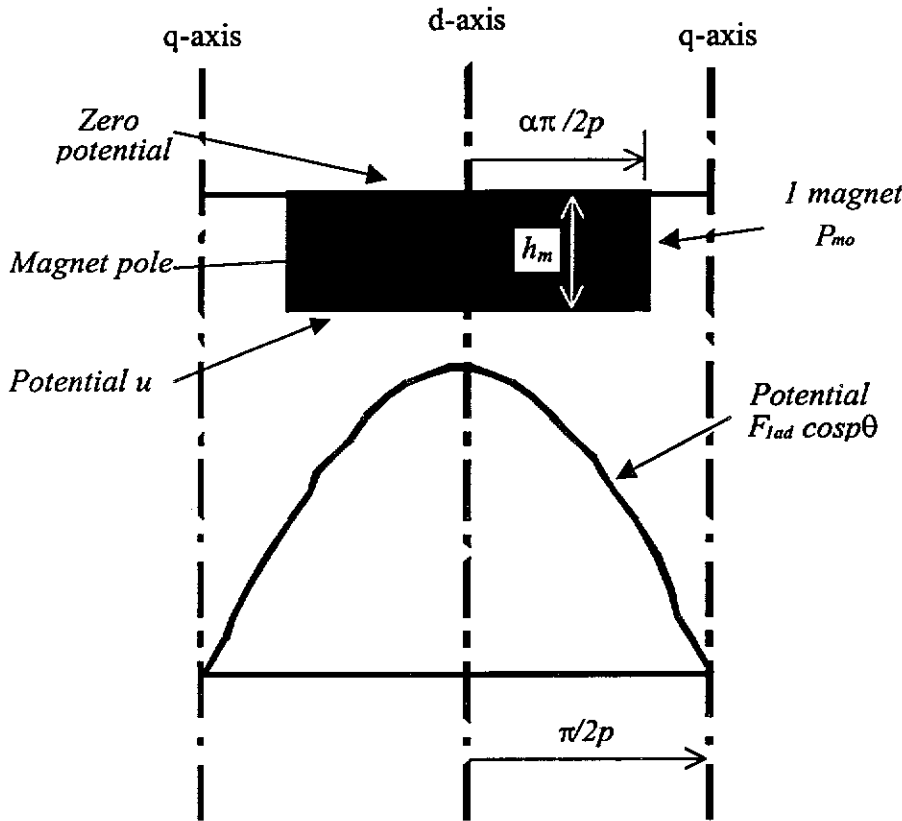
Fig. 4.13   Geometry for X_d calculation

The pole is floating magnetically and has an undetermined magnetic potential u. If the q-axis is taken as the datum of magnetic potential, u is the magnetic potential

drop across one magnet. Here, "one magnet" is defined as the segment of magnet associated with one half-pole. It means that the actual magnets are splited into two sections in parallel. The permeance P_{mo} is the permeance of "one magnet", i.e. $\mu_{rec}\mu_o(A_m/2)/h_m$, where h_m is the thickness of one block of magnet. The air gap flux-density over the magnet is given by

$$B_{ad}(\theta) = (\mu_o/g')(F_{1ad}\cos p\theta - u)$$

(4.35)

Where F_{1ad} is the fundamental component of the MMF produced by armature reaction. So, the total d-axis flux corresponding to $B_{ad}(\theta)$ is

$$\Phi_{ad} = 2 \int_0^{\alpha\pi/2p} B_{ad}(\theta) r L_{stk} d\theta$$

$$= \frac{2\mu_o r L_{stk}}{g'} [\frac{F_{1ad}}{p}\sin p\theta - u\theta]_0^{\alpha\pi/2p}$$

$$= 1/R_g [F_{1ad}k_{ad}-u]$$

(4.36)

where

$$k_{ad} = \frac{\sin\frac{\alpha\pi}{2}}{\frac{\alpha\pi}{2}}$$

(4.37)

and

$$R_g = \frac{g'}{\mu_o\frac{\alpha\pi D_g}{2p}L_{stk}} = \frac{2pg'}{\mu_o\alpha\pi D_g L_{stk}}$$

(4.38)

and $D_g = 2r$ is the average diameter of the air gap. R_g is the air gap reluctance taken over the whole arc across the magnet.

The flux Φ_{ad} is equally divided into the two halves of the magnet, and $\Phi_{ad}/2$ flows through the parallel combination $P_{mo}//P_l$ (Fig.4.9), where P_{mo} is the permeance of one magnet as shown in Fig. 4.13 and P_l is the leakage permeance associated with the magnet. Both P_{mo} and P_l are confined to one half-pole, defined by axis of symmetry d and the equipotential q. For convenience write

$$P_{mo}//P_l = P_{mo}(1 + P_{rl}) = P_m \tag{4.39}$$

Where $P_{rl} = P_{mo}//P_l$ is the per-unit rotor leakage permeance, normalized to the base P_m. Thus

$$u = \frac{\Phi_{ad}}{2P_m} \tag{4.40}$$

and when this is substituted back into equation (4.36) and re-arranged

$$\Phi_{ad} = \frac{2P_m k_{ad}}{1 + 2P_m R_g} F_{1ad} \tag{4.41}$$

The above equation gives the total flux produced by the armature reaction current I_d. The $X_d I_d$ in the phase diagram is generated by its fundamental component that can be determined by Fourier analysis of Φ_{ad} [4.8]. Thus the amplitude of the fundamental armature-reaction air gap flux-density symmetrical about the d-axis is

$$B_{lad} = \frac{4}{\pi} \int_0^{\pi/2p} B_{ad}(\theta)\, d\theta = \frac{\mu_o}{g'}[k_{lad}F_{lad} - k_1 u] \qquad (4.42)$$

The constants k_1 and k_{lad} arise in the Fourier analysis and are given by

$$k_1 = \frac{4}{\pi}\sin\frac{\alpha\pi}{2} \qquad (4.43)$$

and

$$k_{lad} = \alpha + \frac{\sin\alpha\pi}{\pi} \qquad (4.44)$$

If equation (4.40) and (4.41) are substituted into equation (4.42), there results a simple expression for B_{lad}:

$$B_{lad} = \frac{\mu_o}{g_d{}''}F_{lad} \qquad (4.45)$$

where $g_d{}''$ is the effective air gap presented to the fundamental component of d-axis flux, given by

$$g_d{}'' = \frac{g'}{k_{lad} - \dfrac{k_1 k_{lad}}{1 + P_m R_g}} \qquad (4.46)$$

The fundamental flux-linkage associated with B_{lad} is

$$\psi_{lad} = k_{wl}N_{ph}\phi_{lad} \qquad (4.47)$$

and the fundamental armature reaction flux

$$\Phi_{1ad} = \frac{D_g L_{stk}}{p} B_{1ad} \quad \text{Wb} \tag{4.48}$$

Where k_{w1} is the fundamental winding factor and N_{ph} the total number of turns in series per phase. As known, the RMS amplitude of fundamental component of the MMF is expressed as

$$F_{1ad} = \frac{3}{\pi} \frac{k_{w1} N_{ph} I}{p} \tag{4.49}$$

and

$$X_{ad} = 2\pi f L_{ad} = 2\pi f \psi_{1ad}/I \tag{4.50}$$

Manipulating equation (4.45~4.50), the d-axis synchronous reactance is obtained

$$X_d = X_{ad} + X_\sigma = \frac{6\mu_o D_g L_{stk} f}{p^2 g_d} (k_{w1} N_{ph})^2 + X_\sigma \tag{4.51}$$

The leakage reactance X_σ can be calculated by using the normal formula of electric machines design. It is

$$X_\sigma = 4\pi f \mu_o \frac{N_{ph}^2}{pq} L_{stk} \sum \lambda \tag{4.52}$$

134

Where q is the number of slots per pole per phase, and resultant ratio leakage permeance $\Sigma\lambda$ is the sum of slot ratio leakage permeance, harmonic ratio leakage permeance, tooth-top ratio leakage permeance and end-winding ratio leakage permeance.

The fundamental flux-linkage associated with B_{1ad} is $\psi_{1ad} = k_{w1}N_{ph}\Phi_{1ad}$ and the RMS induced voltage is $\omega\psi_{1ad}/2 = (2\pi/2) k_{w1}N_{ph}f\Phi_{1ad} = X_{ad}I_d$ V/phase.

4.6.2 Q-Axis Reactance X_q

The component of stator ampere-conductor distribution associated with I_q is symmetrical about the q-axis and produces a flux without passing through the magnet. An ideal form of the air gap flux distribution is shown in Fig. 4.14. The air gap flux-distribution symmetrical about the q-axis is given by

$$B_{aq}(\theta) = (\mu_o/g')F_{1aq}cosp\theta \qquad (4.53)$$

Where F_{1aq} is the fundamental component of the MMF produced by armature reaction.

135
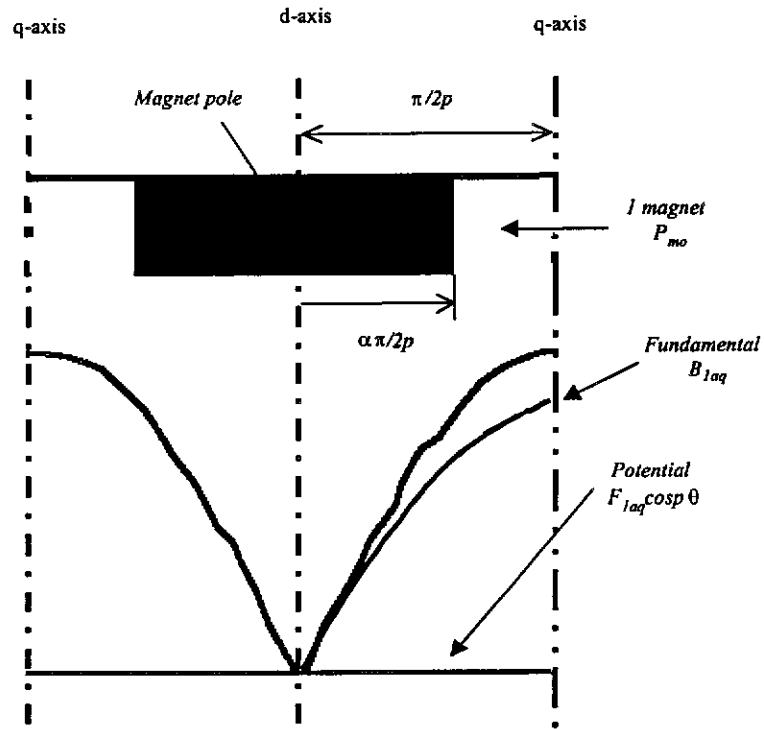
Fig. 4.14   Geometry for calculation of X_{aq}

So, the total q-axis flux corresponding to $B_{aq}(\theta)$ is

$$\Phi_{aq} = 2\int_{0}^{\alpha\pi/2p} \frac{\mu_o}{g'} F_{1aq}(\theta) rL_{stk} \sin p\theta d\theta$$

$$= \frac{2\mu_o rL_{stk}}{pg'}[1 - \cos\frac{\alpha\pi}{2}]F_{1aq} \qquad (4.54)$$

This is the total q-axis flux produced by the armature reaction current I_q. Its fundamental component generates the voltage $X_{aq}I_q$ in the phasor diagram, which is discussed in the next section. The fundamental component is determined by Fourier analysis of Φ_{aq} [4.8]. Thus the fundamental armature-reaction air gap flux-density symmetrical about the q-axis is

136

$$B_{1aq} = 4\frac{2}{2\pi} \int_0^{\alpha\pi/2} \frac{\mu_o}{g'}F_{1aq} \sin^2\theta d\theta = k_{1aq}\frac{\mu_o}{g'}F_{1aq} \qquad (4.55)$$

where

$$k_{1aq} = \alpha - \frac{\sin\alpha\pi}{\pi} \qquad (4.56)$$

Similar to the derivation of X_d the equation (4.55) can be used to determine X_q. So,

$$X_q = X_{aq} + X_\sigma = \frac{6\mu_o D_g L_{stk} f}{p^2 g_q{}''}(k_{w1}N_{ph})^2 + X_\sigma \qquad (4.57)$$

where

$$g_q{}'' = \frac{g'}{k_{1aq}} \qquad (4.58)$$

The leakage reactance is calculated using the same formula in equation (4.52) as described in last section.

For completeness, the fundamental flux of armature reaction associated with B_{1aq} is given by

$$\Phi_{1aq} = \frac{B_{1aq} D_g L_{stk}}{p} \qquad Wb \qquad (4.59)$$

The fundamental flux-linkage associated with B_{Iaq} is $\psi_{Iaq} = k_{wl}N_{ph}\Phi_{Iaq}$ and the RMS

induced voltage is $\omega\psi_{Iaq}/2 = (2\pi/2)\, k_{wl}N_{ph}f\Phi_{Iaq} = X_{aq}I_q$ V/phase.

4.7   Phasor Diagram for the PM Generator

4.7.1 Modification of the phase diagram

In a conventional salient-pole machine, the armature reaction MMF F_a can be

divided into direct-axis and quadrature-axis MMF reactions, owning to the non-

uniformity of air gap between the stator and rotor. This is the conventional dual-axis

theory. In the case, d-axis synchronous reactance X_d is greater than q-axis reactance

X_q. Fig. 4.15 shows the conventional phasor diagram [4.19].
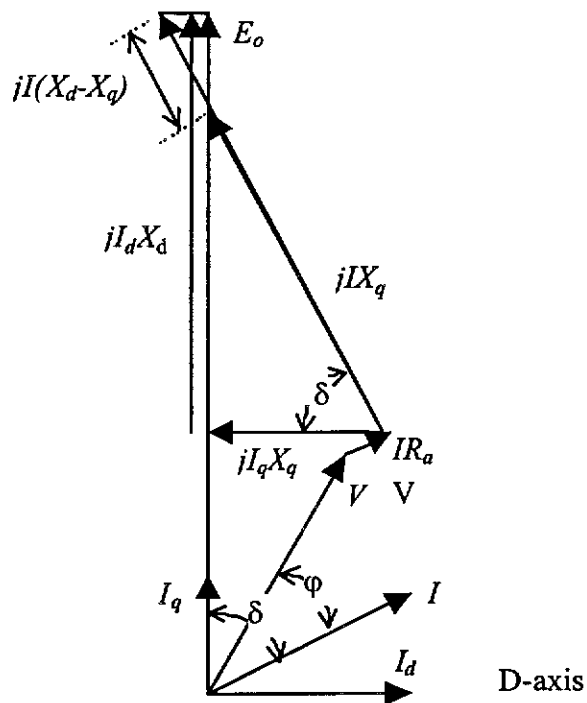
Fig. 4.15 Conventional phasor diagram for synchronous machine

It has been found that inductances L_d and L_q of a permanent magnet machine were not constant and varied with the operating condition [4.9][4.10]. In some interior-type of PM machines, L_q is even larger than L_d due to the saturation of quadrature axis [4.9]. It is necessary to make appropriate modification to the conventional two-axis theory to achieve satisfactory accuracy in the calculation of parameters. This should be considered to incorporate all major effects and maintain a relatively efficient computation program. A modified phasor diagram [4.11] is shown in fig. 4.16. It is used for subsequent analysis of performance. This is a more general phasor diagram with the current and voltages resolved into d-axis and q-axis components. The inequality of X_d and X_q stems from differences in the magnetic reluctance along the d-axis and q-axis.
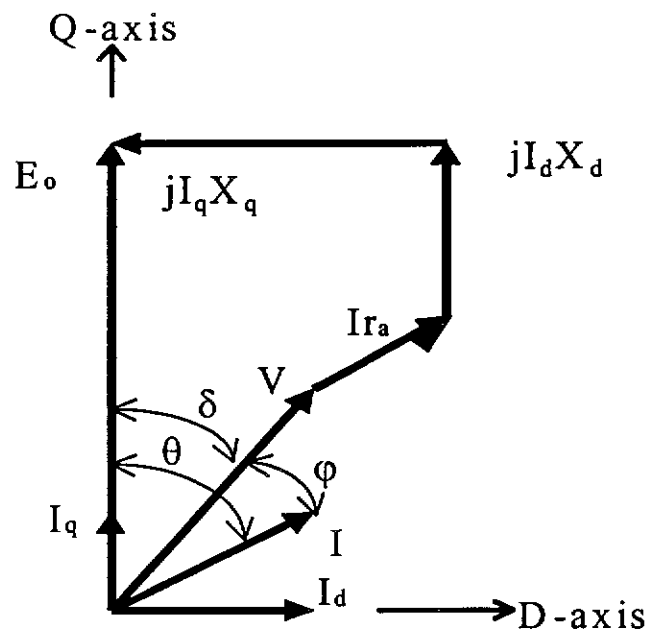
Fig. 4.16 Phasor diagram of the PM generator

With permanent magnet machine working as a generator, more attention is paid to the condition when armature current presents demagnetizing behavior. All of the vectors in the phasor diagram are based on one phase and a corresponding vector equation is given by

$$E_o = V + r_a I + j X_d I_d + j X_q I_q \qquad (4.60)$$

Where E_o is the back-EMF or open-circuit phase voltage, V the terminal voltage at load condition, r_a the armature resistance, I the load current flowing through the armature, φ the power factor angle, δ the load angle and X_d, X_q, I_d and I_q are the d-axis and q-axis reactances and currents respectively.

4.7.2 Approximate Phasor Diagram at Resistive Load

With a 3-phase symmetrical resistor connected to terminals, the generator operates at pure resistive load. To simplify analysis of the performance and parameters an approximate phasor diagram is used as shown in Fig. 4.17.

Neglecting stator resistance, the equation for voltage components with respect to d-axis and q-axis are given

$$V\cos\delta = E_o - X_d I_d \qquad (4.61)$$

$$V\sin\delta = X_q I_q \qquad (4.62)$$

In terms of load angle δ, $I_d = I\sin\delta$ and $I_q = I\cos\delta$. Load current I can be vanished by substituting $I = V/R_L$. Equations 4.61 and 4.62 are re-expressed as

$$E_o = Vcos\delta + (X_d/R_L)\ Vsin\delta \qquad\qquad (4.63)$$

$$Vsin\delta = (X_q/R_L)\ Vcos\delta \qquad\qquad (4.64)$$
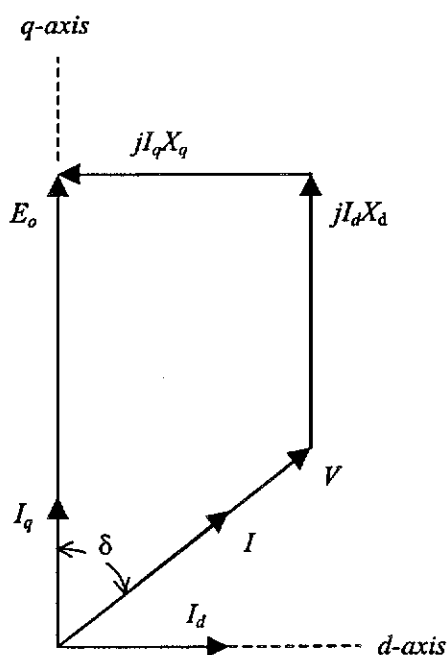
Fig. 17   Phasor diagram of PM generator at resistive load

From equation 4.64

$$\tan\delta = \frac{X_q}{R_L} \qquad\qquad (4.65)$$

$$\cos\delta = \frac{R_L}{\sqrt{X_q^{\ 2} + R_L^{\ 2}}} \qquad\qquad (4.66)$$

$$\sin\delta = \frac{X_q}{\sqrt{X_q^{\ 2} + R_L^{\ 2}}} \qquad\qquad (4.67)$$

Substituting equations 4.65, 4.66 and 4.67 into equation 4.63

$$E_o = V \frac{R_L^2 + X_d X_q}{R_L \sqrt{X_q^2 + R_L^2}}$$

(4.68)

Hence, output terminal voltage is

$$V = \frac{E_o R_L \sqrt{X_q^2 + R_L^2}}{R_L^2 + X_d X_q}$$

(4.69)

From the above equation

$$I = \frac{V}{R_L} = \frac{E_o \sqrt{X_q^2 + R_L^2}}{R_L^2 + X_d X_q}$$

(4.70)

With equations 4.69 and 4.70, output power is obtained

$$P_{out} = VI = \frac{E_o^2 R_L (X_q^2 + R_L^2)}{(R_L^2 + X_d X_q)^2}$$

(4.71)

Also, from Equation 4.65 the load angle can be found as

$$\delta = \tan^{-1}(X_q/R_L)$$

(4.72)

The PM generator should be designed to supply a strong output power. Therefore, the value of its armature DC resistance must be as small as possible. It is reasonable

to assume that X_d, X_q and R_L are far greater than the armature DC resistance. This approximate method, derived from Fig. 4.17, can achieve satisfactory accuracy when it is used to analyze design and predict the machine performance.

4.7.3 Analysis With Armature Resistance

More general case is considered for the generator operation when that the load current I lags terminal phase voltage V and the stator resistance is taken into account. Fig. 4.18 gives the phasor diagram for analysis of the generator performance.
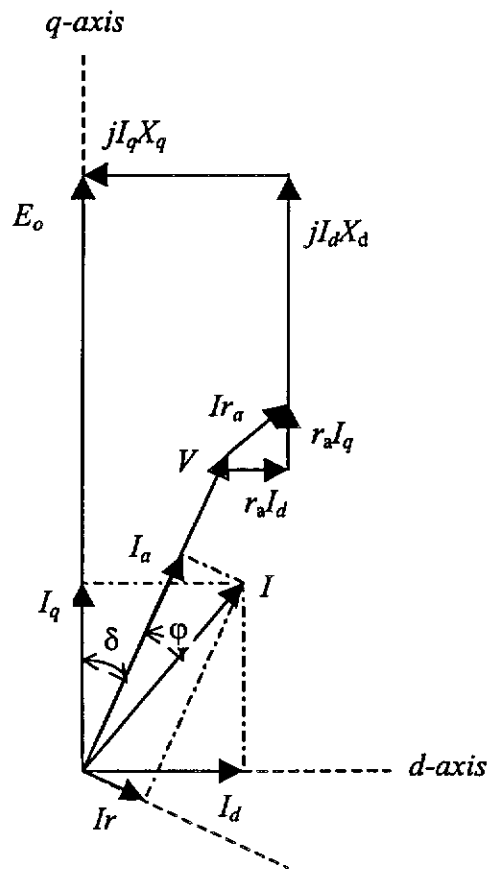
Fig. 4.18 Phasor diagram for general case

It is seen, from fig. 4.18, that the load current, with given load angle δ, can be converted into active and lagging reactive components of current. That is $I_a = I\cos\varphi$ and $I_r = I\sin\varphi$. Thus, the current components on the d-axis and q-axis are respectively expressed as

$$I_d = I_a\sin\delta + I_r\cos\delta \qquad (4.73)$$

$$I_q = I_a\cos\delta - I_r\sin\delta \qquad (4.74)$$

The voltage equations are

$$E_o = V\cos\delta + X_dI_d + r_aI_q \qquad (4.75)$$

$$0 = V\sin\delta - X_qI_q + r_aI_d \qquad (4.76)$$

Substituting for I_d and I_q into equations 4.75 and 4.76 and rearranging

$$E_o = V\cos\delta + X_d(I_a\sin\delta + I_r\cos\delta) + r_a(I_a\cos\delta - I_r\sin\delta) \qquad (4.77)$$

$$0 = V\sin\delta - X_q(I_a\cos\delta - I_r\sin\delta) + r_a(I_a\sin\delta + I_r\cos\delta) \qquad (4.78)$$

To find V and δ, equations. 4.77 and 4.78 are solved with given I and φ, by using the Newton-Raphson method of iterative computation.

4.8   Machine Characteristics and Performance

To investigate the performance of this type of generator, a prototype machine was built with a rated output power of 20 kW at a speed of 170 rpm. The machine was

designed by the author and built by Westwind Turbines Pty Ltd, a Western Australian company. Fig. 4.19 shows the outer-rotor of the machine, Fig. 4.20 the assembly of inner-stator and outer-rotor and Fig. 4.21 the assembled permanent magnet generator. Fig. 4.22 the prototype machine coupled to a car engine simulating the characteristics of a wind turbine. Westwind Turbines has subsequently built another modified outer-rotor permanent-magnet generator coupled to a 2 bladed wind turbine and installed at Murdoch University, Perth, as shown in Fig. 4.23.

4.8.1 Open-Circuit Characteristics

The nature of the no-load or magnetization curve depends upon the magnetic permeability of the iron portion of the magnetic circuit and the dimensions of the different parts of this circuit. Since it is not possible to control the field flux a voltage-speed characteristic can be used as the open-circuit characteristic. Like a separately excited generator, its main flux supplied by magnets would remain constant at no-load test. A linear relationship has been found between open-circuit voltage or back-EMF and rotating speed results.

The open-circuit test was made under various rotational speeds. Fig.4.24 shows output RMS line-line voltages drawn from computation and measurement. It is seen that the computed result from the described method has a very good agreement with measured one. The test results shows that the output terminal EMF was linearly proportional to the rotational speed and so the machine operated at unsaturated region.
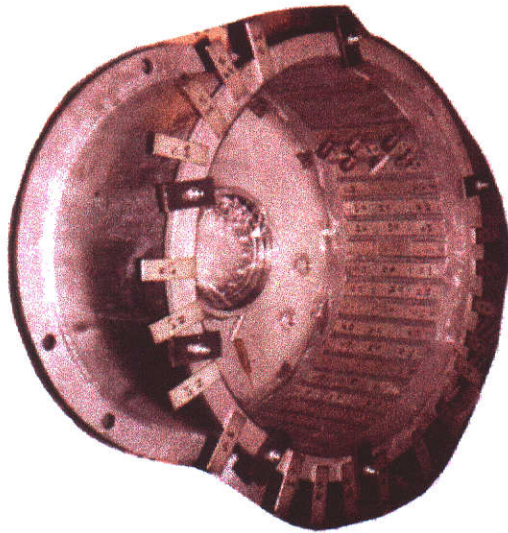
Fig. 4.19   Outer-rotor of the PM generator
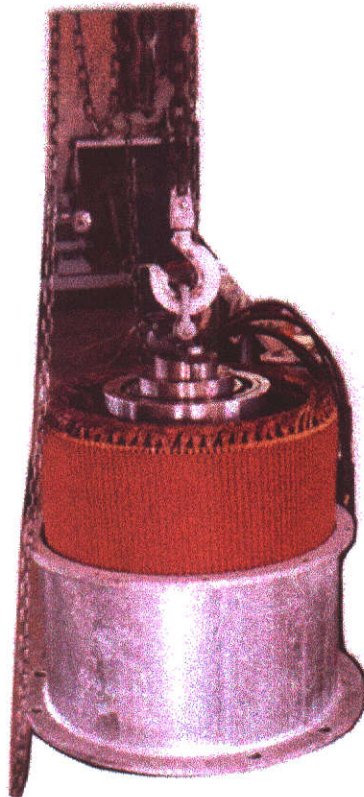
Fig. 4.20   Machine assembly
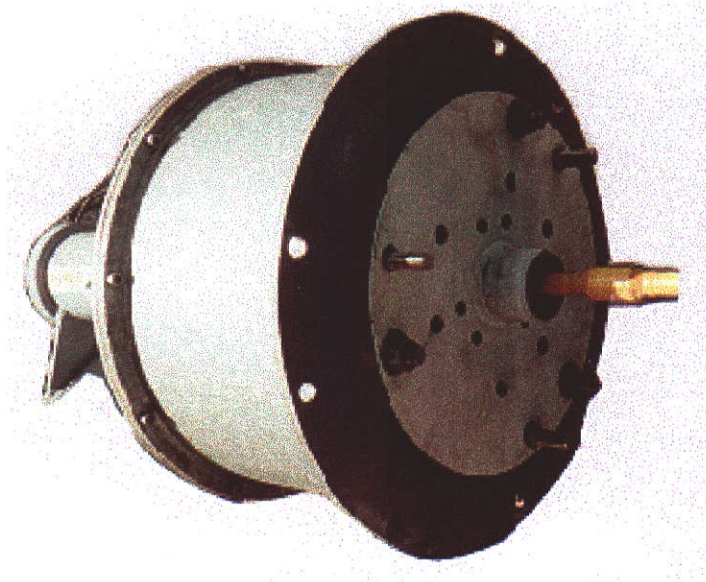
Fig. 4.21   Assembled permanent magnet generator
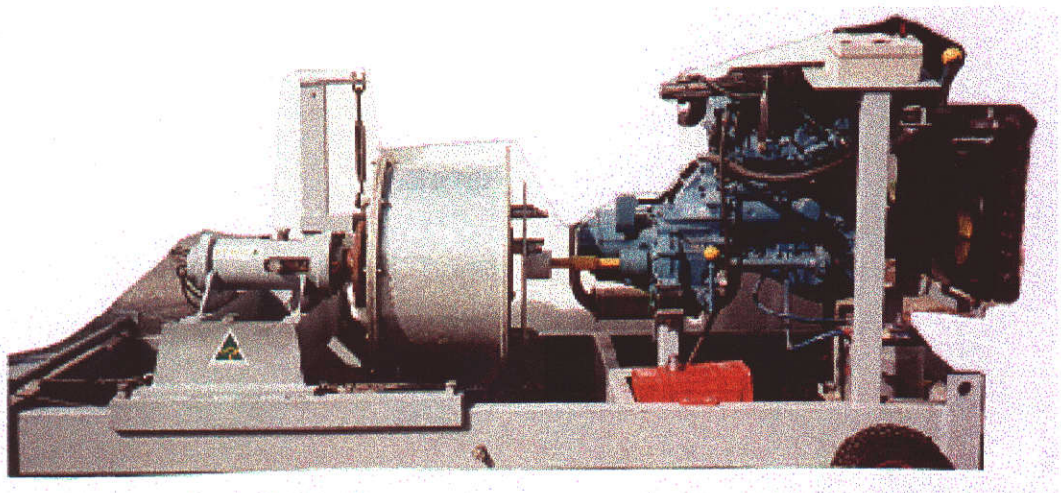
Fig. 4.22   The prototype machine on test bed

Fig. 4.23   Modified outer-rotor PM generator at test site

(Photo by courtesy of ACRE)
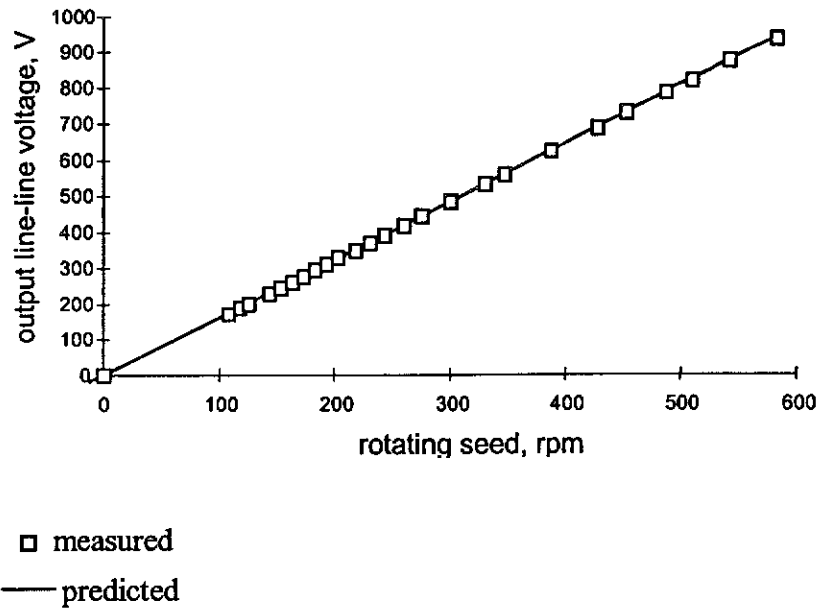
Fig. 4.24   Open-circuit characteristics of the PM generator

4.8.2 Measurement of Synchronous Inductance

Direct axis synchronous reactance X_d is defined as the ratio of the fundamental component of reactive armature voltage due to the fundamental direct axis component of armature current to this component of current under state conditions. It is known that positive sequence currents in a balanced three-phase stator winding, set up a rotating field, consisting of fundamental component and a number of space harmonics. Some of the harmonics rotate with respect to armature in the same direction as fundamental while others opposite to it. The fundamental that rotates at synchronous speed remains stationary with respect to the rotor, if the later is running at synchronous speed. If the rotor position is so adjusted that the direct- or pole-axis coincides with the maximum of the fundamental of the rotating MMF wave, the magnitude of the corresponding flux would be the largest, because the reluctance of

the path in this particular position is minimum. The flux linkage of any armature phase per unit current in that phase is the direct axis synchronous inductance.

Attention should be paid to two points. Firstly, since the harmonics of the MMF wave have been ignored, MMF wave would be purely sinusoidal, and as it is in coincidence with d-axis, no MMF exists in the quadrature axis. Therefore, no quadrature axis current will flow under these conditions. Secondly, as the MMF wave is stationary when referred to the field system, there would be no EMF induced in the rotor.

Quadrature axis synchronous reactance X_q is defined as the ratio of the fundamental component of reactive armature voltage due to the fundamental quadrature axis component of armature current to this component of current under state conditions. If the quadrature-axis is aligned with the crest of the space fundamental of the MMF wave due to positive sequence armature current, the flux would be minimum. The corresponding flux linkage per unit armature current is the q-axis synchronous inductance.

4.8.2.1 D-axis inductance L_d

To find out X_d of a permanent magnet motor, it was suggested [4.12] to use the open-circuit voltage E_o measured at zero-current, input voltage V and no-load current I_{nl} for calculation in the following:

$$X_d = (V - E_o) / I_{nl} \qquad (4.79)$$

The measurement of X_d by this way is a good approximation at a no-load current level. The similar method is employed to plot the direct-axis inductance of this outer-rotor generator. To find the current I_z at zero power factor a zero power factor test was carried out with a 3-phase variac used as the symmetrical inductive load. The output terminal voltages and inductive load currents were measured, and a power factor angle meter was used to monitor the variation of the power factor angle.

It is known that when the power factor angle φ approaches $\pi/2$, E_o would tend towards the sum of V_{ph} and $X_d I_d$, and the load current I_z is nearly in d-axis. At the condition, the voltage equation is:

$$E_o = V_{ph} + X_d I_z \tag{4.80}$$

Thus,

$$X_d = (E_o - V_{ph}) / I_z \tag{4.81}$$

To obtain the load current I_z at zero power factor, an inductive load should be applied to the output terminals of the machine. In the test, the symmetrical inductive load (a 3-phase variac) was adjusted until the power factor angle reached nearly $\pi/2$. As the reactance is far greater than the DC resistance of the variac, the load current can be basically regarded as inductive. The output terminal voltage and inductive load current were measured. The power factor angle meter was used to monitor the variation of the power factor angle.

In the test, the machine was run at 50 Hz and the load current was gradually increased from low to high values while the terminal phase voltage V_{ph} and load

current I_z were recorded to get enough data points. It was found that the power factor angle between output phase voltage and load current was not $\pi/2$ until the load current closed to 9.3 ampere, even though a nearly pure inductive load was connected to the output terminals of the machine. During the test the generator displayed a tendency trying to keep the phase voltage and phase current in phase. This characteristic is shown in Fig. 4.25.
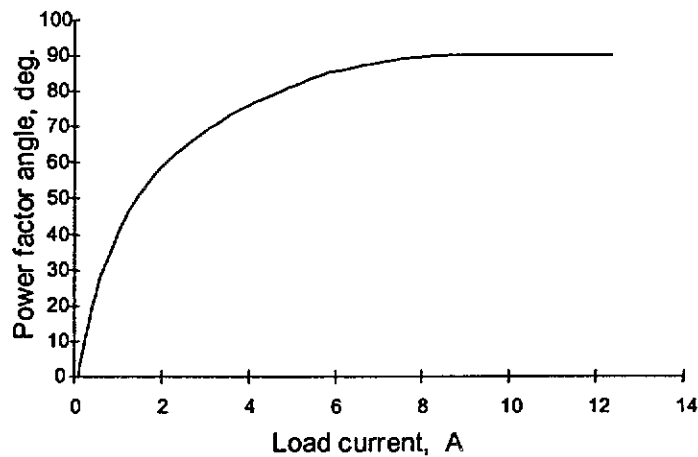
Fig. 4.25 Variation of power factor angle in inductive load test

From the test results, the direct-axis inductance L_d can be found:

$$L_d = (E_o - V_{ph})/(2\pi f I_z)$$ (4.82)

The measured direct-axis inductance varying with load current through this test is shown in Fig. 4.26. In the test L_d increased by a factor of about 15% while the current varied from 9.3 A to 56 A. The variation of L_d tended to compensate the voltage drop between E_o and V_{ph} when the load current rose.

4.8.2.2   Q-axis inductance L_q

Honsinger suggested [4.13] that measurement of the three parameters E_o, X_{do} and X_{qo} should, if possible, be under actual operating conditions with the machine loaded. To obtain the inherent parameters of the machine, a resistive load was used in the test to plot the variation of L_q since the load of resistor has least impact on output variables. Also, to ensure the later calculation as precise as possible, a power factor meter was set to detect any variation of angle. In the test, a series of relative variables were recorded based on the load current changing.

—X— Computed L_q with constant L_d

—O— Measured L_q

—+— Measured L_d by zero power factor test
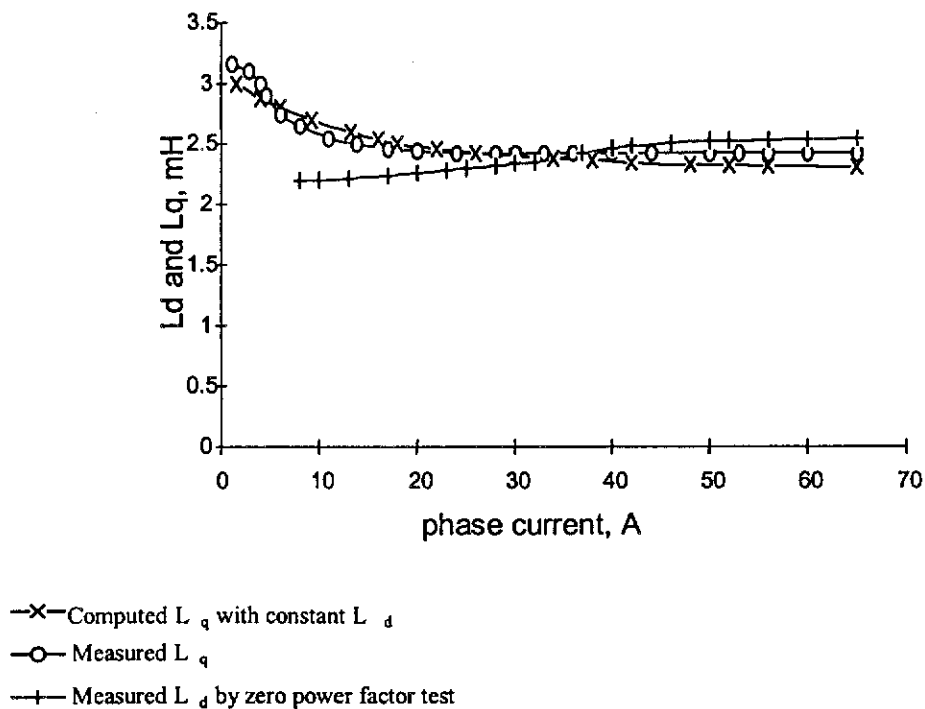
Fig. 4.26 Variation of L_d and L_q

With the E_o, L_d, φ, V_{ph}, and I obtained in the tests, and using the phasor diagram shown in Fig. 4.18, a series of tested points of L_q, varying with load current, were determined. The variation of L_q versus load current I is shown in Fig. 4.26.

Additionally, a curve of L_q computed with a constant L_d is drawn in Fig. 4.26. It is seen, at constant frequency, that L_q had a higher value than L_d at low current. While load current increased the armature D-axis reaction became stronger, L_q reduced to a level close with L_d. Further increase of load current, say greater than 37 A, led to a lower L_q. In contrast, L_d had a reverse characteristic in the test. It shows that the load current I has a significant affect to the value of L_q. From the two parameters L_d and L_q, this outer-rotor PM generator is similar to a normal non-salient machine.

4.8.3 Load Test Results

The prototype generator was tested with a symmetrical 3-phase resistive load. In the test, the armature reaction varied with different load condition had significant influence to the output characteristics of the machine. The designed parameters, mentioned methods and a proper phasor diagram have been used to predict the output characteristics at resistive load condition. The predicted results of the output phase voltage with load current variation at six different speeds are shown in Fig. 4.27. Comparing with the X_d and X_q at low operating frequency, stator armature resistance r_a has a significant influence to the performances of the permanent magnet machine. It is seen in Fig. 4.27 that the prediction of regulation at low rotation section reaches a reasonable accuracy by taking account of r_a. Fig. 4.27 also shows the measured results of output voltage per phase at six different rotating speeds with resistive load. The measured output phase voltage is the mean of the three-measured phase voltages and the load current is the mean of the three measured line currents. A positive voltage regulation can be seen in the results. The computed results include stator resistance r_a and armature reaction with saturation of L_q. A good agreement between computed and measured values was obtained within the normal load current range.

With higher value of current, difference between the two voltages is gradually increased.
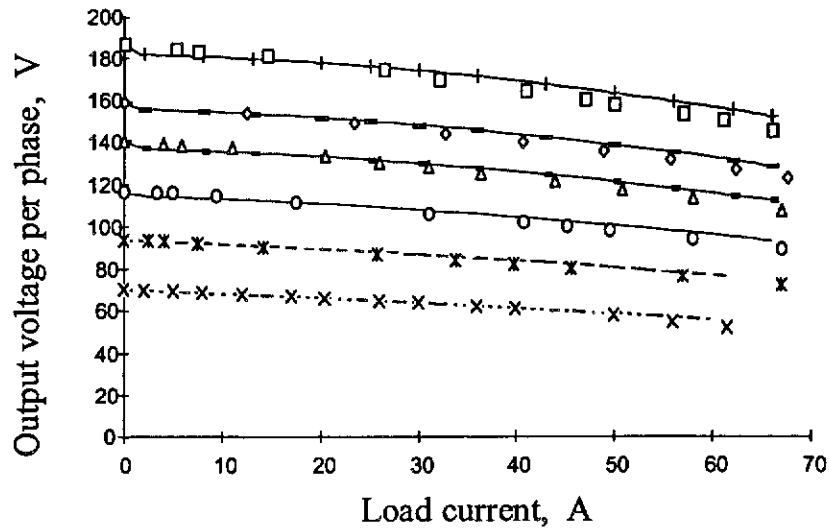
Fig. 4.27   Comparison of regulation

The difference between computation and measurement could be caused by the variation of stator armature resistance due to temperature rise. A constant resistance value for r_a was used in the computation, which remained with temperature. However, operation at higher current levels resulted in temperature rise and caused the r_a to change a lot in the actual test. When frequency increased, load angle and

power factor angle varied in a more complicated function, which is related to the features of magnet material and symmetry of the machine.
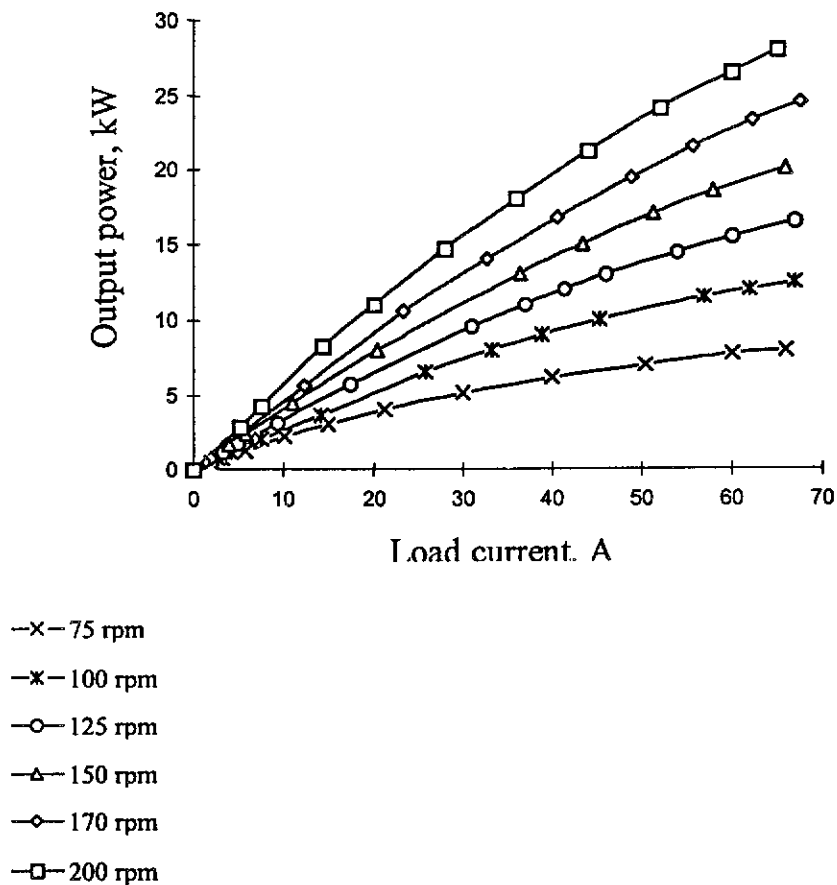
Fig. 4.28   Output characteristic at different speeds

The synchronous performance of this prototype machine was also tested under different loading condition at six different rotational speeds. The output power with varied load current at each of these speeds is shown in Fig. 4.28. It is obvious that the generator characteristics are affected by the variation of load power factor due to the changing position of armature reaction field with respect to the rotor. Since the outer-rotor field is uncontrollable except by some complicated means, the effect of the power factor requires consideration in this type of machine. A proper mean to

improve the machine characteristic is to use capacitors in circuit, either in series or in parallel with the load.
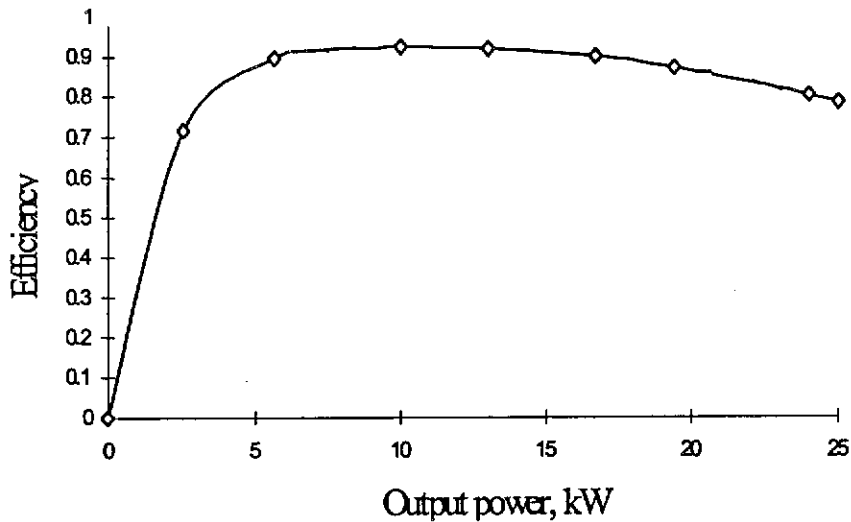
Fig. 4.29   Machine performance at 170 rpm

The experimental results of load test show that when the output power of the generator reached 20 kW at the rotating speed of 170 rpm, the efficiency was about 87% and the output phase voltage was 134 V. The efficiency characteristic versus output power is shown in Fig. 4.29. After one hour's full load test, the measured temperature rise of the stator armature was 57°C at the ambient temperature of 31°C. This exhibits that the machine can work with a reliable performance at the supposed environmental condition such as the restraint in section 4.4.

4.9 Conclusion

This chapter has described the design of the outer-rotor, low-speed permanent magnet generator used for direct coupled wind turbine application. Design principles

and important equations for the outer-rotor, multi-pole permanent magnet generator have been fully developed and utilized for the design and construction of a prototype using high energy Neodymium-Iron-Boron magnet. Obviously, the simple mechanical structure and reduced weight of the generator are the features that can bring benefits to machine manufacture, transportation, installation and site maintenance.

As the machine is used for wind energy conversion, some initial data has been derived from the wind energy assessment, such as the nominal rotating speed and the rated-power requirement. The electromagnetic design is the most important task and involves the detailed calculation of various parameters. Since the generator is excited by permanent magnet and has a novel outer-rotor structure, some conventional formulae for normal synchronous machines could not be applied. The Thevenin and Norton equivalent circuits were applied in the magnetic design. The values of main flux permeances and leakage flux permeances depend mainly on the geometry of the machine and properties of the Nd-Fe-B material. A modified phasor diagram was used in the electromagnetic design. The estimation of d-axis and q-axis inductances, and prediction of output characteristics are based on this phasor diagram.

A prototype machine was built to demonstrate the main features of the proposed generator and to validate the theoretical magnetic model. It was verified that the permanent magnet generator can operate with good and reliable performance over a wide range of speeds. Satisfactory results have been achieved by using the direct design program for initial iteration. It is seen, from the experimental results, that the outer-rotor permanent magnet generator has a behavior similar to a normal non-

salient machine. A detailed analysis with finite element method will be described in chapter five. The good agreement between the theoretical and experimental results displays the availability of the design principles and the effectiveness of the design methodology.

4.10 References

[4.1] Spooner, E. and Williamson, A.C., (1996), "Direct coupled, permanent magnet generators for wind turbine application", IEE Proc.-Electr. Power Appl, Vol. 143, (1), pp.1-8.

[4.2] Soderlund, L., Eriksson, J-T., Salonen, J., Vihriala, H. and Perala, R., (1996), "A permanent magnet generator for wind power application", IEEE Transactions for Magnetics, Vol. 32, No.4, pp.2389-2392.

[4.3] Nayar, C.V., (1991), "Investigation of capacitor-excited induction generators permanent magnet alternators for small scale wind power generation", Renewable energy, Vol. 1, No.3/4, pp.381-388.

[4.4] Lampola, P., Perho, J. and Saari, J., (1995), "Electromagnetic and thermal design of a low-speed permanent-magnet wind generator", Proc. IEEE Powertech conference, Stockholm, pp.221-215.

[4.5] Golding, E.W., (1976), "The Generation of Electricity from Wind Power", E&F Spon Ltd., London.

[4.6] Johnson, G.L., (1985), '*Wind Energy Systems*', Prentice-Hall, U.S.A.

[4.7] Strnat, K. J., (1987), "Permanent magnets based on 4f-3d compounds", IEEE Transactions on Magnetics, Vol. 23, pp.2094-2099.

[4.8] Miyashita, K., Yamashita, S., Tanabe, S., Shimozu, T. and Sento, H., (1979), "Development of a high-speed permanent magnet synchronous motor", IEEE transactions, Power Apparatus and Systems.

[4.9] Chalmers, B.J., (1994), "Performance of interior-type permanent-magnet alternator", IEE Proc.-Electr. Power Appl, Vol. 141, (4), pp. 186-190.

[4.10] Shimmin, D.W., Wang, J., Bennett, N. and Binns, K.J., (1995), "Modeling and stability analysis of a permanent-magnet synchronous machine taking into account the effect of cage bars", IEE Proc.-Electr. Power Appl, Vol.142, (2), pp. 137-144.

[4.11] Chen, J.Y. and Nayar, C.V., (1998), "Determination of Parameters and Evaluation of Performance of An Outer-Roter Permanent Magnet Generator for Wind Energy Application", IEEE International Conference on Power Electronics Drives and Energy Systems for Industrial Growth, Perth, Australia, December, pp353-358.

[4.12] Hongsinger, V.B., (1982), "The fields and parameters of interior type a.c. permanent magnet machines", IEEE Trans., PAS-101, (4), pp.867-876.

[4.13] Hongsinger, V.B., (1971), "The inductances L_d and L_q of reluctance machines", IEEE Trans. on Power Apparatus and Systems, PAS-90, (1), pp.298-304.

[4.14] Chen, J.Y., Nayar, C.V. and Xu, L., (1998), "Design of A Outer-Rotor, Direct-Coupled Wind Generator for Wind Energy Conversion", 1998 IEEE Industry Applications Society Conference (The 33rd Annual Meeting), St. Louis, USA, October 11-15, pp387-394.

[4.15] Nayar, C.V., Phillips, S.J., James, W.L., Prior, T.L. and Remmer, D., (1993), "Novel wind/diesel/battery hybrid energy system", Solar Energy 51(1), pp65-78.

[4.16] Strnat, K. J., (1970), "The recent development of permanent magnet materials containing rare earth metals", IEEE Transactions on Magnetics, Vol. 6, pp.182-190.

[4.17] Campbell, P., (1994), "Permanent magnet materials and their application", Cambridge University Press, London.

[4.18] Sawhney, A.K., (1992), "A course in electrical machine design", Dhanpat Rai & Sons, Deihi.

{4.19] Edwards, J. D., (1986), "Electrical machines : an introduction to principles and characteristics", Macmillan, London.

Armature Reaction under One Pole Caused by a 3-Phase Winding Current

It is known that the amplitude of magneto-motive force under one pole produced by a single-phase winding current is [3.8].

$$F_1 = \frac{4\sqrt{2}}{\pi} \frac{IW_p}{p} k_w \qquad (A4.1.1)$$

where I is the phase current, W_p the number of turns in series per phase, k_w the winding factor and p the number of poles.

A symmetrical 3-phase winding has a space displacement of $120°$ between each phase winding. When a balanced 3-phase current flows through the 3-phase winding, there is a phase shift of $120°$ electrical between each other. Let the center of winding A be at the origin with initial position angle of φ, and the value of current in winding A be zero when time $t = 0$. Then, the magneto-motive force (MMF) produced by A, B and C 3-phase windings are respectively

$$f_{A1}(\varphi,t) = F_1 \cos\varphi \sin\omega t$$

$$f_{B1}(\varphi,t) = F_1 \cos(\varphi - \frac{2}{3}\pi)\sin(\omega t - \frac{2}{3}\pi) \qquad (A4.1.2)$$

$$f_{C1}(\varphi,t) = F_1 \cos(\varphi - \frac{4}{3}\pi)\sin(\omega t - \frac{4}{3}\pi)$$

With the help of trigonometrical formula

$$sin\alpha \cos\beta = \frac{1}{2}\sin(\alpha + \beta) + \frac{1}{2}\sin(\alpha - \beta)$$ (A4.1.3)

The equation (A4.1.2) can be re-written as

$$f_{A1} = \frac{1}{2}F_1 \sin(\omega t - \varphi) + \frac{1}{2}F_1 \sin(\omega t + \varphi)$$

$$f_{B1} = \frac{1}{2}F_1 \sin(\omega t - \varphi) + \frac{1}{2}F_1 \sin(\omega t + \varphi - \frac{4}{3}\pi)$$ (A4.1.4)

$$f_{C1} = \frac{1}{2}F_1 \sin(\omega t - \varphi) + \frac{1}{2}F_1 \sin(\omega t + \varphi - \frac{2}{3}\pi)$$

Now, Add the three M.M.F.s in equation (A4.1.4) together. Since the sum of the

second items at the right hand of each equation in equation (A4.1.4) is zero, the

resultant MMF is obtained

$$f_1(\varphi, t)$$
$$= f_{A1} + f_{B1} + f_{C1}$$
$$= \frac{3}{2}F_1 \sin(\omega t - \varphi)$$ (A4.1.5)
$$= F_a \sin(\omega t - \varphi)$$

Where, the amplitude of MMF produced by 3-phase current in 3-phase windings is

$$F_a = \frac{3}{2}F_1 = \frac{3}{\pi}\frac{2\sqrt{2}IW_p}{p}k_w$$ (A4.1.6)

To find direct-axis component of F_a, take angle θ into account

$$F_{ad} = F_a \sin\theta$$

$$= \frac{6\sqrt{2}}{\pi} \frac{IW_p}{p} k_w \sin\theta \qquad\qquad (A4.1.7)$$

where θ is the phase displacement between load current and direct axis. To obtain the quadrature axis component of armature reaction

$$F_{ad} = F_a \cos\theta$$

$$= \frac{6\sqrt{2}}{\pi} \frac{IW_p}{p} k_w \cos\theta \qquad\qquad (A4.1.8)$$

In the above derivation, the fundamental is only considered.

CHAPTER FIVE

FINITE ELEMENT ANALYSIS FOR THE DESIGN OF

THE PERMANENT-MAGNET GENERATOR

Abstract

The numerical technique has been recognized as practical and accurate method of field computation to aid the design of electrical machines. Finite element method is used in this chapter for the analysis, performance evaluation and optimization of electromagnetic design of the outer-rotor permanent magnet generator. The modeling approach involves two-dimensional finite element boundary-value problems with specified current sources for the conductors and magnets, on the assumption that the finite element solution and external circuitry do not affect the sources.

To satisfy the requirement of identifying a convenient functional, the Galerkin approach is used in the finite element analysis to deriving the finite element equations. As a fast approach, the Newton-Raphason iteration method is employed to seek a convergent solution in the nonlinear system analysis. Dirichlet and Neumann boundary conditions are applied to the domain of a pair-pole section of the permanent-magnet generator for finite element analysis. The increments δA_i of vector potential A_i can be obtained by solving the derived matrix equations. The terminal voltages of the generator evaluated at no-load and load conditions are derived by calculating flux linkages and their products with angular velocity. The derivation of the Maxwell stress expressions is contained in this chapter. Some of the drawbacks of the B^2 method can be overcome by the Maxwell stress method for computing forces. The simulation of the electromagnetic torque and power

capability are given following the computation of the electromagnetic forces. The discussion includes some suggested improvements for performance prediction of the outer-rotor permanent magnet generator.

5.1 Introduction

Numerical techniques have long been recognized as practical and accurate methods of field computation to aid in electrical design. Solving a differential equation analytically is only possible assuming simplifications in the differential equations that are valid in a domain that can be a plain mathematical way. Specific boundary conditions and various material properties in different domains make it difficult to obtain an analytical solution for problems of technical importance. The two most popular groups of numerical methods are the finite difference method (FDM) and finite element method (FEM). Although the FDM was the technique precursory to the FEM in history, the FEM nowadays is the most important and most frequently used approach solving variational problems and differential equations in engineering. The most significant success of this method is founded in the possibility to develop on computer programs of general application range. Due to its structure rules this is
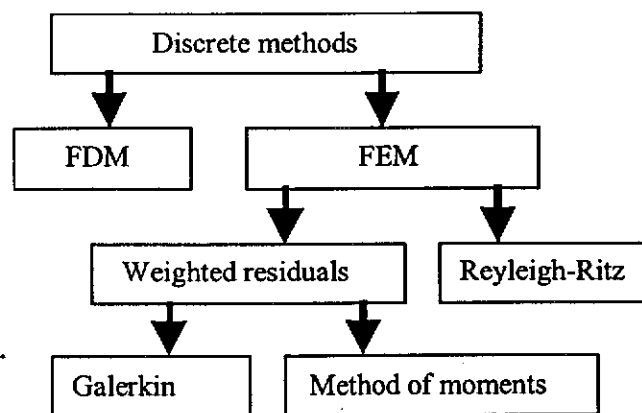
Fig. 5.1 Overview of various numerical methods

closely linked to the opportunity of the FEM to generate stable numerical schemes for considering complicated two- and three-dimensional geometry in a relatively simple way. Fig 5.1 shows the sorting of the numerical methods.

The finite element method has been proved valuable in the design, performance evaluation and optimization of electrical machinery because its elements can be easily adapted to any shape of boundary and interface geometry. The modeling approach has most commonly involved two-dimensional finite element boundary-value problems with specified current sources for the conductors. The most popular finite element methods are:

- Ritz method

- variational method

- weighted residual method

- Galerkin method

- approach based on the energy-minimum functional

In this chapter, the author has applied FEM for the analysis of the outer-rotor permanent magnet generator. Bounded by the geometry of the PM generator, the finite element analysis aims mainly at the simulation of the magnetic flux distribution, winding flux linkage as a function of rotor position, induced back EMF, electromagnetic force and torque, and power capability. In the simulation, each permanent magnet can be replaced by a simple current sheet surrounding the permanent material that has permeability equal to the recoil permeability [5.1]. For the behavior prediction and design optimization, various post-processing techniques

169

have been developed based on the finite element solutions. The Maxwell Stress method [5.2][5.3] can increase the accuracy of torque calculation by means of area integration over the air gap.
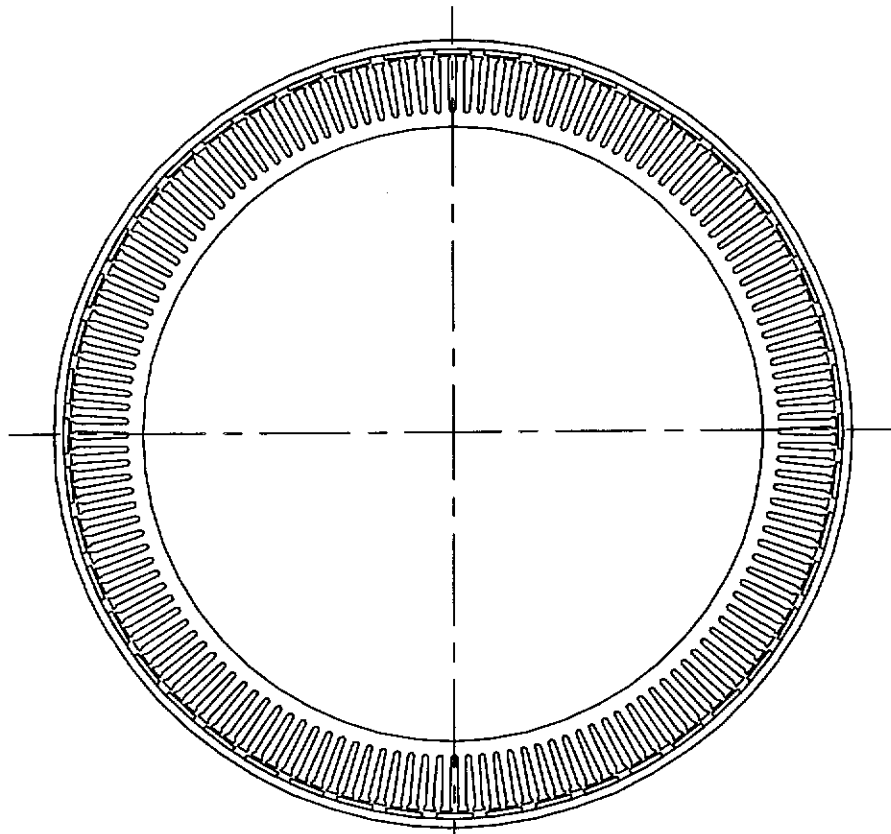
Fig. 5.2 cross section of the outer-rotor PM generator

The permanent magnet generator with outer-rotor was designed in the last chapter by using direct design method that involves the calculation of lumped parameters in magnetic and electrical circuits. In the foregoing design and linear analysis, main dimensions and major performance of the generator are determined and predicted. However, the permeability of iron core is assumed infinite (i.e. zero reluctance), and the main and leakage flux paths or permeance are considered being affected only by the geometry not the MMF levels of the magnets and armature. Also, local magnetic

saturation of the lamination is not examined. To validate the design methodologies and predict the performance of the designed PM generator more accurately, 2-dimesional finite element method is applied to the analysis of the initial design in this chapter. Fig. 5.2 shows the cross section of the PM generator on a plane perpendicular to the generator shaft. It is illustrated that there are 144 slots or teeth on the inner-stator lamination, and 48 poles made of Nd-Fe-B evenly arranged along the inside periphery of the rotor drum.

Triangle element Δijk
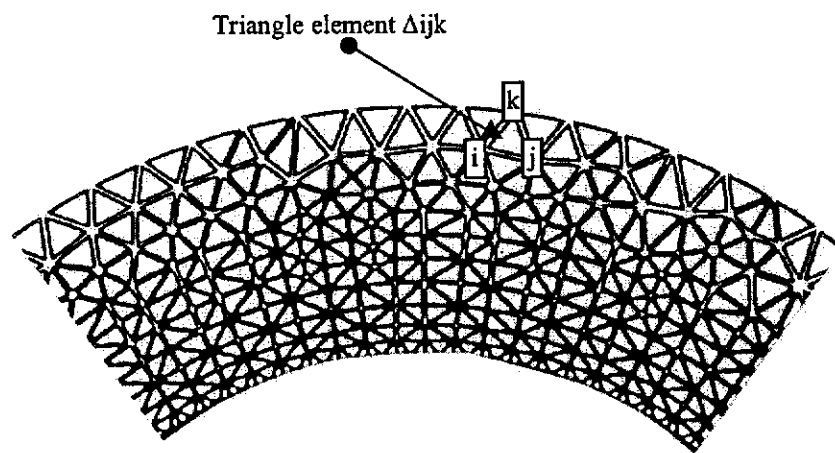
Fig. 5.3   Finite element mesh using triangles

In the finite element analysis, the problem is discretized in adequate sub-problems. The sub-problems are described by geometrically simple shaped elements (triangles) for two-dimensional problem, as shown in Fig. 5.3.   These elements form the numerical discretization, the mesh, and are so called the finite elements. On this discretization, the problem describing differential equation is locally approximated by simple basis function. The approximated overall solution is obtained by assembling all sub-problems into a system of equations and solving this. After this procedure, the approximated potential solution is known in certain points of the

discretization. The task is to determine the field describing potential functions for the discrete problem, the finite element equations, and to define an adequate basis or shape function to be able to assemble the overall system of equations.

Due to the symmetry of the machine construction, only a pair-pole segment of the entire cross-section is computed, as shown in Fig. 5.4. The computed domain is divided into about 5000 discrete elements. The precise nonlinear magnetic characteristic curves of iron core and magnets are used in FE analysis.
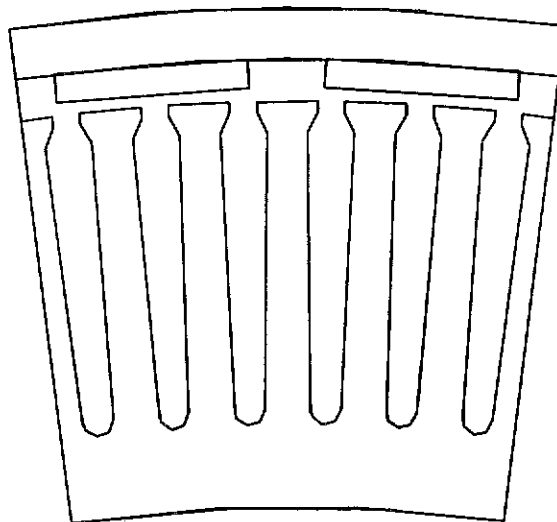
Fig. 5.4   Cross-section of one pair of pole

5.2   Finite Element Analysis for the PM Generator

5.2.1 Basic Equations of FEM for The Machine

In magnetic field the relation of magnetic flux density B, magnetic flux strength H and magnetic vector potential A meets Maxwell's equation conditions:

$$\nabla \times A = B \tag{5.1}$$

$$\nabla \times H = J_0 \tag{5.2}$$

$$\nabla \cdot B = 0 \tag{5.3}$$

$$B = \mu H \tag{5.4}$$

where J_0 is the current density and μ the permeability. So, the system of differential equations can be derived from the above equations as:

$$\nabla \times (\frac{1}{\mu} \nabla \times A) = J_0 \tag{5.5}$$

Applying the vector calculus $\nabla \times (\nabla \times A) = \nabla(\nabla \cdot A) - \nabla^2 A$ [5.14] to equation (5.5) yields:

$$\nabla(\nabla \cdot A) - \nabla^2 A = \mu J_0 \tag{5.6}$$

Since $\nabla \cdot A = 0$ [5.14] and by assuming a constant permeability μ, a Poisson equation in A-formulation of the magnetic field is obtained:

$$\nabla^2 A = -\mu J_0 \tag{5.7}$$

Describing a magnetic field alternating with an angular frequency ω, equation (5.7) can be expressed in two-dimensional Cartesian coordinate (A has only a z component) [5.15] as:

$$\frac{1}{\mu}\frac{\partial^2 A_z}{\partial x^2} + \frac{1}{\mu}\frac{\partial^2 A_z}{\partial y^2} = -J_0 + j\omega\sigma A \qquad (5.8)$$

where σ is the electrical conductivity.

Equation (5.8) is the diffusion equation for the steady state operation taking account of time harmonics. The term $j\omega\sigma A$ at the right hand of the equation represents the effect of eddy current.

In the finite element analysis of this outer-rotor generator, the steady state operation is only considered with the multi-pole and polyphase configuration. While the rotor is rotating at a speed in steady state the produced MMF by the stator also rotates at the same speed. Since the rotor is involved in a constant magnetic field ($\frac{\partial B}{\partial t} = 0$), there are no eddy currents on the rotor. An observer on the stator experiences a time varying field whose fundamental is at the system frequency. Because the stator core is laminated and the stator winding is stranded and transposed, the eddy currents are resistance limited and can be neglected in the field computation. Thus, the term $j\omega\sigma A$ in the diffusion equation (5.8) can be neglected since σ *is* equal to zero. Therefore, a Poisson's equation with respect to magnetic vector potential A is available [5.11] for the magnetostatic analysis of the outer-rotor permanent magnet generator,

$$\frac{\partial}{\partial x}(v\frac{\partial A_z}{\partial x}) + \frac{\partial}{\partial y}(v\frac{\partial A_z}{\partial y}) = -J_z - J_{zpm} \qquad (5.9)$$

174

where A_z = Z component of magnetic vector potential;

                   $v = 1/\mu$, magnetic reluctivity;

                   J_z = applied current density in circuit;

                   J_{zpm} = equivalent current density at the magnet boundary.

5.2.2 Galerkin Approach for The Finite Element Analysis

The Galerkin approach is used in the finite element analysis of the PM generator. In fact, the Galerkin approach is a special case of the Method of Weighted Residuals (MWR) and has greater generality compared with the variational approach.

Since the computation is in two-dimensional Cartesian coordinates it will not cause misunderstanding that the A_z is replaced by A in equation (5.9). Substituting an approximation, A, for A_z gives a residual R [5.16].

$$R = \frac{\partial}{\partial x}(v\frac{\partial A}{\partial x}) + \frac{\partial}{\partial y}(v\frac{\partial A}{\partial y}) + J_z + J_{zpm}$$ (5.10)

Multiplying equation (5.10) by a weighting function and setting the integral to zero [5.17], an integral functional is:

$$\iint_\Omega RWdxdy = 0$$ (5.11)

Substituting equation (5.10) for R, obtain

$$- \iint_{\Omega} W[\frac{\partial}{\partial x}(v \frac{\partial A}{\partial x}) + \frac{\partial}{\partial y}(v \frac{\partial A}{\partial y})]dxdy = \iint_{\Omega} WJ_z dxdy + \iint_{\Omega} WJ_{zpm} dxdy \qquad (5.12)$$

Using Green's theorem (see the Appendix V-2), the left-hand side of equation (5.12) is transformed to

$$- \iint_{\Omega} W[\frac{\partial}{\partial x}(v \frac{\partial A}{\partial x}) + \frac{\partial}{\partial y}(v \frac{\partial A}{\partial y})]dxdy$$

$$= \iint_{\Omega} v[(\frac{\partial W}{\partial x} \frac{\partial A}{\partial x}) + (\frac{\partial W}{\partial y} \frac{\partial A}{\partial y})]dxdy - \oint_{s} vW \frac{\partial A}{\partial n}ds \qquad (5.13)$$

where the last term is on the boundary s with n being the outward normal unit vector.

After substituting the result into Equation (5.12) the surface integral is needed to be broken into summations over small areas. The surface in the case is meshed with triangles (the finite elements) and the integral over the entire domain is replaced by the summation of the integral over the individual triangles.

$$\sum_M [v^e \iint_{\Omega_e} (\frac{\partial W^e}{\partial x} \frac{\partial A^e}{\partial x} + \frac{\partial W^e}{\partial y} \frac{\partial A^e}{\partial y})dxdy - \oint_{s} v^e W^e \frac{\partial A^e}{\partial n}ds$$

$$= \iint_{\Omega_e} W^e J_z^e dxdy + \iint_{\Omega_e} W^e J_{zpm}^e dxdy] \qquad (5.14)$$

where M is the number of triangular elements and the superscript e means an individual element.

The line integral in equation (5.14) only needs to be evaluated over elements that have a side in common with the boundary of the problem. In the section 5.2.3, it will

be demonstrated that the integral of this case can be simply set to zero because of

$\dfrac{\partial A}{\partial n} = 0$, which results in the natural boundary condition. But, when the integral is

used in the problem where the finite element method is coupled to other solution

techniques [5.13], it must be evaluated.

To discuss the detailed calculation of elements, the individual triangular element Δ_{ijk}

is taken out from Fig. 5.3 and depicted in Fig. 5.5. The convention of counter

clockwise is adopted for the numbering order of the vertices. The unknown vector

potentials at vertices or nodes should be repeatedly calculated until a satisfied

solution is obtained.

(x_k, y_k)

k

i

(x_i, y_i)

j

(x_j, y_j)
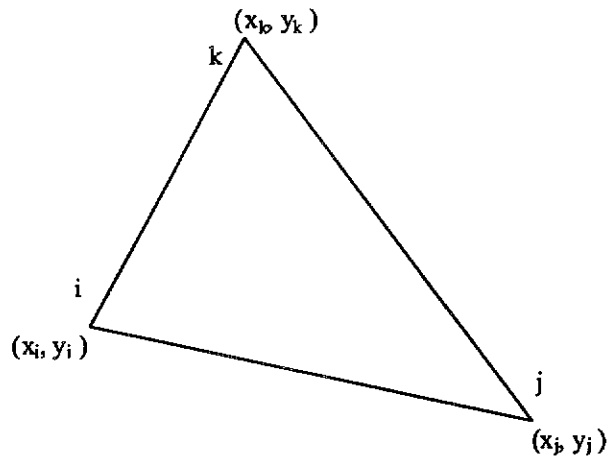
Fig. 5.5   First order triangular element

Assume that the potential varies linearly in the element. So, a linear or first order

element is obtained here. With this approximation, the vector potential may be

expressed at any point in the triangle as

$$A = \alpha_1 + \alpha_2 x + \alpha_3 y \qquad\qquad (5.15)$$

177

In the above equation, the α_1, α_2 and α_3 are constants to be determined. Since the vector potential varies linearly, the flux density, which is the derivative of the potential, is also constant in the triangle.

Let $x = x_i$, and $y = y_i$ at the vertex i. The vector potential A at this point must be equal to A_i. So,

$$\alpha_1 + \alpha_2 x_i + \alpha_3 y_i = A_i \tag{5.16}$$

Similarly for nodes j and k

$$\alpha_1 + \alpha_2 x_j + \alpha_3 y_j = A_j \tag{5.17}$$

and

$$\alpha_1 + \alpha_2 x_k + \alpha_3 y_k = A_k \tag{5.18}$$

Now, three equations can be solved for the three unknowns α_1, α_2 and α_3 in terms of the potential and geometry. Using Kramer's rule

$$\alpha_1 = \frac{\begin{vmatrix} A_i & x_i & y_i \\ A_j & x_j & y_j \\ A_k & x_k & y_k \end{vmatrix}}{\begin{vmatrix} 1 & x_i & y_i \\ 1 & x_j & y_j \\ 1 & x_k & y_k \end{vmatrix}} \tag{5.19}$$

or
$$\alpha_1 = \frac{\begin{vmatrix} A_i & x_i & y_i \\ A_j & x_j & y_j \\ A_k & x_k & y_k \end{vmatrix}}{2\Delta} \tag{5.20}$$

Similarly

$$\alpha_2 = \frac{\begin{vmatrix} 1 & A_i & y_i \\ 1 & A_j & y_j \\ 1 & A_k & y_k \end{vmatrix}}{2\Delta} \tag{5.21}$$

$$\alpha_3 = \frac{\begin{vmatrix} 1 & x_i & y_i \\ 1 & x_j & y_j \\ 1 & x_k & y_k \end{vmatrix}}{2\Delta} \tag{5.22}$$

where Δ is the area of the triangle.

Substituting equation (5.20), (5.21) and (5.22) into equation (5.15), the potential A at any point in the triangle may be expressed as

$$A = \frac{(a_i + b_i x + c_i y)A_i + (a_j + b_j x + c_j y)A_j + (a_k + b_k x + c_k y)A_k}{2\Delta} \tag{5.23}$$

where

$$
\begin{aligned}
a_i &= x_j y_k - x_k y_j, b_i = y_j - y_k, c_i = x_k - x_{j;} \\
a_j &= x_k y_i - x_i y_k, b_j = y_k - y_i, c_j = x_i - x_{k;} \\
a_k &= x_i y_j - x_j y_i, b_k = y_i - y_j, c_k = x_j - x_i
\end{aligned}
\tag{5.24}
$$

The above coefficients in the equation (5.23) are shape functions. The potential of any point in an element can be expressed as the sum of the shape functions times nodal potential.

$$A = \sum_{i=1}^{m} S_i(x,y)A_i \qquad (5.25)$$

Where S_i is the shape function and there are m nodes in the element. It is noticed that S_i equals 1 at node i and 0 at all other nodes. The sum of all the shape functions at any point in the triangle is 1.

The nodal potential in matrix form from equation (5.23) can be written as

$$A^e = (S_i^e, S_j^e, S_k^e) \begin{pmatrix} A_i^e \\ A_j^e \\ A_k^e \end{pmatrix} \qquad (5.26)$$

where

$$S_i^e = \frac{a_i^e + b_i^e x + c_i^e y}{2\Delta}$$

$$S_j^e = \frac{a_j^e + b_j^e x + c_j^e y}{2\Delta} \qquad (5.27)$$

$$S_k^e = \frac{a_k^e + b_k^e x + c_k^e y}{2\Delta}$$

The weighting function is the same as the shape function in the Galerkin method. So,

$$W^e = \begin{pmatrix} S_i^e \\ S_j^e \\ S_k^e \end{pmatrix}$$

(5.28)

Taking derivatives of A and W with respect to x and y,

$$\frac{\partial A}{\partial x} = \frac{1}{2\Delta}(b_i^e, b_j^e, b_k^e)\begin{pmatrix} A_i^e \\ A_j^e \\ A_k^e \end{pmatrix}$$

(5.29)

$$\frac{\partial A}{\partial y} = \frac{1}{2\Delta}(c_i^e, c_j^e, c_k^e)\begin{pmatrix} A_i^e \\ A_j^e \\ A_k^e \end{pmatrix}$$

and

$$\frac{\partial W}{\partial x} = \frac{1}{2\Delta}\begin{pmatrix} b_i^e \\ b_j^e \\ b_k^e \end{pmatrix}$$

(5.30)

$$\frac{\partial W}{\partial y} = \frac{1}{2\Delta}\begin{pmatrix} c_i^e \\ c_j^e \\ c_k^e \end{pmatrix}$$

With these derivatives the first term on the left side of equation (5.14) becomes

$$\nu^e \iint_{h_e} \left(\frac{\partial W^e}{\partial x}\frac{\partial A^e}{\partial x} + \frac{\partial W^e}{\partial y}\frac{\partial A^e}{\partial y}\right)dxdy$$

$$= \nu^e \left(\frac{\partial W^e}{\partial x}\frac{\partial A^e}{\partial x} + \frac{\partial W^e}{\partial y}\frac{\partial A^e}{\partial y}\right)\iint_{h_e} dxdy$$

(5.31)

where the double integral

$$\iint_{\Omega_e} dxdy = \Delta \tag{5.32}$$

Substituting equation (5.29), (5.30) and (5.32) into equation (5.31)

$$
\begin{aligned}
&v^e \iint_{\Omega_e} (\frac{\partial W^e}{\partial x}\frac{\partial A^e}{\partial x} + \frac{\partial W^e}{\partial y}\frac{\partial A^e}{\partial y})dxdy \\
&= \frac{v^e}{4\Delta}
\begin{pmatrix}
b_i^2 + c_i^2 & b_i b_j + c_i c_j & b_i b_k + c_i c_k \\
b_i b_j + c_i c_j & b_j^2 + c_j^2 & b_j b_k + c_j c_k \\
b_i b_k + c_i c_k & b_j b_k + c_j c_k & b_k^2 + c_k^2
\end{pmatrix}
\begin{pmatrix}
A_i \\
A_j \\
A_k
\end{pmatrix}
\end{aligned}
\tag{5.33}
$$

The coefficient matrix in equation (5.33) is also called stiffness matrix because of its initial use in mechanical engineering.

The force functions in equation (5.14) become

$$
\begin{aligned}
&\iint_{\Omega_e} W^e J_z^e dxdy \\
&= \iint_{\Omega_e}
\begin{pmatrix}
S_i^e \\
S_j^e \\
S_k^e
\end{pmatrix}
J_z^e dxdy \\
&= \frac{J_z^e}{2}
\begin{pmatrix}
a_i + b_i \bar{x} + c_i \bar{y} \\
a_j + b_j \bar{x} + c_j \bar{y} \\
a_k + b_k \bar{x} + c_k \bar{y}
\end{pmatrix}
= \frac{J_z^e \Delta}{3}
\begin{pmatrix}
1 \\
1 \\
1
\end{pmatrix}
\end{aligned}
\tag{5.34}
$$

and

182

$$\iint_{\Delta_e} W^e J^e_{zpm} \, dxdy$$

$$= \frac{J^e_{zpm}}{2} \begin{pmatrix} a_i + b_i \bar{x} + c_i \bar{y} \\ a_j + b_j \bar{x} + c_j \bar{y} \\ a_k + b_k \bar{x} + c_k \bar{y} \end{pmatrix} \tag{5.35}$$

$$= \frac{J^e_{zpm} \Delta}{3} \begin{pmatrix} 1 \\ 1 \\ 1 \end{pmatrix}$$

where $\bar{x}$ and $\bar{y}$ are the coordinates of the centroid of the triangular element. They are

$$\bar{x} = \frac{1}{3}(x_i + x_j + x_k)$$

$$\bar{y} = \frac{1}{3}(y_i + y_j + y_k) \tag{5.36}$$

Substituting the values in equation (5.24) into equation (5.34) and (5.35), obtain

$$\frac{a_i + b_i \bar{x} + c_i \bar{y}}{2} = \frac{a_j + b_j \bar{x} + c_j \bar{y}}{2} = \frac{a_k + b_k \bar{x} + c_k \bar{y}}{2} = \frac{\Delta}{3} \tag{5.37}$$

This leads to the final results in equation (5.34) and (5.35).

5.2.3 Boundary Conditions

A number of boundary conditions will be treated in the finite element analysis of the PM generator. It is necessary to give the description on how to make the boundary value problem be well posed. Both the bound unknown and its normal derivative must be specified at each point on the boundary so that a unique solution can be

obtained to the problem. Further, the potential of at least one point in the problem must be specified to render the global matrix non-singular. When the potential is specified at a point it is called Dirichlet condition [5.20]. If the potential is specified as constant along a line (an equi-potential) and the value of this potential is zero, this is called the homogeneous Dirichlet condition. When the normal derivative of the potential is specified it is meaning a Neumann condition [5.20]. If $\partial\phi/\partial n=0$ at the boundary, it is the homogeneous Neumann condition and is also called natural boundary condition. This is the condition we obtain by default as a result of discarding the surface integral term in equation (5.14).

5.2.3.1 Periodic boundary conditions

In this thesis, only symmetries in the geometry are considered to lead to the application of the Dirichlet or Neumann boundary conditions. As the PM generator is one type of rotating electrical machines it is of course a cylinder symmetric device. Therefore, the generator is not only symmetric in the geometry but also in the magnetic field distribution. Under load conditions the air gap field of an electrical machine repeats periodically every double pole pitch. At no-load operation, it repeats itself every pole pitch. This field periodicity can be used to define another type of boundary condition to reduce the size of the numerical model. The local potentials in such boundaries depend on the solution of the field problem and thus inherently occur always in pairs. One boundary is computed and the opposite one is linearly linked to this value. This type of periodic condition can be expressed in the form:

$$\kappa\phi_I(x) + \phi_i(x) = m \qquad\qquad (5.37b)$$

If $m=0$ and κ equals 1 or -1 this boundary is called binary condition.

5.2.3.2   Dirichlet and Neumann conditions

With periodicity, the domain of one pair-pole is used in the problem. As shown in Fig. 5.6, a homogeneous Dirichlet condition is assigned to the two arcs $\overset{\frown}{ab}$ and $\overset{\frown}{cd}$ where A = 0. The two arcs are the outer borders of the rotor and inner border of the stator respectively. Since the two lines $\overline{ad}$ and $\overline{bc}$ are located at the direct axis, a homogeneous Neumann condition is specified along the two lines where $\dfrac{\partial A}{\partial n} = 0$.

This normal derivative of the vector potential is also called natural boundary condition. In fact, the condition has been obtained by default as a result of discarding the surface integral term in equation (5.37).

In the geometry shown in Fig. 5.7, the homogeneous Dirichlet boundary condition, A = 0, is specified to the four borders. The two straight lines $\overline{ad}$ and $\overline{bc}$ are located at the quadrature axis.
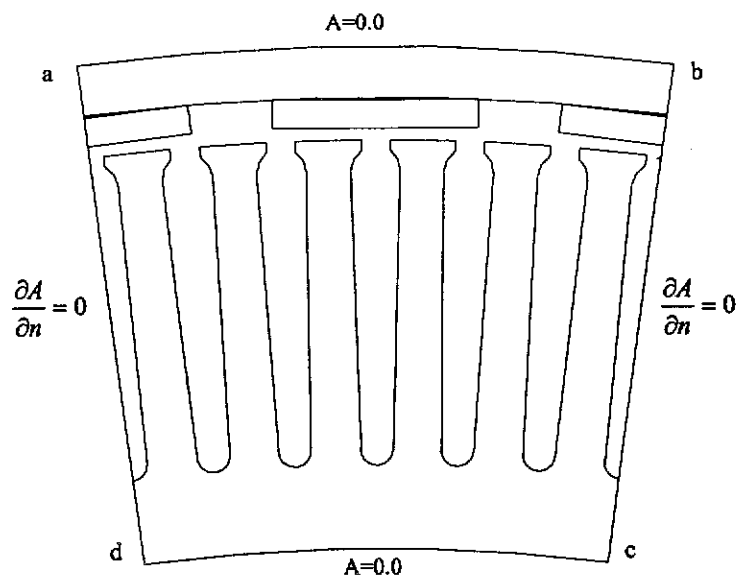
Fig. 5.6 Dirichlet and Neumann condition

For two dimensional magnetic vector potential problems, a contour of constant flux is a flux line. This can be defined by the differential equation,

$$\nabla \times A = B \tag{5.38}$$

In two-dimensional Cartesian coordinates, vector potential has only the z component A_z. The difference of A between two points multiplying length of the machine gives the flux between these points. Applying Stoke's theorem (Appendix V-3) to equation (5.38), it gives

$$L_c \oint A \cdot dl = \psi_m \tag{5.39}$$
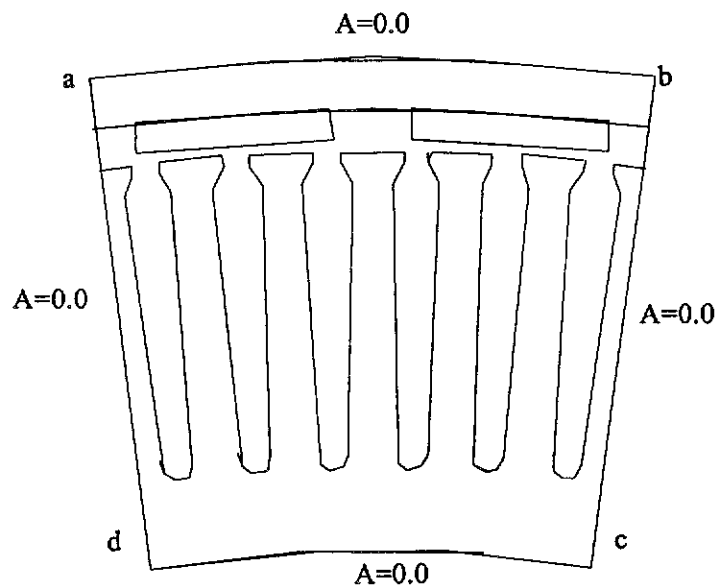
Fig. 5.7 Homogeneous Dirichlet condition

where ψ_m is the magnetic flux linking the closed path of integration. There is no contribution of paths in the x direction because of the zero dot product. The total magnetic flux between two points is then the product of the length of the machine and the difference in vector potential between these points. If the values of potential at two points are equal, no flux crosses the line connecting these points. It means that the two points are on the same equi-potential line, or on a flux line. So, the value of potential should be specified on at least one point in the problem to obtain a unique solution.

5.3 Permanent Magnets Modeling

The development of high-energy permanent magnet materials such as SmCo and Nd-Fe-B grades has led to increased interest in the use of permanent magnets in electrical machines. But, the representation of the magnetization characteristics of these permanent magnets is difficult and is still the subject of ongoing research. However, it is often acceptable to consider the magnetic characteristic of a permanent magnet by a straight line in the second quadrant of the hysteresis loop [5.4][5.5]. The 48 poles of this generator are made of Nd-Fe-B permanent magnets. It is seen, from Fig. 5.8, that the hysteresis characteristic of Nd-Fe-B has a comparatively wide loop, and it normally exhibits a linear magnetization characteristics in the second quadrant.

The intersection of the loop with the ordinate is called the residual or remanent flux density B_r. The intersection of the abscissa and the loop is called the coercive force H_c. The permanent magnet generator is designed to operate in this region. In the

design, a straight line is used to represent the magnet characteristic. But, particular attention is paid to the operating temperature of the magnets during the design of the PM generator.
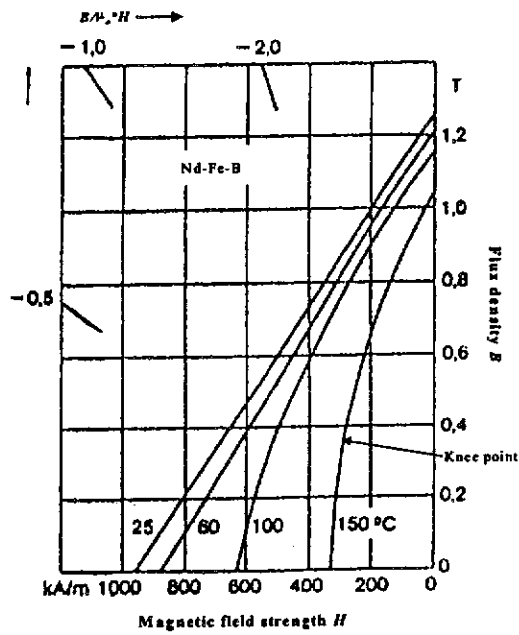
Fig. 5.8   Magnetization characteristic of Nd-Fe-B

5.3.1 Current Sheet Model of Permanent Magnet

The Nd-Fe-B magnet used in this research has a rectangular shape and specific dimension. This brings some restraint to the design of the machine. To set up a mathematical model for the Nd-Fe-B magnet the equivalent current sheet method is employed to model the permanent magnet because it is quite straightforward for rectangular magnets with magnetization parallel to two sides of the rectangle. Demerdash [5.6][5.7] improved the early form of the current sheet model such that it can be easily used on arbitrary shaped magnets like the magnetization vector approach.

188

With the repeat geometry of the 48-pole PM generator, a pair-pole part of the machine is considered in the analysis, as shown in Fig. 5.9. Firstly, it is assumed that the permeability of the core and rotor yoke (drum) is infinite. Then

$$H_m l_m + H_g \delta_g = 0$$

or $\qquad H_g = \dfrac{-l_m}{\delta_g} H_m$ (5.40)

where H_m is the magnetic field strength of the magnet, H_g the magnetic field strength in the air gap, l_m the length of the magnet in field strength direction and δ_g the length of the air gap.
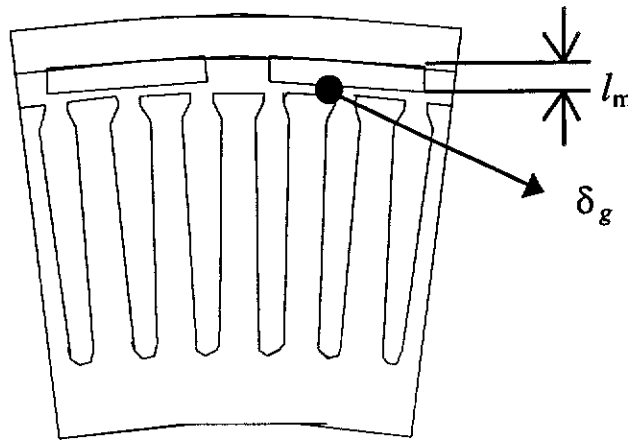
Fig. 5.9   2-pole cross section

Neglecting the fringing and corner effects, the average flux density in the air gap, B_{av}, is

$$B_{av} = -\mu_o \frac{l_m}{\delta_g} H_m$$ (5.41)

189

Equation (5.41) represents the air gap characteristic in the magnetic circuit. When applying it to the Nd-Fe-B magnet characteristic the operating point of the generator will be the intersection of the two characteristics. For a linear magnet it has

$$B = B_r + \frac{B_r}{H_c} H$$
$$B = B_r + \mu_o (1 + \chi_m) H \qquad (5.42)$$
$$B = B_r + \mu_m H$$

So, the operating point can be plotted at (H_o, B_o) shown in Fig. 5.10. The H_o in the second quadrant is negative. According to the data from the direct design, the flux density in the stator tooth keeps at a level lower than the early saturation of the silicon-steel. It will not cause any significant error to assume the operating point at the linear section.
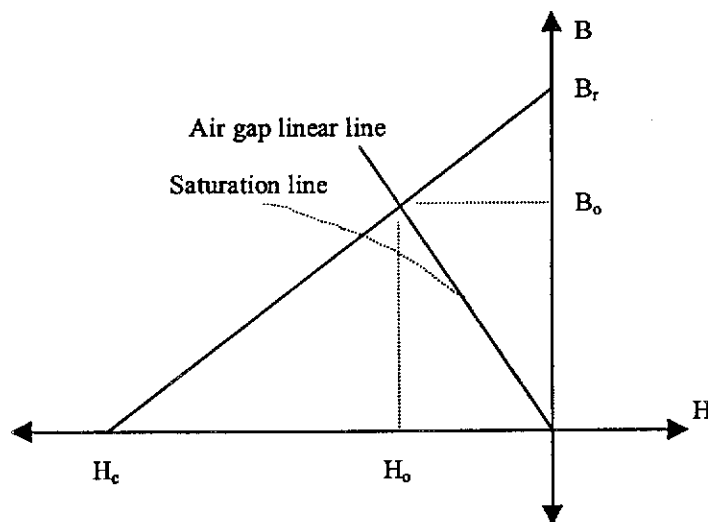
Fig. 5.10   Magnet operating point

190

H_o is negative here. If the finite permeability of the core and saturation is taken into account a modified new load curve (dotted) below the air gap line should be used to plot the saturation operating point. The flux density, then, will be lower.

The Nd-Fe-B magnet in Fig. 5.9 can be further replaced by an equivalent current sheet with total ampere turns $NI = H_c l_m$ and a material with equivalent permeability $\mu = B_r/H_c$. At the linear case the permeability of the silicon-steel is far greater than air. It has

$$H_m l_m + H_g \delta_g = H_c l_m \qquad (5.43)$$

Using the flux continuity constraint, obtain

$$\frac{H_c}{B_r} B + v_o \frac{\delta_g}{l_m} B = H_c \qquad (5.44)$$

Therefore, a thin current sheet can be added to the two sides of the magnet such that a magnetic field is produced in the direction of the magnetization. The linear current density (Amperes/meter) should be equal to H_c, the coercive force. That is $J_{zpm} = H_c$.

5.4 Newton-Raphson Method for Nonlinear Analysis

In electromagnetic calculations, the PM generator is designed to operate at or near the saturation point to achieve the most benefits. The problems in the analysis of the machine are almost nonlinear due to the presence of ferromagnetic materials. The magnetic permeability, $\mu = B/H$, is non-homogeneous and will be a function of the

local magnetic fields which are unknown at the start of the problem. As the permeability is unavoidably contained in all of the element stiffness matrices, an iterative process must be used to keep correcting the permeability until μ is consistent with the field solution. Newton-Raphson iteration technique [5.17][5.18] is used in the analysis to deal with the non-linear problem. The method is based on Newton's method for finding the roots of polynomial equation. The magnetic reluctivity, $v=1/\mu$ as a function of $|B|^2$ must be continuous and differentiable. A number of approximations are possible from polynomials to exponentials. It is known that magnetic permeability vs. flux density is not a monotonic function. The permeability is low at very low flux densities, rises quickly as flux density increases and then decreases in the saturation region. In order to guarantee convergence the permeability in the low flux density region is approximated as a constant.

At the beginning, an unsaturated value of permeability is assigned for each element in the mesh. When solving the problem, the magnitude of the flux density in each element is computed and the permeabilities are corrected to be consistent with the computed values of the flux density. The problem is then solved again using the new values. This process is continued till a satisfactory result is obtained when the difference between the current solution and the previous one is smaller than a pre-specified value.

Here, the previously derived two-dimensional nonlinear Poisson equation [5.8] for the magnetic vector potential is used. The stiffness matrix for a two-dimensional first order triangle is

$$\frac{v}{4\Delta}\begin{pmatrix} s_{ii} & s_{ij} & s_{ik} \\ s_{ji} & s_{jj} & s_{jk} \\ s_{ki} & s_{kj} & s_{kk} \end{pmatrix}\begin{pmatrix} A_i \\ A_j \\ A_k \end{pmatrix} = \frac{\Delta}{3}\begin{pmatrix} J_z \\ J_z \\ J_z \end{pmatrix} + \frac{\Delta}{3}\begin{pmatrix} J_{zpm} \\ J_{zpm} \\ J_{zpm} \end{pmatrix} \tag{5.45}$$

The values in the stiffness matrix are referred to equation (5.33). Now, let G_i, G_j and G_k represent the three equations respectively

$$
\begin{aligned}
G_i &= \frac{v}{4\Delta}\begin{pmatrix} s_{ii} & s_{ij} & s_{ik} \end{pmatrix}\begin{pmatrix} A_i \\ A_j \\ A_k \end{pmatrix} - \frac{J_z\Delta}{3} - \frac{J_{zpm}\Delta}{3} \\[2mm]
G_j &= \frac{v}{4\Delta}\begin{pmatrix} s_{ji} & s_{jj} & s_{jk} \end{pmatrix}\begin{pmatrix} A_i \\ A_j \\ A_k \end{pmatrix} - \frac{J_z\Delta}{3} - \frac{J_{zpm}\Delta}{3} \\[2mm]
G_k &= \frac{v}{4\Delta}\begin{pmatrix} s_{ki} & s_{kj} & s_{kk} \end{pmatrix}\begin{pmatrix} A_i \\ A_j \\ A_k \end{pmatrix} - \frac{J_z\Delta}{3} - \frac{J_{zpm}\Delta}{3}
\end{aligned}
\tag{5.46}
$$

The derivatives in the Newton-Raphson method can be found by differentiating these equations with respect to the nodal vector potentials. For G_i this gives

$$\frac{\partial G_i}{\partial A_i} = \frac{v}{4\Delta}s_{ii} + \frac{1}{4\Delta}(s_{ii}A_i + s_{ij}A_j + s_{ik}A_k)\frac{\partial v}{\partial B^2}\frac{\partial B^2}{\partial A_i} \tag{5.47}$$

$$\frac{\partial G_i}{\partial A_j} = \frac{v}{4\Delta}s_{ij} + \frac{1}{4\Delta}(s_{ii}A_i + s_{ij}A_j + s_{ik}A_k)\frac{\partial v}{\partial B^2}\frac{\partial B^2}{\partial A_j} \tag{5.48}$$

$$\frac{\partial G_i}{\partial A_k} = \frac{v}{4\Delta}s_{ik} + \frac{1}{4\Delta}(s_{ii}A_i + s_{ij}A_j + s_{ik}A_k)\frac{\partial v}{\partial B^2}\frac{\partial B^2}{\partial A_k} \tag{5.49}$$

The chain rule is used here to replace $\dfrac{\partial v}{\partial A}$ by $\dfrac{\partial v}{\partial B^2}\dfrac{\partial B^2}{\partial A}$. So, the Newton-Raphson

equation is

$$\frac{\partial G_i}{\partial A_i}\Delta A_i + \frac{\partial G_i}{\partial A_j}\Delta A_j + \frac{\partial G_i}{\partial A_k}\Delta A_k = -G_i(A_i, A_j, A_k) \tag{5.50}$$

Substituting equation (5.46~5.49) into (5.50)

$$\frac{v}{4\Delta}(s_{ii}\Delta A_i + s_{ij}\Delta A_j + s_{ik}\Delta A_k) +$$

$$\frac{1}{4\Delta}(s_{ii}A_i + s_{ij}A_j + s_{ik}A_k)(\frac{\partial v}{\partial B^2})(\frac{\partial B^2}{\partial A_i}\Delta A_i + \frac{\partial B^2}{\partial A_j}\Delta A_j + \frac{\partial B^2}{\partial A_k}\Delta A_k) \tag{5.51}$$

$$= -\frac{v}{4\Delta}(s_{ii}A_i + s_{ij}A_j + s_{ik}A_k) + \frac{J_z\Delta}{3} + \frac{J_{zpm}\Delta}{3}$$

Its matrix notation is

$$\frac{v}{4\Delta}(s_{ii} + s_{ij} + s_{ik})\begin{pmatrix} \Delta A_i \\ \Delta A_j \\ \Delta A_k \end{pmatrix} +$$

$$\frac{1}{4\Delta}\frac{\partial v}{\partial B^2}[(\sum_{n=i}^{k}s_{in}A_n)\frac{\partial B^2}{\partial A_i}, (\sum_{n=i}^{k}s_{in}A_n)\frac{\partial B^2}{\partial A_j}, (\sum_{n=i}^{k}s_{in}A_n)\frac{\partial B^2}{\partial A_k}]\begin{pmatrix} \Delta A_i \\ \Delta A_j \\ \Delta A_k \end{pmatrix} \tag{5.52}$$

$$= -\frac{v}{4\Delta}(s_{ii}, s_{ij}, s_{ik})\begin{pmatrix} A_i \\ A_j \\ A_k \end{pmatrix} + \frac{J_z\Delta}{3} + \frac{J_{zpm}\Delta}{3}$$

Similar process is applied to equations G_j and G_k and combining the three equations

together, obtain

$$\frac{v}{4\Delta}\begin{pmatrix} s_{ii} & s_{ij} & s_{ik} \\ s_{ji} & s_{jj} & s_{jk} \\ s_{ki} & s_{kj} & s_{kk} \end{pmatrix}\begin{pmatrix} \Delta A_i \\ \Delta A_j \\ \Delta A_k \end{pmatrix} + \frac{1}{4\Delta}\frac{\partial v}{\partial B^2}\begin{pmatrix} \sum_{n=i}^{k} s_{in} A_n & \sum_{n=i}^{k} s_{in} A_n & \sum_{n=i}^{k} s_{in} A_n \\ \sum_{n=i}^{k} s_{jn} A_n & \sum_{n=i}^{k} s_{jn} A_n & \sum_{n=i}^{k} s_{jn} A_n \\ \sum_{n=i}^{k} s_{kn} A_n & \sum_{n=i}^{k} s_{kn} A_n & \sum_{n=i}^{k} s_{kn} A_n \end{pmatrix}$$

$$\times \begin{pmatrix} \dfrac{\partial B^2}{\partial A_i} & 0 & 0 \\ 0 & \dfrac{\partial B^2}{\partial A_j} & 0 \\ 0 & 0 & \dfrac{\partial B^2}{\partial A_k} \end{pmatrix}\begin{pmatrix} \Delta A_i \\ \Delta A_j \\ \Delta A_k \end{pmatrix} \tag{5.53}$$

$$= -\frac{v}{4\Delta}\begin{pmatrix} s_{ii} & s_{ij} & s_{ik} \\ s_{ji} & s_{jj} & s_{jk} \\ s_{ki} & s_{kj} & s_{kk} \end{pmatrix}\begin{pmatrix} A_i \\ A_j \\ A_k \end{pmatrix} + \frac{J_z \Delta}{3}\begin{pmatrix} 1 \\ 1 \\ 1 \end{pmatrix} + \frac{J_{zpm}\Delta}{3}\begin{pmatrix} 1 \\ 1 \\ 1 \end{pmatrix}$$

For elements with constant permeability, the second term in the above equation is

equal to zero since $\dfrac{\partial v}{\partial B^2}$ is zero. The three vector potentials are the results from the

previous iterative calculation. For non-linear permeability, $\dfrac{\partial v}{\partial B^2}$ can be found from

the saturation part of magnetization curve of the materials. $\dfrac{\partial B^2}{\partial A_i}$ can be evaluated in

the following process. The relationship between B and A is,

$$B^2 = \left(\frac{\partial A}{\partial x}\right)^2 + \left(\frac{\partial A}{\partial y}\right)^2 \tag{5.54}$$

From equation (5.23), the derivation of the vector potential A with respect to x and y

can be obtained,

$$\frac{\partial A}{\partial x} = \frac{A_i b_i + A_j b_j + A_k b_k}{2\Delta} \tag{5.55}$$

$$\frac{\partial A}{\partial y} = \frac{A_i c_i + A_j c_j + A_k c_k}{2\Delta} \tag{5.56}$$

Substituting into equation (5.54)

$$B^2 = \frac{(A_i b_i + A_j b_j + A_k b_k)^2 + (A_i c_i + A_j c_j + A_k c_k)^2}{4\Delta^2} \tag{5.57}$$

Thus

$$\frac{\partial B^2}{\partial A_i} = \frac{b_i(A_i b_i + A_j b_j + A_k b_k) + c_i(A_i c_i + A_j c_j + A_k c_k)}{2\Delta^2} \tag{5.58}$$

Similarly,

$$\frac{\partial B^2}{\partial A_j} = \frac{b_j(A_i b_i + A_j b_j + A_k b_k) + c_j(A_i c_i + A_j c_j + A_k c_k)}{2\Delta^2} \tag{5.59}$$

$$\frac{\partial B^2}{\partial A_k} = \frac{b_k(A_i b_i + A_j b_j + A_k b_k) + c_k(A_i c_i + A_j c_j + A_k c_k)}{2\Delta^2} \tag{5.60}$$

Thus, the results of equation (5.58~5.60) can be used in equation (5.53) for the solution.

196

5.5 Flux and Flux Linkage

In this three-phase synchronous machine, the current in adjacent phase belts is phase shifted by 60° electrical. The current in the stator is also distributed in discrete slots. Arranging the current in exactly as it is will lead to poor convergence because of that fundamental quantities will be only used to compute the terminal voltage and yet the space harmonics will be automatically included in the solution. To deal with the harmonic problem in the finite element analysis the proper method is to adopt the exact values of the stator current at different rotor positions. This gives the waveform of the flux linkage from which the fundamental part is then extracted. This is a rigorous process though the number of calculations is increased by orders of magnitude.

5.5.1 Flux Distribution

ANSYS software package is used for the simulation of flux distribution [5.19]. The flux distributions of the PM generator are plotted from both the no-load and full-load conditions for the rotor rotation of a quarter pole-pitch in each plot in Figs. 5.11(a) and (b). For a clear visualization of the flux line, the stator inner bore is not applied in the figures. As can be seen that in no-load condition, the flux distribution is largely symmetric with minor distortion due to the slot effects. Flux density distribution has concentrations at the stator teeth and the rotor yoke. Leakage flux between the magnetic poles and across stator slots is negligibly small. However, once the PM generator is loaded at the rated current, the flux distortion from the symmetric distribution is obvious. It is interesting to note is the substantial leakage flux both between the magnet poles and across the stator slots. The leakage flux pattern

197

(parameter) is not only determined by the lamination geometry but also by the level of load conditions.
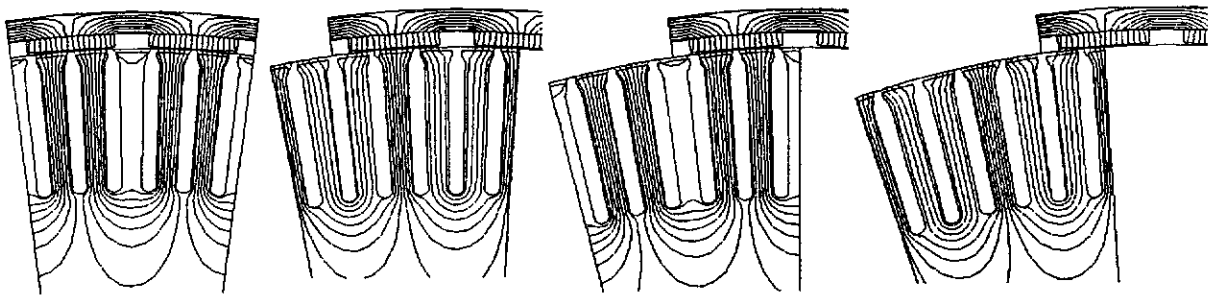
Fig. 5.11   (a) Flux distribution at no load
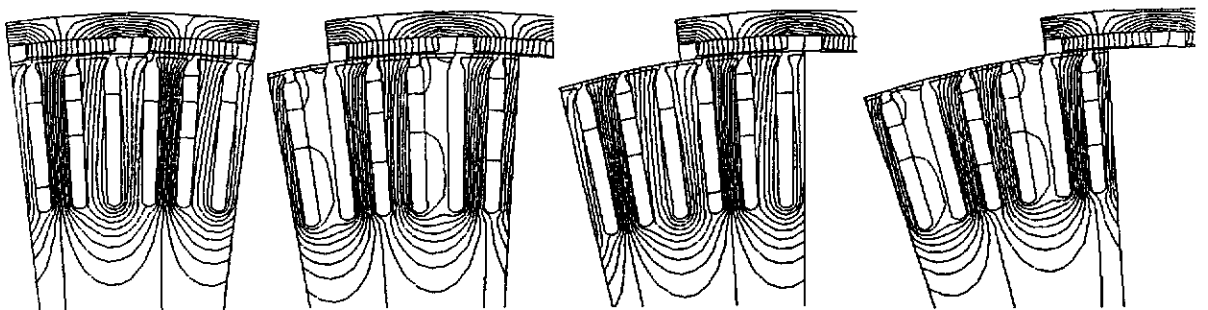
Fig. 5.11   (b) Flux distribution at full load

5.5.2 Determination of Flux Linkage

With the sought vector potential A, the flux linkage can be determined by multiplying the difference between the vector potentials at the two coil sides by the axial length of the stator core. Generally, the vector potential can be taken at the centroid of the coils without much loss of precision. More rigorous treatment would

198

involve using weighted average of the vector potential at a number of points in the coil. So, the total flux linkage of one phase is

$$\psi_p = l \sum_{i=1}^{n} \Delta A_i$$

(5.61)

where l is the length of the stacked lamination, i the number of the coils and ΔA the difference of vector potentials across one coil (two sides).

The coils in the prototype generator are arranged in full-pitch and each has 180° electrical phase shift between two sides. As there is only one coil per pole per phase the difference of vector potential of one phase is just equal to the one of a coil. Thus, the winding flux linkage ψ_{coil} is computed by the integral below:

$$\psi_{coil} = L_c \int_{a1}^{a2} \frac{\partial A_z}{\partial \ell} d\ell = A_z(a_1) - A_z(a_2)$$

(5.62)

where $A_z(a_1)$ and $A_z(a_2)$ are the vector potentials at the locations of the two sides of a coil, and L_c is the effective length of the coil. Note that the profile of the winding flux linkages determines the waveform of the induced back EMF. The computed phase winding flux linkages are shown in Fig. 5.12(a) and (b).
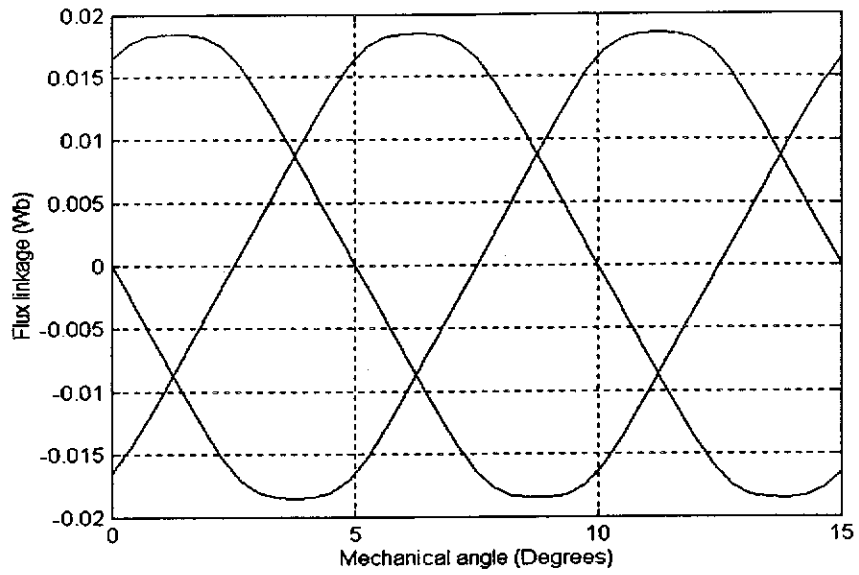
Fig. 5.12 (a) Winding flux linkage at no-load
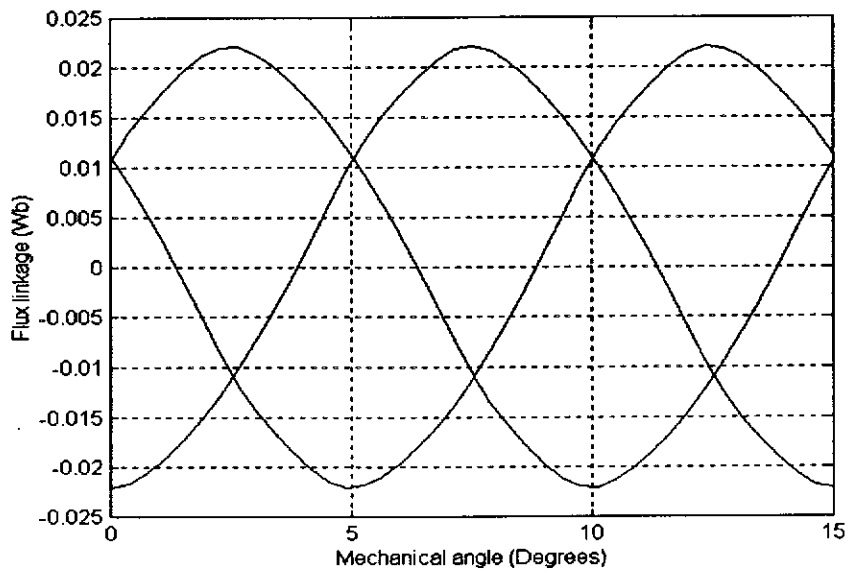
Fig. 5.12 (b) Winding flux linkage at full load

5.6   Back EMF and Terminal Voltage

For the three phase machine the peak flux linkage of each phase (ψ_a, ψ_b and ψ_c) is the same and is delayed from each other by $2\pi/3$ electrical degrees. The relationship between output line voltage and flux linkages is given by

$$E_{l\text{-}l} = \omega \sqrt{\psi_a^2 + \psi_b^2 + \psi_c^2}$$

(5.63)

Where the $E_{l\text{-}l}$ is the RMS line to line voltage, ω is the angular frequency, and ψ_a, ψ_b and ψ_c are the flux linkages of phase A, B, and C. To find peak value of the phase voltage, multiply the $E_{l\text{-}l}$ by $\sqrt{\dfrac{2}{3}}$. The phase angle of the voltage is the same as the phase angle of the corresponding flux linkage. In a symmetrical system, the voltage leads its corresponding flux linkage by 90 electrial degree since $E = j\omega\psi$. They are

$$\psi_a = \psi_p \angle \theta$$
$$\psi_b = \psi_p \angle \theta - \frac{2\pi}{3}$$
$$\psi_c = \psi_p \angle \theta - \frac{4\pi}{3}$$

(5.64)

where θ is the angle between the peak of the phase a flux linkage and the phase a current. Since ψ_a, ψ_b and ψ_c are known from the finite element computations, θ can be found by solving any one of the equations (5.64). Reversely, the peak flux linkage of one phase can be obtained from the phase voltage by

$$\psi_p = \frac{E_a}{\omega} \qquad\qquad (5.65)$$

Without armature reaction the Poisson's equation (5.9) does not contain the applied current density J_z in circuit. The voltage computed from equation (5.63) is open-circuit voltage or back EMF. Because the slot number per pole per phase of the generator is only one with fully pitched single-layer windings, it is not difficult to understand that the flux linkage and back EMF of this generator can easily depart from a regular sine wave. Fig. 5.13 shows the simulated waveform and value of the no-load induced back EMF at 170 rpm, which is derived from the flux linkage shown in Fig. 5.12 (a).

For comparison, the waveform of the phase voltage taken from no-load test is shown in Fig. 5.14. Basically, the two waveforms are similar. But a slight difference can be seen that the practical waveform within half of cycle is not symmetrical with respect to Y-axis. The reason is that the previous load tests resulted in this slightly distorted field of the magnet.

A comparison of the output voltage at open-circuit is made between computation and measurement. Fig. 5.15 shows the output line to line voltage versus rotating speed. The computed line voltage is drawn from the designed data modified by finite element analysis. It is seen that a very good agreement has been achieved between the design and test results.
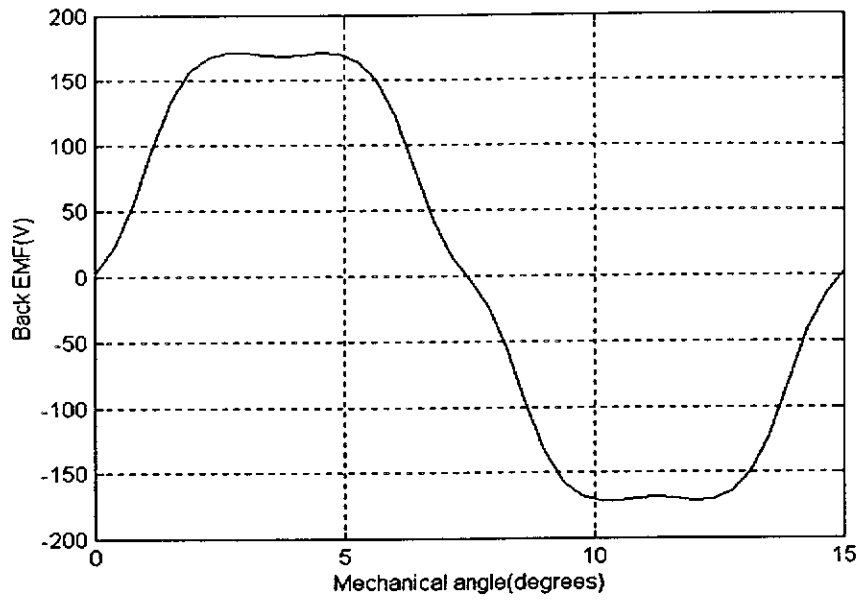
Fig. 5.13   Induced back EMF at no load
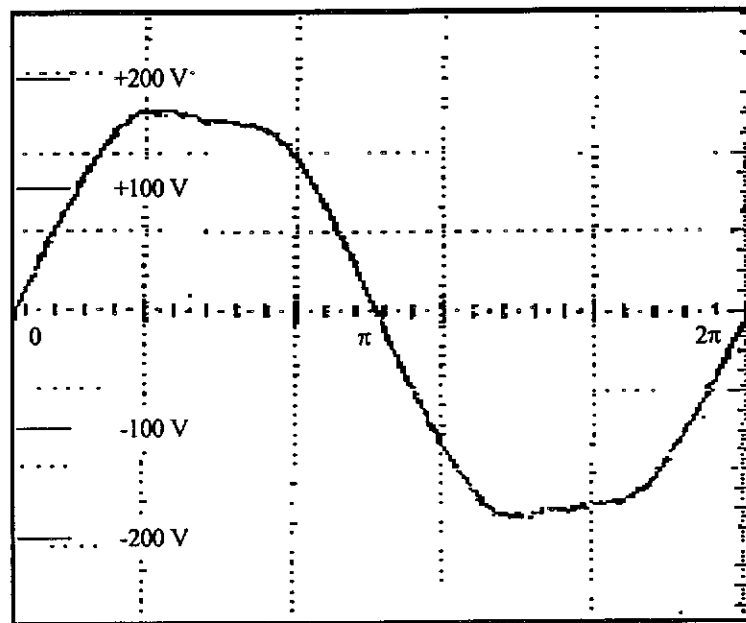
Fig. 5.14   Waveform of no-load voltage at 170 rpm
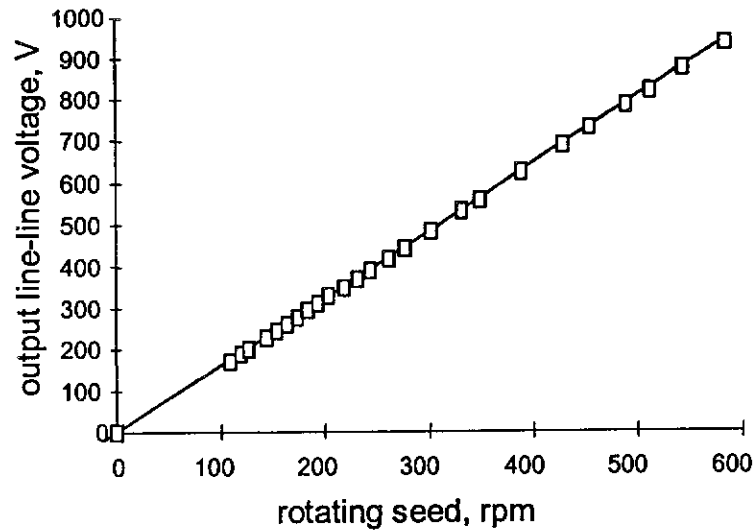
□ measured

────predicted

Fig. 5.15   Open-circuit characteristic

As described in section 4.8.3, Chapter Four, the prototype generator was also tested with a symmetrical 3-phase resistive load. In the test, the waveforms of armature voltage and current varied with the different load resistance. During the load test, it was noticed that although the no-load voltage waveform was not truly sinusoidal, the voltage waveforms became more sinusoidal when the load current was increased. The larger the load current, the more sinusoidal the output voltage tended to be, indicating an obvious reduction of the other harmonics. This improving trend of waveform enhanced when load current increased as a result of either the load resistance reducing at a certain frequency, or frequency increasing at a constant load resistance. Fig. 5.16 shows the improved voltage waveform with the resistance of 11Ω, at the speed of 170 rpm.
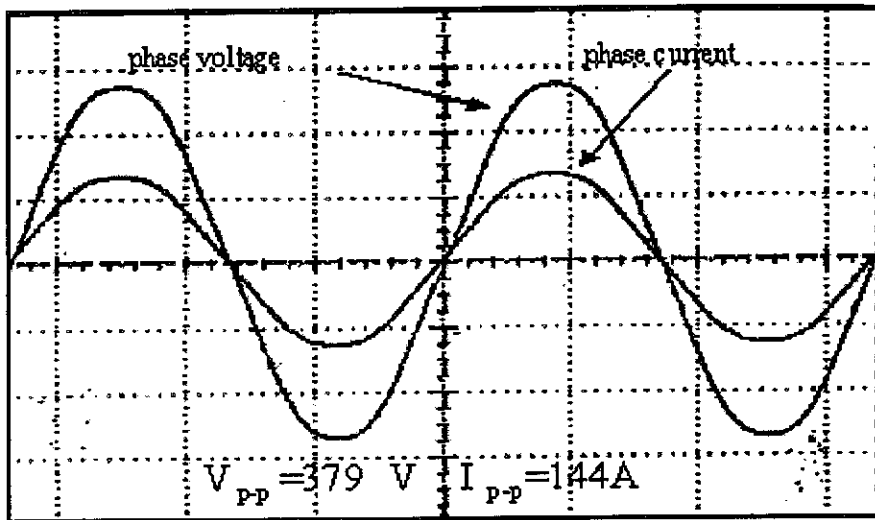
Fig. 5.16   Output waveform at resistive load

5.7   Force, Torque and Power Capability

Theoretically, the electromagnetic forces can be computed directly from the local field solution. However, the force converges much more slowly than the field solution. The Maxwell stress tensor method is probably the most common approach to determine electromagnetic forces. Based on the energy, the Maxwell stress tensor method describes the forces directly in terms of the magnetic field strength. The advantage of this method is that forces can be determined with only one FEM-solution.

5.7.1 Force and Torque Calculation By Maxwell Stress Method

Maxwell stress approach computes the local stress at all points of a bounding surface and then sums the local stresses (using a surface integral) to find the overall force.

Maxwell's stress tensor T is used for the expression of volume forces with the help of field and forces on the surface of the body. The force acting on element d*l* of a conductor or magnet with current or equivalent current *I* in a magnetic field *B* can be expressed from Biot-Savart's [5.9] law,

$$dF = I(dl \times B) \qquad (5.66)$$

The force per unit volume is called Lorentz force density [5.10].

$$f_\upsilon = J \times B = J \times \nabla \times A \qquad (5.67)$$

Also, from the Maxwell's electromagnetic equation

$$\nabla \times H = J \qquad (5.68)$$

In the constitutive relationship, $B = \mu_o H$, equation (5.67) becomes

$$
\begin{aligned}
f_\upsilon &= (\nabla \times \frac{B}{\mu_o}) \times B \\
&= \frac{1}{\mu_o}[B_z(\frac{\partial B_x}{\partial z} - \frac{\partial B_z}{\partial x}) - B_y(\frac{\partial B_y}{\partial x} - \frac{\partial B_x}{\partial y})]\vec{a}_x \\
&+ \frac{1}{\mu_o}[B_x(\frac{\partial B_y}{\partial x} - \frac{\partial B_x}{\partial y}) - B_z(\frac{\partial B_z}{\partial y} - \frac{\partial B_y}{\partial z})]\vec{a}_y \\
&+ \frac{1}{\mu_o}[B_y(\frac{\partial B_z}{\partial y} - \frac{\partial B_y}{\partial z}) - B_x(\frac{\partial B_x}{\partial z} - \frac{\partial B_z}{\partial x})]\vec{a}_z
\end{aligned}
\qquad (5.69)
$$

where the $\vec{a}_x$, $\vec{a}_y$ and $\vec{a}_z$ are the unit vector in x, y and z direction respectively. First,

consider the x component of the force density

$$f_x = \frac{1}{\mu_o}(B_z \frac{\partial B_x}{\partial z} - B_z \frac{\partial B_z}{\partial x} - B_y \frac{\partial B_y}{\partial x} + B_y \frac{\partial B_x}{\partial y}) \qquad (5.70)$$

Without changing the mean, add and subtract the quantity $\dfrac{1}{\mu_o} B_x \dfrac{\partial B_x}{\partial x}$ to equation

(5.70),

$$f_x = \frac{1}{\mu_o}(B_x \frac{\partial B_x}{\partial x} + B_z \frac{\partial B_x}{\partial z} + B_y \frac{\partial B_x}{\partial y} - B_x \frac{\partial B_x}{\partial x} - B_z \frac{\partial B_z}{\partial x} - B_y \frac{\partial B_y}{\partial x}) \qquad (5.71)$$

Using the derivative relationship

$$B_p \frac{\partial B_p}{\partial q} = \frac{1}{2} \frac{\partial B_p^2}{\partial q} \qquad (5.72)$$

Obtain

$$f_x = \frac{1}{\mu_o}[\frac{1}{2} \frac{\partial B_x^2}{\partial x} + B_z \frac{\partial B_x}{\partial z} + B_y \frac{\partial B_x}{\partial y} - \frac{1}{2} \frac{\partial}{\partial x}(B_x^2 + B_y^2 + B_z^2)] \qquad (5.73)$$

Using the definition of divergence

$$divF = \nabla \cdot F = \frac{\partial F_x}{\partial x} + \frac{\partial F_y}{\partial y} + \frac{\partial F_z}{\partial z} \qquad (5.74)$$

Reorganizing equation (5.73), it gives

$$f_x = \frac{1}{\mu_o}[\frac{\partial}{\partial x}(B_x^2 - \frac{1}{2}|B|^2) + \frac{\partial}{\partial y}(B_x B_y) + \frac{\partial}{\partial z}(B_x B_z) - B_x \nabla \cdot B] \qquad (5.75)$$

Since $\nabla \cdot B = 0$, equation (5.75) can be re-written as

$$f_x = \frac{1}{\mu_o}[\frac{\partial}{\partial x}(B_x^2 - \frac{1}{2}|B|^2) + \frac{\partial}{\partial y}(B_x B_y) + \frac{\partial}{\partial z}(B_x B_z)] \qquad (5.76)$$

The equation can be regarded as in the form of the divergence of a vector, T_x whose x, y and z component are defined as

$$T_{xx} = \frac{1}{\mu_o}(B_x^2 - \frac{1}{2}|B|^2)$$

$$T_{xy} = \frac{1}{\mu_o}(B_x B_y) \qquad (5.77)$$

$$T_{xz} = \frac{1}{\mu_o}(B_x B_z)$$

So, equation (5.76) can be expressed as

$$f_x = \nabla \cdot T_x = \frac{\partial T_{xx}}{\partial x} + \frac{\partial T_{xy}}{\partial y} + \frac{\partial T_{xz}}{\partial z} \qquad (5.78)$$

208

Similar deductive procedure is applied to seek y and z component of the force density in equation (5.69). Thus

$$f_y = \nabla \cdot T_y = \frac{\partial T_{yx}}{\partial x} + \frac{\partial T_{yy}}{\partial y} + \frac{\partial T_{yz}}{\partial z} \tag{5.79}$$

$$f_z = \nabla \cdot T_z = \frac{\partial T_{zx}}{\partial x} + \frac{\partial T_{zy}}{\partial y} + \frac{\partial T_{zz}}{\partial z} \tag{5.80}$$

Let the three vectors T_x, T_y and T_z be the x, y and z components of the Maxwell's stress tensor T. It gives

$$T = \frac{1}{\mu_o} \begin{pmatrix} B_x^2 - \frac{1}{2}|B|^2 & B_x B_y & B_x B_z \\ B_y B_x & B_y^2 - \frac{1}{2}|B|^2 & B_y B_z \\ B_z B_x & B_z B_y & B_z^2 - \frac{1}{2}|B|^2 \end{pmatrix} \tag{5.81}$$

Thus, the Lorentz force density can be expressed as the divergence of the Maxwell's stress tensor.

$$f_v = \nabla \cdot T \tag{5.82}$$

The total force can be found by integrating the force density over the volume.

$$F = \int_v \nabla \cdot T d\upsilon \tag{5.83}$$

According to the vector divergence theorem equation (5.83) can be transformed into a surface integral below,

$$F = \oiint T dx dy \tag{5.84}$$

The finite element method is only applied in two-dimensional geometry in analysis of this PM generator. Since the depth of the domain is a constant (in machine shaft direction), the surface integral can be further simplified into a loop line integral.

$$F = \oint L_c T dl \tag{5.85}$$

where L_c is a constant, the axial length of the stator core, and dl is the differential length along the integral path. The unit normal and tangential vectors to the surface are

$$\vec{a}_n = -\sin\theta \cdot \vec{a}_x + \cos\theta \cdot \vec{a}_y \tag{5.86}$$

$$\vec{a}_t = \cos\theta \cdot \vec{a}_x + \sin\theta \cdot \vec{a}_y \tag{5.87}$$

where θ is the angle between the force direction and x-axis, and $\vec{a}_x$ and $\vec{a}_y$ are unit vectors in x- axis and y-axis direction.

Then, the incremental force is

$$dF = L_c T ds = L_c T \vec{a}_n dl \tag{5.88}$$

In two-dimensional system it gives

$$
d\vec{F} = \begin{pmatrix} d\vec{F}_x \\ d\vec{F}_y \end{pmatrix}
$$
$$
= \frac{L_c dl}{\mu_o} \begin{pmatrix} B_x^2 - \frac{1}{2}|B|^2 & B_x B_y \\ B_y B_x & B_y^2 - \frac{1}{2}|B|^2 \end{pmatrix} \begin{pmatrix} -\sin\theta \\ \cos\theta \end{pmatrix} \tag{5.89}
$$

The tangential component of the incremental force is

$$
\begin{aligned}
dF_t &= d\vec{F} \cdot \vec{a}_t \\
&= d\vec{F}_x \cos\theta + d\vec{F}_y \sin\theta \\
&= \frac{L_c dl}{\mu_o}[B_x B_y (\cos^2\theta - \sin^2\theta) + \cos\theta \sin\theta (B_y^2 - B_x^2)]
\end{aligned} \tag{5.90}
$$

The normal component is

$$
\begin{aligned}
dF_n &= d\vec{F} \cdot \vec{a}_n \\
&= d\vec{F}_x(-\sin\theta) + d\vec{F}_y \cos\theta \\
&= \frac{L_c dl}{\mu_o}[B_x^2 \sin^2\theta + B_y^2 \cos^2\theta - \frac{1}{2}|B|^2 - 2B_x B_y \cos\theta \sin\theta]
\end{aligned} \tag{5.91}
$$

To find the relationship between force and flux density consider the tangential and normal components of the flux density

$$B_t = \vec{B} \cdot \vec{a}_t = B_x \cos\theta + B_y \sin\theta \tag{5.92}$$

$$B_n = \vec{B} \cdot \vec{a}_n = -B_x \sin\theta + B_y \cos\theta \tag{5.93}$$

The product of the two components is

$$
\begin{aligned}
B_n B_t &= -B_x^2 \cos\theta \sin\theta + B_x B_y \cos^2\theta - B_x B_y \sin^2\theta + B_y^2 \cos\theta \sin\theta \\
&= B_x B_y (\cos^2\theta - \sin^2\theta) + \cos\theta \sin\theta (B_y^2 - B_x^2)
\end{aligned}
\tag{5.94}
$$

and

$$
\begin{aligned}
B_n^2 &- B_t^2 \\
&= B_x^2 \sin^2\theta - 2B_x B_y \cos\theta \sin\theta + B_y^2 \cos^2\theta \\
&\quad - (B_x^2 \cos^2\theta + 2B_x B_y \cos\theta \sin\theta + B_y^2 \sin^2\theta)
\end{aligned}
\tag{5.95}
$$

Adding and subtracting $B_x^2 \sin^2\theta + B_y^2 \cos^2\theta$ from equation (5.95), obtain

$$
\begin{aligned}
B_n^2 &- B_t^2 \\
&= 2B_x^2 \sin^2\theta - 2B_x B_y \cos\theta \sin\theta + 2B_y^2 \cos^2\theta \\
&\quad - (B_x^2 \sin^2\theta + B_x^2 \cos^2\theta + 2B_x B_y \cos\theta \sin\theta + B_y^2 \sin^2\theta + B_y^2 \cos^2\theta) \\
&= 2B_x^2 \sin^2\theta - 4B_x B_y \cos\theta \sin\theta + 2B_y^2 \cos^2\theta - (B_x^2 + B_y^2)(\cos^2\theta + \sin^2\theta) \\
&= 2B_x^2 \sin^2\theta + 2B_y^2 \cos^2\theta - |B|^2 - 4B_x B_y \cos\theta \sin\theta \\
&= 2(B_x^2 \sin^2\theta + B_y^2 \cos^2\theta - \frac{1}{2}|B|^2 - 2B_x B_y \cos\theta \sin\theta)
\end{aligned}
$$

$$\tag{5.96}$$

It is seen, from equations (5.90) and (5.91) and (5.95) and (5.96), that

$$dF_t = L_c \frac{B_n B_t}{\mu_o} dl \tag{5.97}$$

$$dF_n = L_c \frac{B_n^2 - B_t^2}{2\mu_o} dl \tag{5.98}$$

The tangential and normal components of the force density are then

$$f_t = \frac{B_n B_t}{\mu_o} \tag{5.99}$$

$$f_n = \frac{B_n^2 - B_t^2}{2\mu_o} \tag{5.100}$$

With the vector normal being identical with the radial direction the machine torque can be calculated by multiplying tangential force by the length of force arm that is from the center of shaft to the point the force acts on. Since a pair of pole geometry is used in analysis and there are 48 poles distributed in the generator, the total torque yielded in the machine should be 24 times of the torque produced within one pair of pole. Fig. 5.17 shows the computed torque of full load at 170 rpm by finite element method.
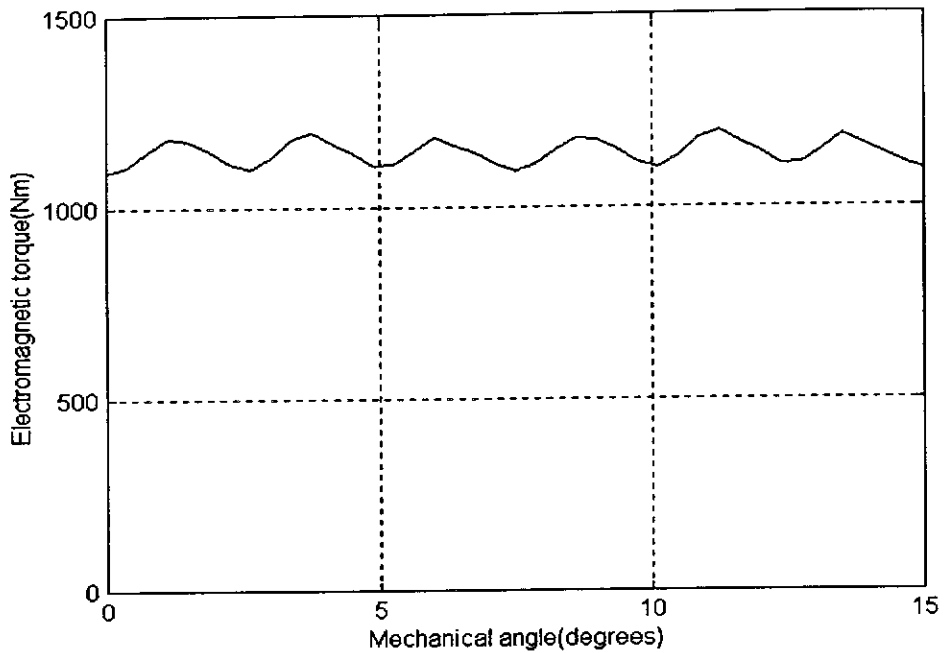
Fig. 5.17 Computed torque at full load

Fig. 5.18 shows the measured torque characteristics against output power at 170 rpm, which is drawn from the test data of the resistive load test. According to the test results, the PM machine had shaft torque of 1268 N-m at output power of 20 kW. Differentiating from that, the simulation of finite element method shows a computed electromagnetic torque of 1160 N-m at the same output power. The main reasons to cause this difference are mechanical loss, eddy loss and extra copper loss due to temperature variation. In practice, the PM generator needs more input power to overcome this dissipated energy to deliver the same output power. However, these factors are not included in the finite element analysis for steady-state operation.
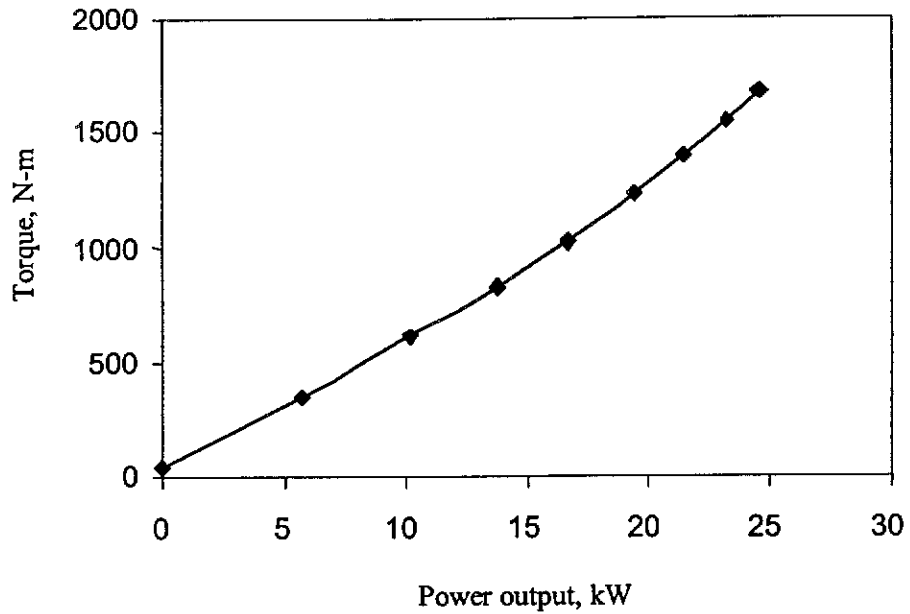
Fig. 5.18   Experimental torque versus output power

5.7.2 Power Capability

Finite element method is also used to investigate the power capability of the designed PM generator. For power computation the load currents are fed into the stator windings and the magnetic field is calculated. Then, Maxwell tensor method is applied to obtain power production. The delivery power through magnetic field is related to the torque by

$$P = \omega T = 2\pi n T/60 \qquad (5.101)$$

Where n is the rotating speed in rpm, ω the rotating angle in radian and T the torque in N-m. Result of the power calculation at 170 rpm is given in Fig. 5.19. Obviously, the designed PM generator is fully capable of delivering the expected power.
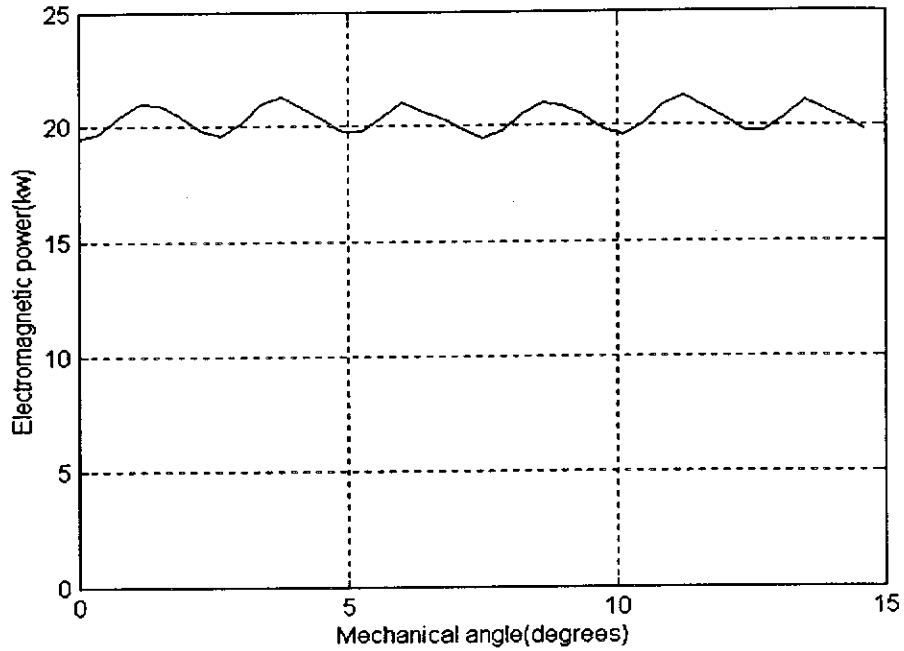
Fig. 5.19　Computed power output at full load

The power capability of this prototype PM generator is also tested under various loading conditions at 6 different rotational speeds. The output power at each of these speeds is shown in Fig. 5.20. When the output power of the generator reached 20 kW at the speed of 170 rpm, the measured load current was 50.9 A, phase voltage 134 V and the efficiency about 86%. After one hour' full load test, the measured temperature rise of the stator armature was 57°C at the ambient temperature of 31°C. These results clearly demonstrate the success of the outer-rotor PM generator specified in the original design.
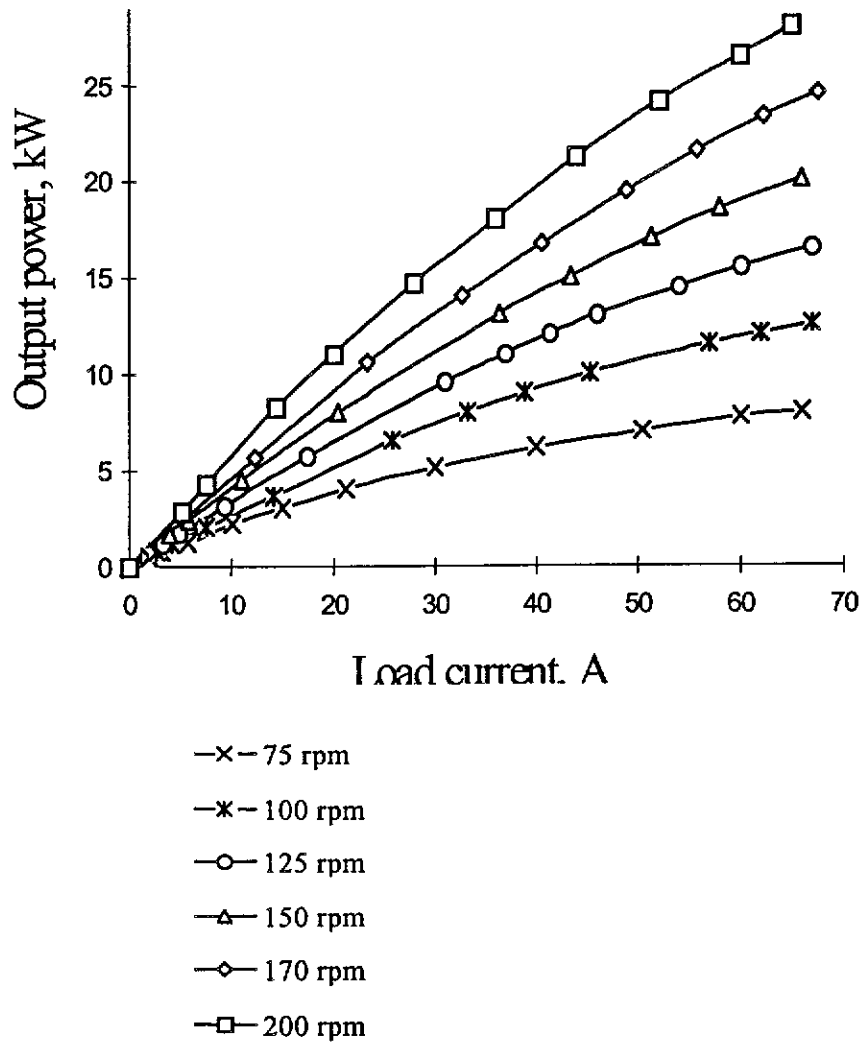
Fig. 5.20   Test output power at different rotation

5.8   Conclusions and Discussion

The finite element method has been applied to this type of generator for improving

design from conventional method and evaluating the performance under possible

conditions of magnetic saturation. The Galerkin approach has been used in finite

element analysis on the design of the outer-rotor permanent magnet generator. The

approach, in fact, is one form of the method of weighted residuals and used in this

chapter for solving two-dimensional linear electromagnetic field problem. The direct advantage of the variational formulation is that the energy functional related to the physical concept of energy. However, the approach has its weakness that for every equation to be solved a functional needs to be identified at its minimum to satisfy the differential equation being solved. For the differential equation with operator ∇ operating on the unknown f, $\nabla(f) = 0$ over the domain Ω, the variational function gives

$$L(f) = \iint_\Omega \nabla^2(f) dx dy \qquad (5.102)$$

It needs to yield symmetric matrices for the Poisson's equation with the term $\nabla^2 A$. But it requires at least a second order polynomial trial function for the unknown f to ensure that the second derivative of the functional shall not vanish. This is not always a convenient way. Obviously, from the derivation of the Galerkin method in Section 5.2.2, the difficulty to identify a convenient functional can be overcome by the Galerkin approach to finite elements.

Newton-Raphson method has been adopted to deal with the non-linear problems of electromagnetic field where magnetic permeability is a function of the local magnetic field. Although the designed generator has a different construction from normal synchronous machines, it is reasonable to use a standard method of mesh generation to produce triangular elements within the domain. As an adaptive mesh generator, the mesh refinements were weighted toward the region of high flux density, varying with the vector potential, distributed elements.

To achieve a convergent solution, finite element method is presented in the process of deriving the true energy functional for problem condition and transforming the domain of continuum problem into a number of discrete triangular elements. These elements represent the geometry, own the material characteristics of the medium, and define the approximation to the magnetic field in the region. The required field solution is obtained by minimizing the energy functional through a set of approximate functions. Periodicity condition for rotating electrical machinery has been used in the finite element method so that a much smaller area, a section of 2-pole, is analyzed rather than the entire region of 48-pole. This saves the computer space and accelerates the computation speed. The current sheet method for modeling a Nd-Fe-B magnet effect on the magnetic field has been used in solving energy functional of the PM generator. The method is suited for used with two-dimensional magnetic vector potential models for the analysis of magnetic fields under no-load and load conditions of the outer-rotor machine. The Maxwell stress method is one of the most popular methods used to calculate global force and torque in finite element method. The simulation of force and torque shows well-behaved results by employing the Maxwell stress method.

The finite element method is effectively used for detailed analysis and further modification of the preliminary design based on the initial scheme made by conventional design program with lumped-parameter calculation. As the knowledge of parameters is of importance for the correct performance prediction and design optimization of the permanent magnet generator, calculation of the main parameters is a significant part of the design. Basically, the theoretically predicted output characteristics of the generator have good agreement with the experimental results,

particularly at no-load and normal load condition. However, discrepancy between computed and measured values occurred at higher frequency and over load conditions, as shown in Fig. 5.21. Regardless the error yielded by testing system such as inductive component of load resistor, and phase imbalance of load and input voltages, etc., the discrepancies are caused by following reasons:
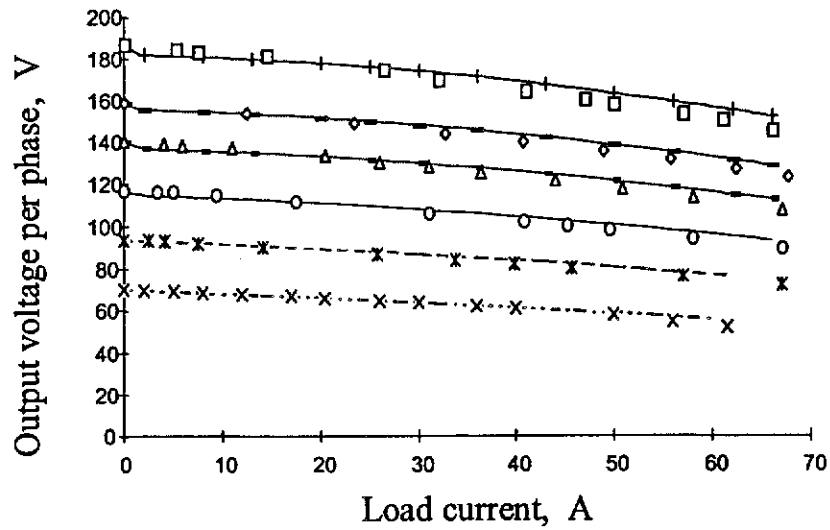
Fig. 5.21   Output characteristic at different speeds

1) Magnetic conditions varied with a more complex function of resultant total flux in the generator rather than only q-axis saturation.

2) The variation of d-axis synchronous reactance X_d and q-axis synchronous reactance X_q is a function of load current and rotating speed.

3) Stator winding resistance varies with temperature or load current. However, a constant resistance was used in the computation.

The author realized that the calculation of L_d and L_q by the process [5.12] is not accurate enough to fit the actual load conditions of the permanent magnet generator. So, an improvement is put forward that the computation of X_d and X_q could be done by applying finite element method at a number of different load and speed conditions from low to high values.

When calculating the direct axis synchronous reactance in steady state performance of this generator, the current can be considered sinusoidally distributed in the stator winding. So, it is reasonable to assume that the produced field peaks at the direct axis and the current peaks at quadrature axis. Without excitation, the inductance of the direct axis winding in this situation is synchronous reactance X_d, and inductance is flux linkage per ampere of current.

$$L = \frac{\psi}{I} \tag{5.88}$$

It is not difficult to find the flux linkage passing through a coil from the vector potential solution. As known from equation (5.45), this is just the difference of the vector potential across the two sides of the coil times the depth of the domain. Therefore, the relation between the flux linkage and vector potential is

221

$$\psi = NI\Delta A \tag{5.89}$$

where N is the number of turns and ΔA the difference of the vector potential at the location.

If periodic boundary conditions are still used for the model of one pair-pole, the inductance computed by the way is per phase per pair-pole. The inductance per phase can be obtained by multiplying the number of pair-pole of the machine, and divided by the number of parallel branches. Provided that the fictitious direct axis winding has the same number of turns as the phase winding and there is an m-phase winding in the machine. The d-axis current would have to be $m/2$ times as great as the phase current to produce the same MMF in the d-axis as the m-phase winding. So, the inductance per phase is

$$L_d = \frac{L}{m/2} \tag{5.90}$$

Then, the per unit value of X_d is

$$X_d = \frac{\omega L_d}{Z} \tag{5.91}$$

The same way can be used to find the quadrature axis reactance. The quadrature axis winding should be displaced in space by 90° electrical. In a homogenous boundary condition, the ratio of quadrature axis flux linkage to quadrature axis current is the quadrature axis synchronous inductance.

5.9 References

[5.1] Weiss, J., Garg, V.K., Shah, M. and Sternheim, E., (1984), "Finite element analysis of magnatic fields with permanent magnets", IEEE Transactions on Magnetics, Vol. MAG-20, No.5, pp.1933-1935.

[5.2] Reyne, G., Sabonnadiere, J.C. and Imhoff, J.F., (1988), "Finite element modeling of electromagnetic force density in DC machines", IEEE Transaction on Magnetics, Vol. 24, (6), pp. 3171-3173.

[5.3] Reyne, G., Sabonnadiere, J.C., Coulomb, J.L. and Brissoneau, P., (1987), "A survey of the main aspects of magnetic forces and mechanical behaviour of ferromagnetic materials under magnetization", IEEE Transaction on Magnetics, Vol. 23, (5), pp. 3765-3767.

[5.4] Campbell, P., (1994), 'Permanent Magnet Materials and Their Application', Cambridge University Press, Cambridge.

[5.5] Park, R.J. and Studders, R.J., (1962), 'Permanent Magnets and Their Application', John Wily and Sons, Inc., New York.

[5.6] Fouad, F.A., Nehl, T.W. and Demerdash, N.A., (1981), "Permanent magnet modeling for use in vector potential finite element analysis in electrical machinery", IEEE Transaction on Magnetics, MAG-17, pp3002-3004.

[5.7]   Demerdash, N.A, (1991), '*Permanent magnets and machines*', Workshop on

Finite Elements in Electromagnetics, Rensselaer Polytechnic Institute.

[5.8]   Chari, M.V.K. and Silvester, P., (1971), "Analysis of turbo-alternator

magnetic fields by finite elements", IEEE Trans. PSP, PAS-90, pp454-464.

[5.9]   Knoepfel, H., (1970), '*Pulse High Magnetic Field*', North-Holland,

Amsterdam.

[5.10] Sykulski, J.K., (1995), '*Computational Magnetics*', Chapman & Hall,

London.

[5.11] Chen, J.Y., Nayar, C.V. and Xu, L., (1998), "Design of A Outer-Rotor,

Direct-Coupled Wind Generator for Wind Energy Conversion", 1998 IEEE

Industry Applications Society Conference (The 33rd Annual Meeting), St.

Louis, USA, October 11-15, pp387-394.

[5.12] Chen, J.Y. and Nayar, C.V., (1998), "Determination of Parameters and

Evaluation of Performance of An Outer-Rotor Permanent Magnet Generator

for Wind Energy Application", IEEE International Conference on Power

Electronics Drives and Energy Systems for Industrial Growth, Perth,

Australia, December, pp353-358.

[5.13] Salon, S.J., and D'Angelo, J., (1988), "Applications of the hybrid finite element – boundary element method in electromagnetics", IEEE Transaction on Magnetics, MAG-24, (1), pp80-85.

[5.14] Hayt, Jr. W.H., (1989), "Engineering Electromagnetics", McGraw-Hill, Inc., New York.

[5.15] Ferrari, R.L. and Pinchuk, A.R., (1985), "Complementary variational finite element solution of eddy current problems using field variables", IEEE Trans. on Magnetics, vol. 21, (6), pp. 2242-2245.

[5.16] Fairweather, G., (1978), '*Finite element Galerkin methods for differential equations*', M. Dekker Inc., New York.

[5.17] Silvester, P.R. and Ferrari, R.L., (1990), '*Finite element for electrical engineers*', 2nd Ed., Cambridge University Press, Cambridge.

[5.18] Hoole, S.R.H., (1989), '*Computer-aided analysis and design of electromagnetic devices*', Elsevier.

[5.19] ANSYS Electromagnetic Field Analysis Guide, 000859, 2nd Edition, SAS IP, Inc., USA.

[5.20] Zienkiewicz, O.C. and Taylor, R.L., (1994), '*The finite element method*', 4th edition', Vol. I, Basic formulations and linear problems, McGraw-Hill, London.

Appendix V-1

Shape Function and Integral in Area Coordinates

Surface integrals are frequently evaluated in terms of area coordinates in the finite element analysis.

Fig. A5.1.1 shows a triangle divided into three distinct areas with vertices i, j k and P. The position of a point in a triangular element can be determined not only by the Cartesian coordinate (x, y) but also by area coordinates $(\zeta_i, \zeta_j, \zeta_k)$. The ζ_i, ζ_j and ζ_k are defined as:

$$\zeta_i = \frac{\Delta_i}{\Delta}, \zeta_j = \frac{\Delta_j}{\Delta}, \zeta_k = \frac{\Delta_k}{\Delta} \qquad (A5.1.1)$$
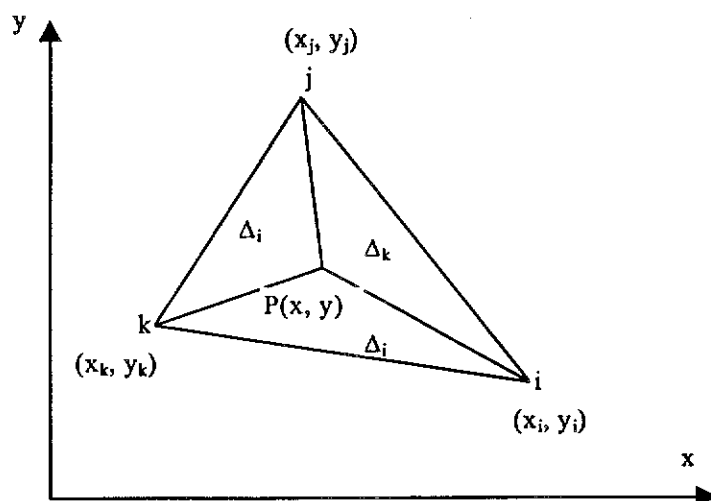
Fig. A5.1.1 Subdivisions of triangle

where area of triangle

226

$$\Delta_i = \frac{1}{2} \begin{vmatrix} 1 & x & y \\ 1 & x_j & y_j \\ 1 & x_k & y_k \end{vmatrix}$$

$$= \frac{1}{2}[(x_j y_k - x_k y_j) + (y_j - y_k)x + (x_k - x_j)y] \qquad (A5.1.2)$$

$$= \frac{1}{2}(a_i + b_i x + c_i y)$$

Similarly,

$$\Delta_j = \frac{1}{2} \begin{vmatrix} 1 & x_i & y_i \\ 1 & x & y \\ 1 & x_k & y_k \end{vmatrix}$$

$$= \frac{1}{2}[(x_k y_i - x_i y_k) + (y_k - y_i)x + (x_i - x_k)y] \qquad (A5.1.3)$$

$$= \frac{1}{2}(a_j + b_j x + c_j y)$$

and

$$\Delta_k = \frac{1}{2} \begin{vmatrix} 1 & x_i & y_i \\ 1 & x_j & y_j \\ 1 & x & y \end{vmatrix}$$

$$= \frac{1}{2}[(x_i y_j - x_j y_i) + (y_i - y_j)x + (x_j - x_i)y] \qquad (A5.1.4)$$

$$= \frac{1}{2}(a_k + b_k x + c_k y)$$

so that

$$\Delta = \Delta_i + \Delta_j + \Delta_k = \frac{1}{2}\begin{vmatrix} 1 & x_i & y_i \\ 1 & x_j & y_j \\ 1 & x_k & y_k \end{vmatrix} \tag{A5.1.5}$$

$$= \frac{1}{2}(x_i y_j + x_j y_k + x_k y_i - x_j y_i - x_k y_j - x_i y_k)$$

The magnitude of these area coordinates varies from zero at the sides to a maximum of unity at the opposite triangle vertices along the altitudes, and they satisfy the relation

$$\zeta_i + \zeta_j + \zeta_k = 1 \tag{A5.1.6}$$

Therefore, there are only two independent variables among the three and the third one is dependent.

Substituting equation (A5.1.2~5) into equation (A5.1.1), obtain

$$\zeta_i = \frac{a_i + b_i x + c_i y}{2\Delta}$$

$$\zeta_j = \frac{a_j + b_j x + c_j y}{2\Delta} \tag{A5.1.7}$$

$$\zeta_k = \frac{a_k + b_k x + c_k y}{2\Delta}$$

It is seen that area coordinates are linear function of Cartesian coordinates. Reversibly, Cartesian coordinates can be expressed in area coordinates

$$x = \zeta_i x_i + \zeta_j x_j + \zeta_k x_k$$

$$y = \zeta_i y_i + \zeta_j y_j + \zeta_k y_k \tag{A5.1.8}$$

Now, it needs to find out the relation of integration between the two coordinates.

Given a surface integral

$$\iint_{\Delta c} F(x,y)\,dxdy \qquad\qquad (A5.1.9)$$

Transforming the integrand into area coordinates

$$\iint_{\Delta c} F(\zeta_i,\zeta_j,\zeta_k)\,dxdy \qquad\qquad (A5.1.10)$$

As there are only two independent variables the third one can be expressed by the independent two. The integration is further changed into

$$\iint_{\Delta c} F(\zeta_i,\zeta_j,1-\zeta_i-\zeta_j)\,dxdy \qquad\qquad (A5.1.11)$$

The relation between $dxdy$ and $d\zeta_i d\zeta_j$ is

$$d\zeta_i d\zeta_j = \begin{vmatrix} \dfrac{\partial \zeta_i}{\partial x} & \dfrac{\partial \zeta_i}{\partial y} \\[2mm] \dfrac{\partial \zeta_j}{\partial x} & \dfrac{\partial \zeta_j}{\partial y} \end{vmatrix} dxdy \qquad\qquad (A5.1.12)$$

From equation (A5.1.7) the derivatives are

$$\frac{\partial \zeta_i}{\partial x} = \frac{b_i}{2\Delta};\ \frac{\partial \zeta_i}{\partial y} = \frac{c_i}{2\Delta};\ \frac{\partial \zeta_j}{\partial x} = \frac{b_j}{2\Delta};\ \frac{\zeta_j}{\partial y} = \frac{c_j}{2\Delta} \qquad\qquad (A5.1.13)$$

Substituting into equation (A5.1.12)

$$d\zeta_i d\zeta_j = \begin{vmatrix} \dfrac{\partial \zeta_i}{\partial x} & \dfrac{\partial \zeta_i}{\partial y} \\[2mm] \dfrac{\partial \zeta_j}{\partial x} & \dfrac{\partial \zeta_j}{\partial y} \end{vmatrix} dxdy = \frac{b_i c_j - b_j c_i}{(2\Delta)^2} dxdy = \frac{dxdy}{2\Delta} \qquad (A5.1.14)$$

So that

$$dxdy = 2\Delta d\zeta_i d\zeta_j \qquad (A5.1.15)$$

Since the two coordinate are linearly dependent the integral domain is still a triangle when it is transformed from Cartesian coordinates. The three vertices turn into (1,0), (0,1) and (0,0) from (x_i, y_i), (x_j, y_j) and (x_k, y_k), as shown in Fig.A5.1.2. Any of the points within one triangle has its corresponding point in the other. So, the surface integral becomes

$$\iint_{\Delta_c} F(\zeta_i, \zeta_j, 1 - \zeta_i - \zeta_j) dxdy$$
$$= \iint_{\Delta_a} F(\zeta_i, \zeta_j, 1 - \zeta_i - \zeta_j) d\zeta_i d\zeta_j \qquad (A5.1.16)$$
$$= 2\Delta \int_0^1 d\zeta_i \int_0^{1-\Omega_i} F(\zeta_i, \zeta_j, 1 - \zeta_i - \zeta_j) d\zeta_j$$

Suppose the integrand is a power function. Generally, it can have such specified form below,

$$F(\zeta_i, \zeta_j, 1 - \zeta_i - \zeta_j) = \zeta_i^a \zeta_j^b \zeta_k^c = \zeta_i^a \zeta_j^b (1 - \zeta_i - \zeta_j)^c \qquad (A5.1.17)$$

where a, b and c are positive integers.
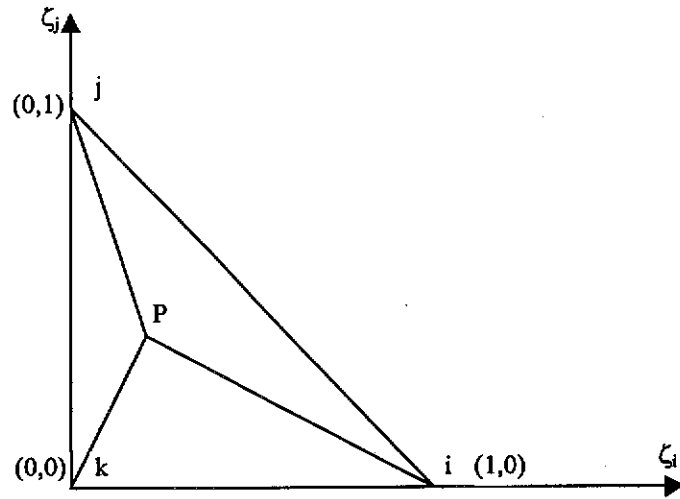
Fig. A5.1.2   Triangle in area coordinate

Then, the equation (A5.1.16) can be re-written as

$$2\Delta \int_0^1 [\int_0^{1-\zeta_i} \zeta_i{}^a \zeta_j{}^b (1-\zeta_i-\zeta_j)^c \, d\zeta_j] d\zeta_i \tag{A5.1.18}$$

Using the transformation, $v = \dfrac{\zeta_j}{1-\zeta_j}$; $dv = \dfrac{d\zeta_j}{1-\zeta_j}$, equation (A5.1.18) becomes

$$2\Delta \int_0^1 [\zeta_i{}^a (1-\zeta_i)^{b+c+1} \int_0^1 v^b (1-v)^c \, dv] d\zeta_i \tag{A5.1.19}$$

Applying Euler's integral formula

231

$$\int_0^1 s^m (1-s)^n \, ds = \frac{m! n!}{(m+n+1)!}$$

(A5.1.20)

The integral of equation (A5.1.19) becomes

$$2\Delta \int_0^1 [\zeta_i^a (1-\zeta_i)^{b+c+1} \frac{b! c!}{(b+c+1)!}] d\zeta_i$$

$$= 2\Delta \frac{a!(b+c+1)!}{[a+(b+c+1)+1]!} \cdot \frac{b! c!}{(b+c+1)!}$$

(A5.1.21)

$$= 2\Delta \frac{a! b! c!}{(a+b+c+2)!}$$

So that

$$\iint_{A_c} \zeta_i^a \zeta_j^b \zeta_k^c \, dxdy = 2\Delta \frac{a! b! c!}{(a+b+c+2)!}$$

(A5.1.22)

As an example of integral in area coordinates, the surface integral of equation (5.22) is re-evaluated as below,

232

$$\iint_{\Omega_e} W^e J_z^e \, dx \, dy$$

$$= \iint_{\Omega_e} \begin{pmatrix} S_i^e \\ S_j^e \\ S_k^e \end{pmatrix} J_z^e \, dx \, dy$$

$$= J_z^e \iint_{\Omega_e} \begin{pmatrix} \dfrac{a_i + b_i x + c_i y}{2\Delta} \\ \dfrac{a_j + b_j x + c_j y}{2\Delta} \\ \dfrac{a_k + b_k x + c_k y}{2\Delta} \end{pmatrix} dx \, dy$$

$$= J_z^e \iint_{\Omega_e} \begin{pmatrix} \zeta_i \\ \zeta_j \\ \zeta_k \end{pmatrix} dx \, dy$$

$$= J_z^e \begin{pmatrix} \dfrac{2\Delta}{3!} \\ \dfrac{2\Delta}{3!} \\ \dfrac{2\Delta}{3!} \end{pmatrix}$$

$$= \frac{J_z^e \Delta}{3} \begin{pmatrix} 1 \\ 1 \\ 1 \end{pmatrix}$$

(A5.1.23)

This result is the same as the one obtained from equation (5.22).

Appendix V-2

Green's Theorem in 2-D Cartesian Coordinates

Let R be an admissible region of the xy-plane with boundary C, and let $P(x,y)$ and $Q(x,y)$ have continuous first partial derivatives in an open region containing R. Then,

$$\oint_C Pdx + Qdy = \iint_R (\frac{\partial Q}{\partial x} - \frac{\partial P}{\partial y})dxdy \tag{A5.2.1}$$

where the direction around C is chosen so that R is on the left as C is traversed.

Take equation (5.2.2b) as an example. Let

$$P = v\frac{\partial A}{\partial x}W$$
$$Q = v\frac{\partial A}{\partial y}W \tag{A5.2.2}$$

Substitute into the right hand of equation (A5.2.1),

$$\iint_R (\frac{\partial Q}{\partial x} - \frac{\partial P}{\partial y})dxdy$$
$$= \iint_R [\frac{\partial}{\partial x}(v\frac{\partial A}{\partial x}) + \frac{\partial}{\partial y}(v\frac{\partial A}{\partial y})]Wdxdy + \iint_R v(\frac{\partial A}{\partial x}\frac{\partial W}{\partial x} + \frac{\partial A}{\partial y}\frac{\partial W}{\partial y})dxdy \tag{A5.2.3}$$

The left hand of equation (A5.2.1) becomes

$$\oint_L P dx + Q dy$$

$$= \oint_s [v \frac{\partial A}{\partial x} W \cos(\hat{n,x}) + v \frac{\partial A}{\partial y} W \cos(\hat{n,y})] ds \qquad (A5.2.4)$$

$$= \oint_s v \frac{\partial A}{\partial n} W ds$$

where $\cos(\hat{n,x})$ and $\cos(\hat{n,y})$ are the direction cosine of x and y components respectively. Combining equation (A5.2.3) and (A5.2.4), gives

$$-\iint_\Omega W[\frac{\partial}{\partial x}(v \frac{\partial A}{\partial x}) + \frac{\partial}{\partial y}(v \frac{\partial A}{\partial y})] dx dy$$

$$= \iint_\Omega v[(\frac{\partial W}{\partial x} \frac{\partial A}{\partial x}) + (\frac{\partial W}{\partial y} \frac{\partial A}{\partial y})] dx dy - \oint_s v W \frac{\partial A}{\partial n} ds \qquad (A5.2.5)$$

This is the result of equation (5.2.3).

Appendix V-3

Stoke's Theorem in Vector Field

Starting with Maxwell's equation in differential form,

$$\nabla \times H = J \qquad\qquad (A5.3.1)$$

Consider the surface S of Fig. A5.3.1, which is broken up into incremental surfaces of area ΔS. Apply the definition of the curl in equation (A5.3.1) to one of those incremental surfaces, then
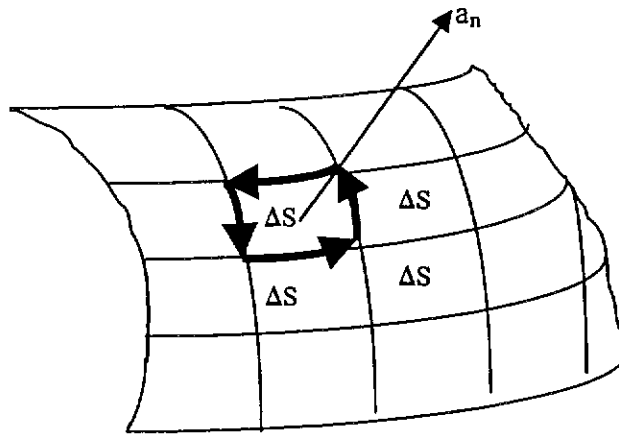
Fig. A5.3.1   Surface S

$$\frac{\oint H \cdot dL_{\Delta S}}{\Delta S} \doteq (\nabla \times H)_n \qquad\qquad (A5.3.2)$$

where the n subscript indicates the right-hand normal to the surface. The subscript on $dL_{\Delta S}$ indicates that the closed path is the perimeter of an incremental area ΔS. This result can be written as

236

$$\frac{\oint H \cdot dL_{\Delta S}}{\Delta S} \doteq (\nabla \times H) \cdot a_n \qquad (A5.3.3)$$

or

$$\frac{\oint H \cdot dL_{\Delta S}}{\Delta S} \doteq (\nabla \times H) \cdot a_n \Delta S = (\nabla \times H) \cdot \Delta S \qquad (A5.3.4)$$

where a_n is a unit vector in the direction of the right-hand normal to ΔS.

Now, determine this circulation for every ΔS comprising S and sum the results. When evaluating the closed line integral for each ΔS, some cancellation will occur because every *interior* wall is covered one in each direction. The only boundaries on which cancellation cannot occur from the outside boundary, the path enclosing S. It gives

$$\oint H \cdot dL \equiv \int_S (\nabla \times H) \cdot dS \qquad (A5.3.5)$$

where dL is taken only on the perimeter of S.

Equation (A5.3.5) is known as **Stoke's Theorem** that is an identity, holding for any vector field.

CHAPTER SIX

CONCLUSIONS

The worldwide energy shortage has made a significant impact on the design and application of electrical machines. Sustainable energy solutions are aimed to reduce the consumption of fossil fuels by using energy efficiency techniques and renewable energy sources. This thesis presents two new sustainable energy applications in the field of electrical machines.

Polyphase induction motors dominate the energy usage spectrum for industrial and commercial applications. The conventional winding structure used in three-phase AC electrical machines has a basic unit of the winding with a 60° phase belt and a three-phase connection either in star or delta. A new winding structure using an innovative Star-Delta Series Connection (SDSC) which has a high winding coefficient and low harmonic content is presented in this thesis. The principle of the SDSC winding is described through two detailed cases. The Electro-Magnetic Belt and Electro-Magnetic Space diagrams are two important means used for optimization of the new winding. Experimental results from the two prototypes confirm the theoretical analysis. The efficiency of the new machine at rated load increased by about 3.8% as compared to its counterpart with a conventional winding structure.

Wind energy shows a prospective future in renewable energy options. Wind turbines are designed to couple either synchronous or asynchronous generators with various forms of direct or indirect connection with grid or diesel generators. Permanent

magnet (PM) generators using high energy permanent magnets (PM) offer advantages such as direct coupling without gear box, absence of excitation winding and slip rings, light weight and smaller size. This thesis presents the design and development of an outer-rotor PM generator using Neodymium- Iron-Boron magnets for wind turbine application. The method with direct electromagnetic design followed by a Finite Element Analysis is proofed applicable to the design of this type of machine. A 20 kW prototype machine was built and extensively tested. It was found that the machine could maintain an efficiency of about 85% over a wide load-operating range. Equivalent circuit models were developed. The results of the Finite Element analysis matches closely with the experimental and the designed values.

The conclusions and contributions are drawn from this thesis are summarized as follows:

6.1 The SDSC Winding Induction Motor

(1)   A conventional 60°-spread winding operating from a standard three-phase supply can be turned into a quasi-12-phase winding by the mean of star-delta series connection. A higher spread factor is achieved through the increase of the effective number of phases. This has been verified by the theoretical analysis and experimental results in Chapter Three. The main advantages from this configuration are:

(i)   Although it is required that the delta component should contain $\sqrt{3}$ times as many effective turns per phase as the star component, a slight

difference is allowed in practice because of discretization of commercial wire sizes. This does not cause any significant problem in the new winding machines.

(ii)   The possibility for circulating currents between the star and delta components which is easy to occur in parallel connection can thus be completely prevented.

(2)   The Electromagnetic Space (EMS) diagram plays an important role in the design of the new winding. The arrangement of the 3-phase winding and connection of coils can be directly derived from this diagram. The requirement of phase displacement between star and delta components and the three-phase windings can be met on the EMS diagram.

(3)   Flexible selection of the Electromagnetic Belt (EMB) is one of the features of the new winding. A higher fundamental spread factor can be obtained by optimizing the EMB. Generally, there are three basic rules to be followed in the selection of EMB:

(i)   To obtain a high spread factor, a narrower EMB is preferred. But, an overall affection should be taken into account for the machine performance;

(ii)   The total peripheral electrical angle must be three times the EMB so that the total number of EMB can be evenly distributed in between the three phases, namely $\dfrac{p \times 180^{o}}{EMB} = 3k$ (k=1, 2, 3, …);

(iii)   Once all of the EMBs are put together to make up a complete three-phase winding, there should be a displacement of 30° electrical angle between the star and delta components per phase.

(4)   The new winding can be made as a single layer and technological short-pitch. It is easy to determine the slot combination. Thus, the utilization coefficient of slot area is increased and coils may have a shorter mean length. The chord factor is always equal to unity by employing full-pitch coils.

(5)   Theoretical analysis showed that the amplitude of fundamental MMF of the new winding motor has been increased by more than 3%, compared to its conventional counterpart. Other higher order harmonic MMFs have been considerably reduced, particularly those that usually produce braking torque to motor starting and operation such as 5th, 7th, 11th and 13th.

(6)   The new winding motor can operate with higher efficiency for a wide load range. Also, it has a higher maximum-torque and starting-torque than a standard motor. This has been verified by experimental results in Chapter Three.

(7)   Different benefits can be achieved by adjusting the design scheme of the new winding motor, depending upon the requirement. The motor can either raise the efficiency without reducing the power factor, or save appropriate raw materials while maintaining the original performance.

(8)   The new winding may be made in two different types; one is a non uniform-constitution and the other a uniform-constitution. Both are applicable for mass production of motors. The uniform-constitution consists of two different coils and the end connections are slightly complex than conventional one.

(9)   The test results show that this new winding motor does not cause any overheating problem at normal operating condition although the circulating current is inversely proportional to number of turns in the delta winding, which is only a fraction of the whole winding. However, caution should be paid to no-load operation at excessive voltage.

(10)   The new winding can be applied not only on the induction machines but also on the synchronous machines where the neutral is not necessary such as synchronous motors and generators used for battery-charging in a stand-alone power system.

Both theoretical and experimental results proofed that the new SDSC winding motors had a higher efficiency and a lower harmonics than the motors with a conventional winding structure. This mainly due to the techniques employed in the design. Since the new winding motor can reduce considerable consumed power from the integral

grid every year and more than 90% of the motors used in industry are induction motor and synchronous motor, the new winding can find a widely potential application in industry.

6.2 The Outer-Rotor, Permanent-Magnet Generator

(a) Wind turbines are low speed (typically between 30 – 300 rpm) prime movers in wind energy conversion systems. To achieve the normal frequency output the low-speed generator needs either a gearbox or should mount with a large number of poles. Because of the enlarged periphery of the out-rotor drum, the multi-pole structure presented in this thesis can be easily accommodated.

(b) The wind turbine blades are directly coupled to the front face of the outer-rotor. This arrangement avoids use of a gearbox, which is very heavy and noisy. With greatly reduced weight, the direct-coupled permanent-magnet generator can be conveniently transported and installed in remote areas.

(c) All of the permanent magnets are squarely shaped and evenly placed to the inner periphery of the rotor drum. While the generator is running, the centrifugal force of the magnets applies a pressure to the bonding media. Thus, the reliability of the glued joints becomes higher. As exposed to the natural wind flow, the outer-rotor has a much-reduced temperature rise than the stator.

(c)   Being excited by permanent magnet the wind turbine generator is free of DC excitation windings and field circuits losses.

(d)   Experimental results confirmed that a permanent magnets generator made in such a simple construction could operate with good and reliable performance over a wide range of speeds. The simple mechanism of the generator leads to a low manufacture cost in factory and low maintaining cost.

(e)   Satisfactory results were obtained by using a direct design program for initial iteration and the finite element method for detailed analysis and final adjustment. The good agreement between the theoretically predicted and experimentally tested results further proves the correctness of the design principles and the effectiveness of the design methodology.

(f)   It was found that discrepancies occurred between computed and measured values of terminal voltages at higher frequency and over load condition. Ignoring the error yielded by testing system such as inductive component of load resistor, and phase imbalance of load and input voltages, etc., the discrepancies are due to the following:

     i)   Magnetic conditions varied with a more complex function of resultant total flux in the generator rather than only q-axis saturation.

     ii)   The variation of d-axis synchronous reactance X_d and q-axis synchronous reactance X_q is the function of load current and rotating speed.

iii)   Stator winding resistance varies with temperature or load current. But a
        constant resistance was used in computation.

(g)   To achieve a convergent solution, finite element method is presented in the
        process that contains deriving the true energy functional for problem
        condition and transforming the domain of continuum problem into a number
        of discrete triangular elements. These elements represent the geometry, own
        the material characteristics of the medium and define the approximation to the
        magnetic field in the region. The required field solution is obtained by
        minimizing the energy functional through a set of approximate functions.

(h)   Although the direct advantage of the variational formulation is that the energy
        functional related to the physical concept of energy, the approach has its
        weakness that for every equation to be solved a functional needs to be
        identified at its minimum to satisfy the differential equation being solved. It
        needs to yield symmetric matrices for the Poisson's equation with the term
        $\nabla^2 A$. At least a second order polynomial trial function for the unknown f is
        required to ensure that the second derivative of the functional shall not
        vanish. This is not always a convenient way. This difficulty can be overcome
        by the Galerkin approach adopted in finite element analysis of this thesis.

(i)   Newton-Raphson method has been adopted to deal with the non-linear
        problems of electromagnetic field where magnetic permeability is a function
        of the local magnetic field. Although the designed generator has a different
        construction from normal synchronous machines, it is reasonable to use a

standard method of mesh generation to produce triangular elements within the domain. As an adaptive mesh generator, the mesh refinements were weighted toward the region of high flux density, varying with the vector-potential, distributed elements.

(j)   The terminal voltages of the generator evaluated at no-load and load conditions are derived by calculating flux linkages and their products with angular velocity. The Maxwell Stress Tensor method is used for computing forces. The simulation of the electromagnetic torque and power capability are given following the computation of the globe forces. The load test of the prototype machine shows a very close result with the simulation.

(k)   Periodicity condition for rotating electrical machinery has been used in the finite element method so that a much smaller area, a section of 2-pole, is analyzed rather than the entire region of 48-pole. This saves the computer space and accelerates the computation speed.

As a non-pollution, and cheap energy source, wind energy has a large distribution around world. It is seen that the out-rotor permanent generator presented in this thesis can effectively convert wind energy to electrical energy in a stand-alone power system and make a significant dedication to energy savings.

BIBLIOGRAPHY

To solve the problems addressed in this thesis, the author has referred a very large volume of literature on the theory of electrical machines and permanent magnet machines, applications of three-phase winding, wind energy and finite element method. These academic papers and books have directly or indirectly been responsible for presenting different viewpoints on matters discussed. The author would not be able to conduct his research without mention the following references which were studied for their perceptive approach.

Bousbaine, A., Low, W.F. and McCormick, M., (1996), "Novel approach to the measurement of iron and stray load losses in induction motors", IEE Proc.-Electr. Power Appl., **143**, (1), pp. 78-86.

Chidambaram, P., Achutha Kamath, A., Subbiah, M. and Krishnamurthy, M.R., (1983), "A new pole-changing winding using star/star-delta switching", IEE Proc.-B, **130**, (2), pp. 130-136.

Eastham, J.F., and Balchin, M.J., (1975), "Pole-change windings for linear induction motors", Proc. IEE, **122**, (2), pp. 154-160.

Rajaraman, K.C., (1978), "New 2-speed induction motor", Proc. IEE, **125**, (10), pp. 957-958.

Rajaraman, K.C., (1970), "Pole-changing motor using π-speed phase windings", Proc. IEE, **117**, (5), pp. 957-960.

Rajaraman, K.C., (1977), "Design criteria for pole-changing windings", Proc. IEE, **124**, (9), pp. 775-783.

Grant, D., (1983), "Design of phase-change 2-speed windings for induction motors, using pole-amplitude modulation techniques", IEE Proc.-B, **130**, (1), pp. 45-50.

Williamson, S., and Laithwaite, E.R., (1985), "Generalised harmonic analysis for the steady-state performance of sinusoidally-excited cage induction motors", IEE Proc.-B, **132**, (3), pp. 157-163.

Williamson, S., and Smith, A.C., (1980), "Field analysis for rotating induction machines and its relationship to the equivalent-circuit method", IEE Proc.-B, **127**, (2), pp. 83-89.

Bird, B.M. and Ridge, J., (1971), "Induction-motor speed-control schemes employing stator-voltage variation and pole-change windings", Proc. IEE, **118**, (3/4), pp. 537-542.

Rajaraman, K.C. and Betigeri, K.G., (1982), "Optimum design of 1:2 pole changing motor", IEE Proc.-B, **129**, (3), pp. 151-158.

Rawcliffe, G.H. and Fong, W., (1970), "'Sum' and 'difference' winding modulation with special reference to the design of 4/6-pole p.a.m. windings", Proc. IEE, **117**, (9), pp. 1782-1792.

Binns, K.J. and Rowlands-Rees, G., (1978), "Radial tooth-ripple forces in induction motor due to the main flux", Proc. IEE, **125**, (11), pp. 1227-1231.

Lees, M.J. and Tindall, C.E., (1974), "Field-theory analysis of saturation harmonics in induction machines", Proc. IEE, **121**, (4), pp. 276-280.

Tindall, C.E and Lees, M.J., (1973), "Field-theory to induction motor analysis", Proc. IEE, **120**, (4), pp. 469-476.

Butler, O.I. and Mohammed, M.Z., (1971), "Change of stray loss of a cage induction motor with axial variation of the interbar resistance", Proc. IEE, **118**, (7), pp. 884-886.

Laithwaite, E.R. and Kuznetsov, S.B., (1982), "Cage-rotor induction motor with unity power factor", IEE Proc.-B, **129**, (3), pp. 143-150.

Fulton, N.N., Slater, R.D. and Wood, W.S., (1976), "Design optimisation of 3-phase induction motor", Proc. IEE, **123**, (2), pp. 141-144.

Marimuthu, P. and Krishnamurthy, M.R., (1975), "Experimental study of pole-changing series motor", Proc. IEE, **122**, (6), pp. 650-651.

Binns,K.J. and Kahan,P.A., (1981), "Effect of load on the tangential-force pulsations and harmonic torques of squirrel-cage induction motor", IEE Proc.-B, **128**, (4), pp. 207-211.

Broadway, A.R.W., (1971), "Cagless induction machine", Proc. IEE, **118**, (11), pp. 650-651.

Eastham, J.F. and Williamson, S., (1973), "Generalised theory of induction motors with asymmetrical airgap and primary windings", Proc. IEE, **120**, (7), pp. 767-774.

G. Qishan, and H. Shuhong., (1994), "Analytic approach to magnetic circuit for saturated axial-field induction machines", IEE Proc.-Electr. Power Appl., **141**, (1), pp. 27-32.

Alwash, J.H.H., (1996), "Predicting performance of three-phase induction motors connected to single-phase supplies", IEE Proc.-Electr. Power Appl., **143**,(4), pp. 339-344.

Singh C. and Sarkar D., (1992), "Practical considerations in the optimisation of induction motor design", IEE Proc.-B, 139, (4), pp. 365-373.

Williamson, S. and McClay, C.I., (1997), "The effect of Axial variations in saturation due to skew on induction motor equivalent-circuit parameters", IEEE Industry Application Society Annual Meeting, New Orleans, Louisiana, Oct. Vol. 1, pp120-127.

Stankovic', A., Benedict E.R., John, V. and Lipo, T.A., (1997), "A novel method for measuring induction machine magnetizing inductance", IEEE Industry Application Society Annual Meeting, New Orleans, Louisiana, Oct. Vol. 1, pp234-238.

Chalmers, B.J. and Musaba, L., (1997), "Design and field-weakening performance of a synchronous reluctance motor with axially-laminatted rotor", IEEE Industry Application Society Annual Meeting, New Orleans, Louisiana, Oct. Vol. 1, pp271-278.

Chan, Wei-Mina and Weldon, W.F., (1997), "Development of a simple nonlinear switched reluctance motor model using measured flux linkage data and curve fit", IEEE Industry Application Society Annual Meeting, New Orleans, Louisiana, Oct., Vol. 1, pp318-325.

Robinson R.B., (1962), "Harmonics in a.c. rotating machines", Proc. of IEE, Vol.109, No.16, February, pp.380-387.

Ishizaki A., Liang G. and Saitoh, K., (1990), "Quantitative study on harmonic flux density of squirrel-cage induction motor", IEEE transactions on Magnetics, , vol.26, No.2, pp.956-959.

Burbidge, R. F. (1958), "A rapid analysing the m.m.f. wave of a single or polyphase winding", Proc. IEE., 105C, pp. 307-311.

Fong, W., (1968), "Polyphase symmetrisation. A new method for the design of electrical-machine winding", Proc. IEE., ibid, 115, pp. 1123-1134.

Rawcliffe, G.H. and Fong, W., (1965), "two-speed induction motors using fractional-slot windings", Proc. IEE., ibid, 112, pp. 1899-1913.

Williams, F.C. Eastham, J.I. and Piggott, L.S., (1964), "Analysis and designs of pole-changing motors using phase mixing techniques ", Proc. IEE., ibid, 111, (1), pp. 80-94.

Lawrenson, P.J. and Ralph, M.C., (1966), "Tooth-ripple losses in solid poles", ibid, 113, (4), pp. 657-662.

Ostovic, V., (1989), 'Dynamics of saturated electric machines', Springer-Verlag, New York.

Still, A. and Siskind, C.S., (1954), 'Element of electrical machine design', McGraw-Hill Book Company, Inc., New York.

Piggot, L.S., (1962), "A theory of the operation of cylindrical induction motors with squirrel-cage rotors", ibid., 109C, pp. 270-282.

Binns, J.J., Hindmarsh, R. and Short, P.B., (1971), "Effect of skewing slots on flux distribution in induction machines", Proc. IEE, 118, (3/4), pp. 543-549.

Cullen, A.L. and Barton, T.H., (1958), "A simplified electromagnetic theory of the induction motor, using the concept of wave impedance", ibid., 105C, pp. 331-336.

Ramarao, N. and Jyoti, Rao, P.A.D., (1968), "Rerating factors of polyphase induction motor under unbalanced line voltage condition", IEEE Trans., 87, pp. 240-249.

Hindmarsh, J., (1989), 'Electrical machines and drives worked examples', Pergamon Press, UK.

Chalmers, B.J. and Harain, C.K., (1970), "High-frequency no-load losses of cage induction motors", IEEE Trans. on Power Apparatus and Systems, Vol. PAS-89, July-August, pp. 1043-1049.

Freeman, E.M., (1962), "The calculation of harmonics, due to slotting, in the flux density waveform of a dynamo-electric machine", Proc. IEE, Vol. 109, September, pp. 581-588.

Karmaker, H.C., (1992), "Stray losses in large synchronous machine", IEEE Trans. on Energy Conversion, Vol. 7, No. 1, pp. 148-153.

Schwarz, K.K., (1964), "Survey of basic stray load losses in squirrel cage induction motors", Proc. IEE, Vol. 111, pp. 1565-1573.

Cistelecan, M., and Onica, P., (1976), "New improvements in the computation of the polyphase induction-motor magnetic circuit", Proc. IEE, Vol. 123, (4), April, pp. 335-340.

Neto. L.M., Camacho, J.R., Salerno C.H. and Alvarenga, B.P., (1999), "Analysis of a three-phase induction machine including time and space harmonic effects: the A, B, C reference frame", IEEE Trans. on Energy Conversion, Vol. 14, No. 1, March, pp. 80-85.

Jimoh, A.A. Findlay, R.D. and Poloudjadouff, M., (1985), "Stray load losses in induction machines. Part 1: definition, origin and measurement. Part 2: calculation and reduction", IEEE Trans., PAS-104, pp. 1500-1512.

Ishizaki, A., Liang, G. and Saitoh, K., (1992), "Quantitative study on harmonic flux densities of squirrel-cage induction motors", IEEE Trans. on Magnetics, Vol. 26, No. 2, pp. 956-959.

Singh, C. and Sarkar, D., (1992), "Practical consideration in the optimisation of induction motor design", IEE Proc.-B, Vol. 139, (4), July, pp. 365-373.

Sawhney, A.K., (1992), 'A course in electrical machine design', Dhanpat Rai & Sons, Inc., Delhi.

Freris, L.L., (1989), 'Wind energy conversion systems', Prentice Hall Ltd., UK.

Westlake, A.J.G., Bumby, J.R. and Spooner E., (1996), "Damping the power-angle oscillations of a permanent-magnet synchronous generator with particular reference to wind turbine applications", IEE Proc.-Electr. Power Appl., Vol. 143, (3), May, pp. 269-280.

Wasynczuk, O., Man, D.T. and Sullivan, J.P., (1981), "Dynamic behaviour of a class of wind turbine generator during random wind fluctuations", IEEE Trans., PAS-100, pp. 2837-2845.

Binns, K.J., and Kurdali, A., (1979), "Permanent-magnet a.c. generator", Proc. IEE, Vol. 126, (7), July, pp. 690-696.

Bonwick, W.J., and Jones, V.H., (1972), "Performance of a synchronous generator with a bridge rectifier", Proc. IEE, Vol. 119, (9), July, September, pp. 1338-1342.

Spooner, E., Williamson, A.C. and Catto, G., (1996), "Modular design of permanent-magnet generators for wind turbines", IEE Proc.-Electr. Power Appl., Vol. 143, (5), September, pp. 388-395.

Chalmers, B.J., Wu, W., and Spooners, E., (1999), "An axial-flux permanent-magnet generator for a gearless wind energy system", IEEE Trans. on Energy Conversion, Vol. 14, No. 2, June, pp. 251-257.

Bonanno, F., Consoli, A., Racti, A., Morgana, B. and Nocera, U., (1999), "Transient analysis of integrated diesel-wind-photovoltaic generation systems", IEEE Trans.on Energy Conversion, Vol. 14, No. 2, June, pp. 232-238.

Wang, L. and Lee H., (1997), "A novel analysis on the performance of an isolated self-excited induction generator", IEEE Trans. on Energy Conversion, Vol. 12, No. 2, June, pp. 109-117.

Binns, K.J., and Low, T.S., (1983), "Performance and application of multi-stacked imbricated permanent magnet generator", IEE Proc.-Electr. Power Appl., Vol. 130, (6), November, pp. 407-414.

Chen, Z., Spooner, E., Norris, W.T. and Williamson, A.C., (1998), "Capacitor-assisted excitation of permanent-magnet generator", IEE Proc.-Electr. Power Appl., Vol. 145, (6), November, pp. 497-508.

Chen, Z., and Spooner, E., (1998), "Modular design of permanent-magnet generators for wind turbines", IEE Proc.-Electr. Power Appl., Vol. 145, (4), July, pp. 273-283.

Kettleborough, J.G., Smith, I.R., and Fanthome, B.A., (1983), "Simulation of a dedicated aircraft generator supplying a heavy rectified load", IEE Proc.-Electr., Vol. 130, (6), Nov., pp. 431-435.

Honda, Y., Higaki, T., Morimoto, S. and Takeda, Y., (1998), "Rotor design optimisation of a multi-layer interior permanent magnet synchronous motor", IEE Proc.-Electr. Power Appl., Vol. 145, (2), March, pp. 119-124.

Craig,, L.M., Saad-Saoud, Z. and Jenkins, N., (1998), "Electrodynamic braking of wind turbines", IEE Proc.-Electr. Power Appl., Vol. 145, (2), March, pp. 140-146.

Van der Veen, J.L.F., Offringa, L.J.J. and Vandenput, A.J.A., (1997), "Minimising rotor losses in high-speed high-power permanent magnet synchronous generators with rectifier load", IEE Proc.-Electr. Power Appl., Vol. 144, (5), September, pp. 331-337.

Demerdash, N.A., Miller, R.H., Nehl, T.W., Overton, B.P. and Ford, C.J., (1983), "Comparison between features and performance characteristics of fifth Hp samarium Cobalt and Ferrite based brushless DC motors operated by same power conditioner", IEEE Trans. on PAS, PAS-102, No. 1, Jan., pp. 104-112.

Levi, E., (1997), "Modeling of magnetic saturation in smooth air-gap synchronous machines", IEEE Trans. on Energy Conversion, Vol. 12, No. 2, June, pp. 151-156.

Spooner, E., and Chalmers, B.J., (1992), "'Torus': a slotless, toroidal-stator, permanent-magnet generator", IEE Proc.-B., Vol. 139, (6), Nov., pp. 497-506.

Cho, K.-Y., Bae, J.-D., Chung, S.-K. and Youn, M.-J., (1994), "Torque harmonics minimisation in permanent magnet synchronous motor with back EMF estimation", IEE Proc.-Electr. Power Appl., Vol. 141, (6), Nov., pp. 323-330.

Shaltout, A.A. and Abdel, M.A., (1995), "Solid-state control of a wind-driven self-excited induction generator", Electric Machines and Power Systems, 23:571-582.

Caricchi, F., Cresimbini, F., Honorati, O., Lo Bianco, G. and Santini, E., (1997), "Performance of coreless-winding axial-flux permanent-magnet generator with power output at 400 Hz-3000 rev/min", IEEE IAS Annual Meeting, Louisiana, Oct., pp. 61-66.

Studer, C., Keyhani, A., Sebastian, T. and Murthy, S.K., (1997), "Study of cogging torque in permanent magnet machines", IEEE IAS Annual Meeting, Louisiana, Oct., pp. 42-49.

Campbell, P., (1974), "Principles of a permanent magnet axial-field D.C. machine", Proc. IEE, Vol. 121, (12), December, pp. 1489-1494.

Chan, C.C., (1987), "Axial-field electrical machines – design and applications", IEEE Trans. on Energy Conversion, Vol. EC-2, No. 2, June, pp. 294-300.

Mizoguchi, T., Sakai, I., Niu, H. and Pinkerton, F.E., (1986), "Nd-Fe-B-Co-Al based permanent magnets with improved magnetic properties and temperature characteristics", IEEE trans. On Magnetics., Vol. MAG-22, No.5, pp. 919-921.

Hendershot Jr., J.R. and Miller, THE, (1994), 'Design of brushless permanent-magnet motors', Magna Physics Publishing and Clarendon Press. ● Oxford, London.

De La Ree, J. and Boules, N., (1989), "Torque production in permanent-magnet synchronous motors", IEEE trans. on Industry Applications, Vol. 25, No.1, pp. 107-112.

Basak, A., (1996), 'Permanent-magnet DC linear motors', Clarendon Press ● Oxford, London.

Campbell, P., (1994), 'Permanent magnet materials and their application', Cambridge University Press, London.

Hoole, S.R.H., (1995), 'Finite elements, electromagnetics and design', ELSEVIER, Amsterdam.

Chari, M.V., (1970), 'Finite element analysis of nonlinear magnetic fields in electric machines', Phd thesis, McGill University, Montreal, Quebec.

Rahman, M.A. and Zhou, P., (1994), "Field-based analysis for permanent magnet motors", IEEE trans. on Magnetics, Vol. MAG-30, No.5, pp. 3664-3667.

Omekanda, A.M., Broche, C. and Renglet, M., (1997), "Calculation of the electromagnetic parameters of a switched reluctance motor using an improved FEM-BIEM-application to different models for the torque calculation", IEEE trans. on Industry Applications, Vol. 33, No.4, Jan./Aug., pp. 914-918.

Williamson, S., Lim, L.H. and Smith, A.C., (1990), "Transient analysis of cage-induction motors using finite-elements", IEEE trans. on Magnetics, Vol. 26, March, pp. 941-944.

Brune, C.S., Spee, R., Alexander, G.C. and Wallace, A.K., (1994), "Experimental evaluation of a variable-speed, doubly-fed wind-power generation system ", IEEE trans. on Industry Applications, Vol. 30, May/June, pp. 648-655.

Ferreira, A.C. and Williamson, S., (1999), "Time-stepping finite-element analysis of brushless doubly fed machine taking iron loss and saturation into account", IEEE trans. on Industry Applications, Vol. 35, No.3, May/June, pp. 583-588.

Hameyer, K., and Belmans, R., (1999), 'Numerical modeling and design of electrical machines and devices', WIT Press, Southampton, UK.

Hayt, Jr., W.H., (1989), 'Engineering electromagnetics', McGraw-Hill, Inc., New York.

Sykulski, J.K., (1995), 'Computational magnetics', Chapman & Hall Gmbh, London, UK.

Fouad, F.A., Nehl, T.W. and Demerdash, N.A., (1981), "Permanent magnet modeling for use in vector potential finite element analysis in electric machinery", IEEE trans. on Magnetics, Vol. MAG-17, No.6, Nov., pp. 3002-3004.

Chari, M.V.K. Bedrosian, G. and D'Angelo, J., (1993), "Finite element applications in electrical engineering", IEEE trans. on Magnetics, Vol. MAG-29, No.2, March, pp. 1306-1314.

Salon, S.J., and D'Angelo, J., (1988), "Applications of the hybrid finite element – boundary element method in electromagnetics", IEEE Trans. on Magnetics, Vol. MAG-24, No.1, Jan., pp. 80-85.

Salon, S.J., and Schneider, J.M., (1981), "A hybrid finite element boundary integral formulation of Poisson's equation", IEEE Trans. on Magnetics, Vol. MAG-17, No.6, Nov., pp. 2574-2576.

Henneberger, G., Sattler, Ph.K. and Shen, D., (1991), "Force calculation with analytical accuracy in he finite element based computational magnetics", IEEE Trans. on Magnetics, Vol. 27, No.5, Sept., pp. 4254-4257.

Deng, F., and Demerdash, N.A., (1998), "Comprehensive salient-pole sychronous machine parametric design analysis using time-step finite element-state space modeling techniques", IEEE Trans. on Energy Conversion, Vol. 13, No.3, Sept., pp. 221-227.

Abdel-Razek, A.A, Coulomb, J.L., Feliachi, M. and Sabonnadiere, J.C., (1982), "Conception of an air-gap element for the dynamic analysis of the electromagnetic field in electric machines", IEEE Trans. on Magnetics, Vol. MAG-18, No.2, March., pp. 655-659.

Strahan, R.J., (1998), "Energy conversion by nonlinear permanent magnet machines", IEE Proc.-Electr. Power Appl., Vol. 145, (3), May, pp. 193-198.

Lee, K., DeBortoli, M,J, and Salon, S.J., (1991), "Coupling finite elements and analytical solution in the airgap of electric machines", IEEE Trans. on Magnetics, Vol. MAG-27, No.5, Sept., pp. 3955-3957.

Salon, S.J., and Hamilto, H.B., (1980), "The application of Poynting's vector to the determination of synchronous machine impedances", IEEE Trans. on Power Apparatus and systems, Vol. PAS-99, No.4, July/Aug., pp. 1442-1446.